ORNL/HTSPC-12

ORNL Superconducting Technology Program for Electric Power Systems

Annual Report for FY 2000

April 2001

SUPERCONDUCTIVITY FOR ELECTRIC SYSTEMS

ORNL/HTSPC-12

ORNL SUPERCONDUCTING TECHNOLOGY PROGRAM FOR ELECTRIC POWER SYSTEMS

ANNUAL REPORT FOR FY 2000

Compiled by
R. A. Hawsey
A. W. Murphy

Edited by
W. S. Koncinski

Manuscript Completed: February 2001
Date Published: April 2001

Prepared for the
Office of Power Technologies
Office of Energy Efficiency and Renewable Energy
U.S. DEPARTMENT OF ENERGY
(EB 50 01 00 0)

Prepared by
OAK RIDGE NATIONAL LABORATORY
P.O. Box 2008
Oak Ridge, TN 37831-6285
Managed by
UT-Battelle, LLC
for the
U.S. DEPARTMENT OF ENERGY
under contract DE-AC05-00OR22725

Contributors

Front row (left to right): Y. Choi, A. Ellis, C. Cantoni, B. Kang, A. W. Murphy, R. A. Hawsey, J. A. Demko, J. W. Lue, and H. R. Kerchner. **Second row (left to right):** G. C. Barber, R. K. Williams, V. Patania, D. F. Lee, P. M. Martin, A. Fadnek, M. P. Paranthaman, D. K. Christen, and I. Sauers. **Back row (left to right):** D. O. Sparks, P. W. Fisher, S. Sathyamurthy, D. H. Lowndes, T. Aytug, D. B. Beach, F. A. List, H. Christen, M. J. Gouge, D. M. Kroeger, B. W. McConnell, R. Feenstra, D. R. James, M. A. Brown, and J. P. Stovall. Not pictured are: A. Goyal, S. W. Schwenterly, J. D. Budai, and E. D. Specht.

Contents

List of Figures

List of Tables

Acronyms and Initialisms

ac	alternating current
ACSR	aluminum construction steel reinforced
AEM	analytical electron microscopy
ASC	American Superconductor Corporation
BIL	basic impulse level
BKD	backscatter Kikuchi diffraction
CCVD	combustion chemical vapor deposition
CRADA	cooperative research and development agreement
dc	direct current
DOE	U.S. Department of Energy
DOE-HQ	DOE Headquarters
DTA	differential thermal analysis
DTA/TGA	differential thermal analysis/thermogravimetric analysis
e-beam	electron beam
EBKD	Electron Backscattered Kikuchi Diffraction
EDS	energy-dispersive spectroscopy
FEG	field emission gun
FTRA	fast temperature range annealing
FWHM	full width at half maximum
GB	grain boundary
GBMD	grain boundary misorientation distribution
Hg-HTS	mercury-based high-temperature superconductors
HTS	high-temperature superconductivity/superconductor/superconducting
HV	high vacuum
IBAD	ion-beam-assisted deposition
I_c	critical current
IEC	International Electric Commission
IGC	Intermagnetics General Corporation
I_p	peak current
I_{rms}	root mean square cable current
ISD	inclined substrate deposition
J_c	critical current density
J_e	engineering critical current density
K_c	critical current per unit width of conductor (I_c/w)
KU	University of Kansas
LANL	Los Alamos National Laboratory
LAO	lanthanum aluminate
LN_2	liquid nitrogen
LTS	low-temperature superconductor
LZO	lanthanum zirconium oxide
MOCVD	metal-organic chemical vapor deposition
MOD	metal organic decomposition
ORNL	Oak Ridge National Laboratory
PIT	power-in-tube
PLC	programmable logic controller
PLD	pulsed-laser deposition

R&D	research and development
RABiTS™	rolling-assisted biaxially textured substrates
RBS	Rutherford Backscattering Spectroscopy/Spectrum
rf	radio frequency
RG&E	Rochester Gas and Electric Company
rms	root mean square
RTA	rapid thermal annealer
SAD	selected area diffraction
SEM	scanning electron microscopy
SEM-EDAX	scanning electron microscopy–energy-dispersive X-ray microanalysis
s.f.	self field
SFO	surface flashover
SMES	Superconducting Magnetic Energy Storage
SPI	Superconductivity Partnership Initiative
SRO	$SrRuO_3$
STEM	scanning transmission electron microscopy
STO	strontium titanate
SUNY	State University of New York
T_c	critical temperature/transition temperature
TEM	transmission electron microscopy
TFA	trifluoroacetate
TGA	thermogravimetric analysis
thd	tetra-methyl-heptane-dionate
ULPA	ultra-low penetrating air
WDG	Wire Development Group
WES	Waukesha Electric Systems
XRD	X-ray diffraction
YBCO	yttrium barium copper oxide
YSZ	yttria-stabilized zirconia
Z-STEM	Z-contrast scanning transmission electron microscopy

Executive Summary

The Oak Ridge National laboratory (ORNL) Superconducting Technology Program is conducted as part of a national effort by the U.S. Department of Energy's Office of Energy Efficiency and Renewable Energy to develop the science and technology base needed by U.S. industry for development of electric power applications of high-temperature superconductivity. The two major elements of this program are wire development and applications development. This document describes the major research and development activities for this program together with related accomplishments. The technical progress reported was summarized from recent open literature publications, presentations, and information prepared for the FY 2000 Annual Program Review held July 17–19, 2000. Aspects of ORNL's work that were presented at the Applied Superconductivity Conference (September 2000) are included in this report as well. This ORNL program is highly leveraged by the staff and other resources of U.S. industry and universities. Interlaboratory teams are also in place on a number of industry-driven projects. Working group meetings, staff exchanges, and joint publications and presentations ensure that there *is* technology transfer with U.S. Industry. Working together, the collaborative teams are making rapid progress in solving the scientific and technical issues necessary for the commercialization of long lengths of practical high-temperature superconductor wire and wire-using systems.

Highlights

WIRE RESEARCH

- High engineering current density (J_E) $YBa_2Cu_3O_{7-y}$ (YBCO) coated conductors were fabricated on Rolling-Assisted Biaxially Textured Substrates (RABiTS™) with a layer sequence of CeO_2/YSZ/Ni. An industrially scalable ex situ BaF_2 precursor process and biaxially textured Ni (100) substrates with a thickness of 50 μm were used. The YBCO films were grown on PLD-buffered CeO_2/YSZ/Ni (100) substrates using e-beam co-evaporated Y-BaF_2-Cu precursors followed by post-annealing. As a test model, high-quality YBCO films with a J_c of over 3.1 MA/cm^2 at 77 K and self-field were grown on CeO_2-buffered YSZ (100) single crystal substrates. Also, high-quality YBCO films with a thickness of over 1 μm carried a J_c of over 1 MA/cm^2 at 77 K and self-field were grown on PLD-buffered CeO_2/YSZ/Ni (100) substrates. A high J_E of over 28,000 A/cm^2 at 77 K was achieved for a YBCO film thickness of 1.6 μm on RABiTS™ for the first time. This result demonstrates the possibility of using both the ex situ BaF_2 precursor approach and the RABiTS™ process for producing long lengths of coated conductors.

- Equipment has been designed and is being installed to enable continuous processing, measurement, and characterization of lengths of YBCO/RABiTS™. To date, 140 m of RABiTS™ tape provided by CRADA partner 3M has been characterized on a reel-to-reel X-ray system.

- To ultimately demonstrate the quality of long-length precursors on RABiTS™ tapes, high-J_c YBCO superconductors must be grown. We have deposited long-length precursors on RABiTS™ under reel-to-reel moving-tape conditions; the product had an architecture of CeO_2/YSZ/CeO_2/Ni. The thickness, length, and width of the YBCO tape were 310 nm, 70 cm, and 1 cm, respectively. Due to the short isothermal region of our conventional furnace (only 30 cm), the precursor tape was cut into short pieces for annealing in a stationary mode. The J_c at 77 K in self-field of various sections along a 5-cm-long YBCO tape was determined to be 0.54 MA/cm^2 with the 1-μv/cm criterion.

- We have demonstrated that epitaxial Eu_2O_3 and LZO buffer layers can be grown on biaxially textured-Ni (100) substrates in meter lengths in a continuous reel-to-reel dip-coating unit. The dip-coated buffers were dense, continuous, and crack-free. Longer annealing times produced carbon-free films. On dip-coated Eu_2O_3 seed layers, we have produced high-quality YBCO films with a J_c of over 1 MA/cm^2 at 77 K and self-field with a layer sequence of YBCO (ex situ BaF_2 process)/CeO_2 (sputtered)/YSZ (sputtered)/Eu_2O_3 (dip-coated)/Ni.

- To complement our work on vapor-deposited conducting buffers, we have developed a nonvacuum, solution-based approach for growing $SrRuO_3$ (SRO) buffers. We have successfully grown epitaxial SRO layers on single-crystal substrates. The SRO precursor solution was prepared by an alkoxide route and was spin-coated onto single-crystal substrates. In addition, we have grown YBCO films with a J_c of over 1 MA/cm^2 at 77 K and self-field on solution SRO seed layers by means of pulsed laser deposition.

- Conductive multilayers of $YBa_2Cu_3O_{7-\delta}$/$SrRuO_3$/$LaNiO_3$ (YBCO/SRO/LNO), YBCO/SRO and YBCO/LNO were grown epitaxially on single-crystal $LaAlO_3$ and $SrTiO_3$ substrates. Property characterizations revealed that the YBCO films on SRO and SRO/LNO buffer structures have excellent structural and superconducting properties. However, the YBCO/LNO suffers degradation in superconducting transition temperatures and critical current densities, despite a good crystalline

structure. The SRO/LNO bilayer showed excellent electrical contact with YBCO. These results have demonstrated the structural and chemical compatibility of SRO/LNO multilayers with YBCO and their potential use as conductive buffer layers for YBCO-based coated conductors as well as for other HTS applications.

- The role of conductive buffer layers in the stability of Ni-based coated conductors and the effect of a metallic cap layer on the electrical properties of Ni-alloy-based superconducting tapes have been studied. For the first case we report on the fabrication of a fully conductive RABiTS™ architecture formed of bilayers of the conductive oxides SRO and $LaNiO_3$ on textured Ni tapes. For the second case we discuss measurements of current-voltage relations on $Ag/YBa_2Cu_3O_{7-\delta}$ and $Cu/Ag/ YBa_2Cu_3O_{7-\delta}$ prototype multilayers on insulating substrates. Limitations on the overall tape structure and properties that are posed by the stability requirement are presented.

- Significant progress has been made in applying the ex situ BaF_2 technique to (1) fabrication of long lengths of nonmagnetic, mechanically strengthened, biaxially textured metal templates in the reel-to-reel deposition of oxide buffer layers and (2) the fabrication of long-length superconductors. Significant progress has also been made in understanding the role of meso-scale defects such as grain boundaries on long-range current flow of high-temperature superconducting (HTS) conductors made by using the RABiTS™ approach. Both experimental and theoretical calculations suggest that these commonly present defects do not provide an intrinsic barrier to current flow in well-textured samples of long-length conductors.

- A low-cost, nonvacuum, solution precursor route has been developed to produce epitaxial Gd_2O_3 and Eu_2O_3 buffer layers and $YBa_2Cu_3O_{7-\delta}$ (YBCO) superconductors on biaxially textured metal substrates. On sol-gel Eu_2O_3 seed layers with sputtered YSZ and CeO_2 top layers, a YBCO film with a J_c of over 1 MA/cm^2 at 77 K was obtained. On all solution buffer layers (CeO_2/Eu_2O_3/Ni), a YBCO film with a J_c of 200,000 A/cm^2 at 77 K was grown by using pulsed laser deposition (PLD). Meter lengths of epitaxial, crack-free Gd_2O_3 buffer layers were fabricated on cube-textured Ni-W (3 at. %) substrates for the first time.

- Solution-based techniques have been examined as potential low-cost processes for manufacturing YBCO coated conductors. YBCO films prepared from metal trifluoroacetate precursors have achieved performance levels equaling or exceeding that of vapor-deposited films with the same thickness on CeO_2/YSZ(Xtal) substrates. Critical current densities of 4.5 MA/cm^2 and 2 MA/cm^2 have been achieved in 0.4-μm-thick YBCO films on CeO_2/YSZ(Xtal) and CeO_2/YSZ/CeO_2/Ni substrates, respectively. Textured Gd_2O_3 buffer layers have been deposited on deformation-textured Ni substrates in a reel-to-reel process. The performance of YBCO films deposited on substrates containing the Gd_2O_3 seed layers is comparable in performance to YBCO films grown on all vacuum-deposited buffer layers.

- First results of a study directed at raising the critical current I_c of ex situ processed YBCO coated conductors by increasing the YBCO thickness are reported. The substrates are RABiTS™, produced by laboratory- and industrial-scale processes, and laboratory-scale ion-beam-assisted deposited yttrium-stabilized zirconia (IBAD-YSZ). Starting from an initial thickness of 0.3 μm, significant improvements in I_c by a factor of 3 to 4 were obtained for 1.5- to 3-μm-thick YBCO on the industrial-scale RABiTS™. The enhancements for ex situ YBCO were similar to those obtained for thick YBCO produced by an in situ PLD process. A maximum current of 200 A/cm width (77 K) was measured for a 1-μm-thick YBCO coating on IBAD-YSZ provided by Los Alamos National Laboratory. The relative contributions of effects related to thickness and texture toward a high I_c are discussed.

- A complete line of reel-to-reel equipment was developed to process and characterize YBCO/RABiTS™ tape of lengths up to 20 m. This equipment includes capabilities for
  — characterizing tape by X-ray diffraction,
  — annealing metal tapes to develop textures,
  — growing epitaxial buffer layers, and
  — depositing YBCO precursor materials (Y-BaF_2-Cu).

- The first 1-m lengths of YBCO/RABiTS™ tapes were processed by using a transverse flow reaction furnace to convert the YBCO precursor to YBCO. The end-to-end J_c of the tape was ~100 kA/cm^2. X-ray diffraction revealed that the one low-J_c region (1 cm) was due to high YBCO (103) intensity. The remaining 1-cm increments of the 1-m tape had J_cs from 300 to 770 kA/cm^2.

SYSTEMS RESEARCH

- Three facilities at Southwire Company now receive electricity through a HTS power cable system that was built and tested with the assistance of Oak Ridge National Laboratory's (ORNL's) Superconductivity for Electric Systems Program. ORNL and Southwire worked for four years to make the dedication on Feb. 18, 2000, possible. Secretary of Energy Bill Richardson was among those on hand for the dedication, which was highlighted by the secretary's moving three switches to convert the Southwire plant from a conventional power feeder to superconducting power feed. In CY 2000, the superconducting cable system provided 100% of the power to three manufacturing plants in Carrollton, Georgia, for 5,000 hours.

- Fault currents of more than ten times the design current have been applied to a 5-m cable system built by Southwire and located at the ORNL cable test facility. Subsequent dc measurements verified that there was no degradation of the HTS cable from the fault current tests or from earlier high-voltage tests, high-current tests, or thermal cycling.

- A U.S. Department of Energy (DOE) Superconductivity Partnership Initiative (SPI) is under way to develop HTS utility power transformers. The SPI team is led by Waukesha Electric Systems (WES) with team partners IGC-SuperPower (IGC), Rochester Gas and Electric Company, and ORNL. The SPI is now in Phase II; the objective is to build a 5/10-MVA HTS transformer and test it on the utility power grid to power the WES main transformer manufacturing plant. This transformer will operate with windings at temperatures well below 77 K. The 5/10-MVA transformer design is being carried out as a scaledown of the final 30-MVA design. A new cryocooled ac loss test facility was put into operation, and three sample coils provided by IGC were tested. Electrical insulation tests focused on solid insulation materials, the objective being to validate their capabilities to handle the 25-kV operating voltage and the 150-kV basic impulse level (BIL) of the 5/10-kV transformer.

1. Technical Progress in Wire Development

1.1 RECENT PROGRESS TOWARD CONTINUOUS PROCESSING OF YBCO/ RABiTS™ TAPE

F. A. List, E. D. Specht, S. W. Lu, and D. F. Lee

The steps for processing YBCO/ RABiTS™ tape include mechanical rolling of nickel or alloy, cleaning to remove debris and organic residue, annealing to develop texture, growing epitaxial oxide buffer layers, depositing YBCO precursor, reacting the precursor to form epitaxial YBCO, overcoating the YBCO with silver, and measuring I_c/J_c (see Fig. 1.1). Fabrication of tape in lengths greater than ~1 m generally requires that all processing be fully compatible with tape motion from one spool to another. At ORNL, a complete line of reel-to-reel equipment is being developed to process and characterize YBCO/RABiTS™ tape in lengths up to ~20 m. This equipment includes capabilities for (a) characterizing tape by X-ray diffraction (XRD), (b) annealing metal tape to develop texture, (c) growing an epitaxial CeO_2 buffer layer, and (d) depositing the YBCO precursor. The efforts to design and develop the laboratory-scale equipment are intended to facilitate the development and optimization of continuous processes for fabrication of YBCO/RABiTS™ tape. Beneficiaries of these efforts include ORNL and its industrial partners.

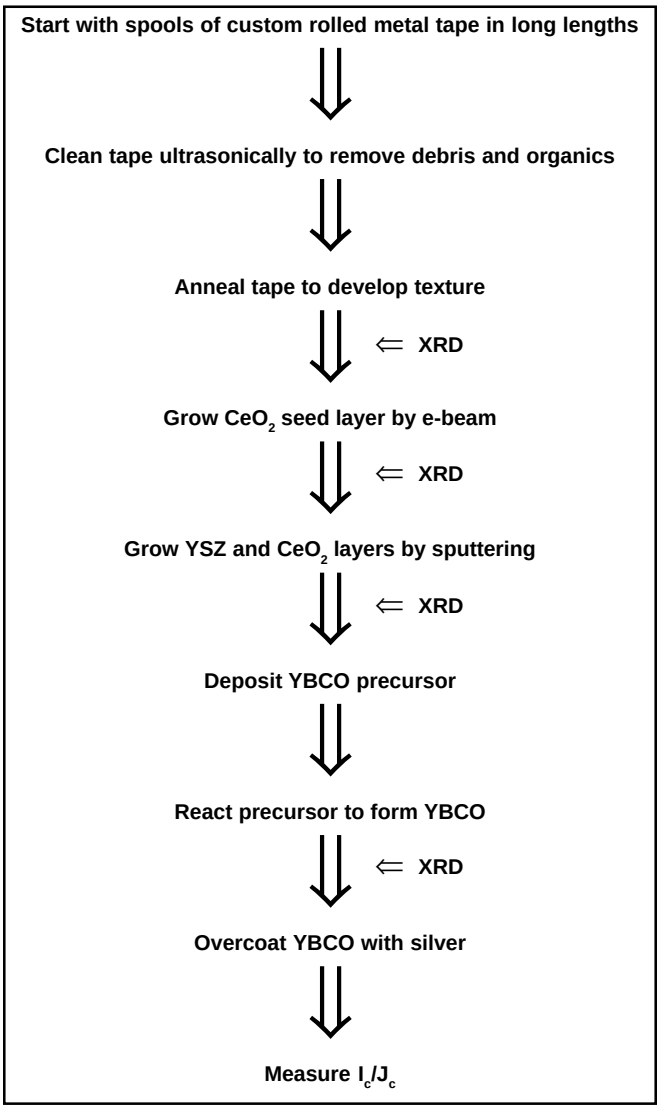

Fig. 1.1. Flow diagram for processing longer-length samples of YBCO/RABiTS™ tape by continuous reel-to-reel processing.

Figure 1.2 shows a photograph of the reel-to-reel XRD system used for characterization of the tape throughout the fabrication process. For stationary tape, θ-2θ, ϕ, and ω scans can each be obtained in ~2 min, and a complete pole figure requires ~30 min. For moving tape, tape speeds of ~5 cm/s are typically used for characterization. To date, more than 1 km of buffered tape has been characterized with this system.

Rapid, nondestructive characterization by XRD has facilitated the development of epitaxial buffer layers for both ORNL and its industrial collaborators. Figure 1.3 shows the θ-2θ diffraction intensity for

Fig. 1.2. Reel-to-reel X-ray diffraction system.

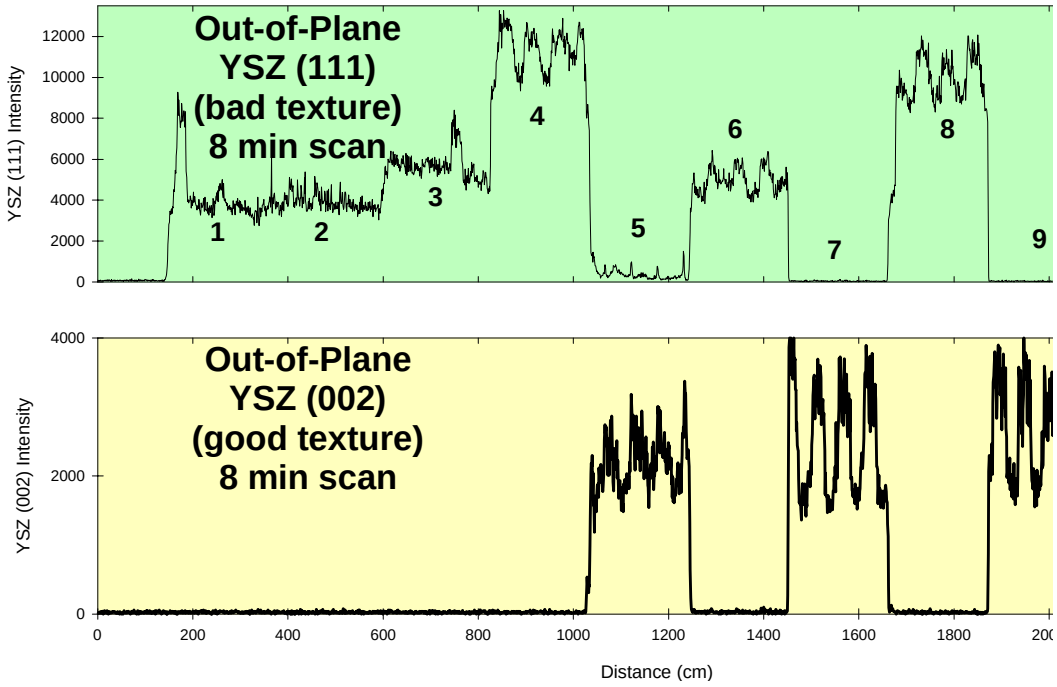

Fig. 1.3. θ-2θ diffraction intensity for YSZ (111) and YSZ (002) along a 24-m length of RABiTS™ tape prepared by 3M Company.

YSZ (111) and YSZ (002) obtained along a 24-m length of RABiTS™ prepared by collaborators at 3M Company. The conditions for buffer layer deposition were intentionally varied ten times over the 24-m length. The step changes of XRD intensity are reflections of the changes in deposition conditions and are used for optimization of the deposition process. Also seen in the data are periodic variations in diffraction intensity (period ~55 cm). This periodic variation in X-ray quality was traced to a problem with tape handling during buffer layer deposition and was subsequently corrected.

Figure 1.4 shows a photograph of a reel-to-reel vacuum system used for both annealing metal tape and depositing buffer layers. Noncontact annealing of tape is accomplished by thermal radiation from a tantalum tube mounted coaxially to the tape and radio-frequency (rf) heated. Epitaxial CeO_2 buffer layers are deposited on a heated tape by e-beam evaporation of cerium metal in an atmosphere containing water vapor. To date, greater than 99% cube texture has been obtained on 5-m lengths of both nickel and nickel-tungsten alloy. On these substrates, 10-Å epitaxial CeO_2 has been deposited with out-of-plane texture of greater than 95% (002).

The deposition of BaF_2 precursor is performed in a reel-to-reel e-beam co-evaporation system (see Fig. 1.5). The fluxes of Y, BaF_2, and Cu are controlled by feedback for quartz-crystal monitors to obtain composition and thickness variations of ~2%. Figures 1.6 and 1.7 show typical Rutherford backscattering spectroscopy (RBS) results for a BaF_2 precursor on a 1-m tape. Good uniformity of composition and thickness is evident. Tape speed for deposition of a 3000-Å precursor is ~0.8 m/h.

Fig. 1.4. Reel-to-reel vacuum system for annealing tape and depositing buffer layers.

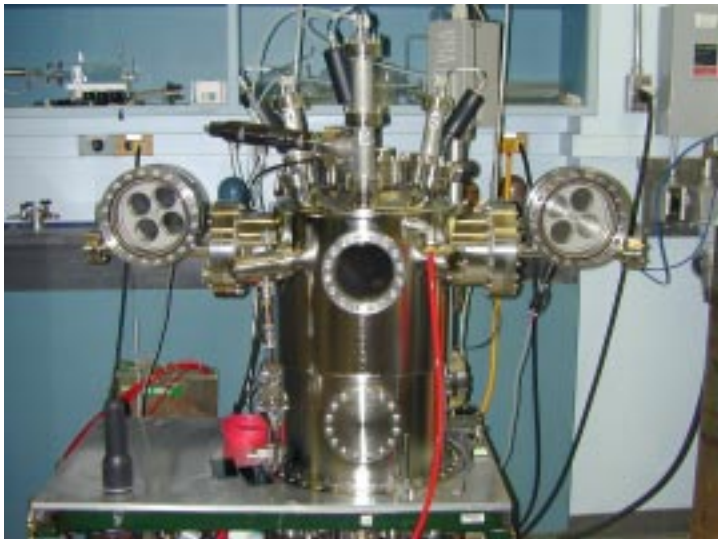

Fig. 1.5. Reel-to-reel e-beam co-evaporation system.

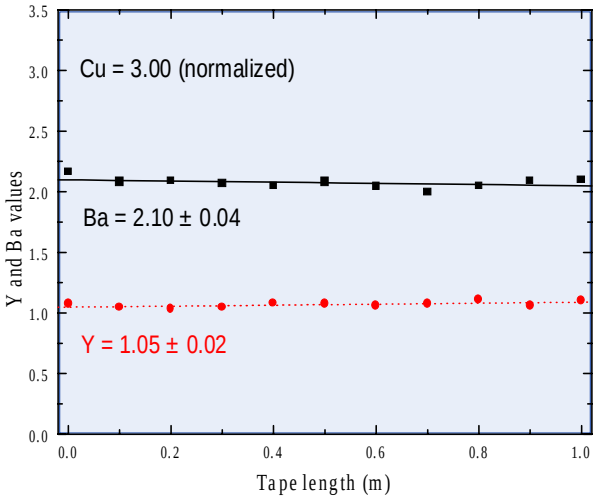

Fig. 1.6. Rutherford Backscattering Spectroscopy results for a BaF_2 precursor on a 1-m tape (composition vs length).

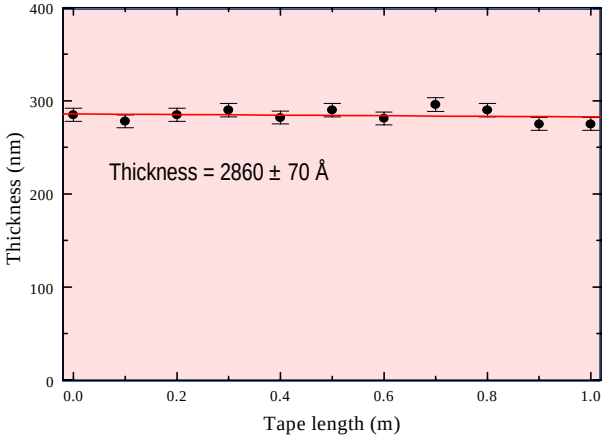

Fig. 1.7. Rutherford Backscattering Spectroscopy results for a BaF_2 precursor on a 1-m tape (thickness vs length).

1.2 ISSUES AND PROGRESS RELATED TO CONTINUOUS EX SITU BaF_2 PROCESSING OF LONG-LENGTH YBCO COATED CONDUCTORS

D. F. Lee, F. A. List, S. W. Lu, E. D. Specht, P. M. Martin, H. Hsu, A. Goyal, D. M. Kroeger, K. W. Childs, R. Feenstra, M. Paranthaman (ORNL); and W. B. Robbins (3M Company)

1.2.1 Introduction

For the past several years, an increasing amount of effort in the high-temperature superconductivity (HTS) community has been focused on the development of YBCO coated conductors. Very high values of critical current density (J_c), in excess of 10^6A/cm^2 at 77 K and self-field, have been reported on YBCO films grown on biaxially textured metallic substrates. These excellent results were typically obtained on a variety of short-length (less than 2-cm) textured templates such as ion-beam-assisted-deposition (IBAD) substrates,[1-4] RABiTS™,[5-8] and, to a lesser extent, inclined-substrate-deposition (ISD) substrates.[9,10] YBCO deposition methods employed to obtain these high J_cs include pulsed-laser deposition (PLD),[11] thermal evaporation,[10] or metal-organic chemical vapor deposition (MOCVD)[12,13] of the BaF_2 precursor[14,15] and trifluoroacetate (TFA).[16]

There have been ample demonstrations of high J_cs on short-length YBCO coated conductors; however, there has been only limited investigation into the feasibility and the issues related to the fabrication of meter-length YBCO coated conductors, mainly because of the limited availability of the long-length substrates and resources needed to investigate epitaxial YBCO formation on moving substrates. An in situ PLD technique has been used to produce meter-length YBCO samples with high end-to-end J_cs.[17-19] It is a well-proven technique, and much knowledge has been gained about the continuous deposition of YBCO by PLD; however, PLD and other in situ techniques may require simultaneous control of film composition and HTS epitaxial growth within a narrow process window.

The ex situ approach of YBCO formation separates the precursor deposition step (i.e., compositional control) from the YBCO epitaxial growth process. By separating these steps, further simplification in processing procedures, such as nonvacuum deposition of precursor film[16] or batch conversion of YBCO,

is possible. Unfortunately, most of the ex situ works to date have been performed on short-length samples. Consequently, issues related to the continuous ex situ processing of YBCO are largely unknown, and thus the feasibility of using this method for manufacturing long-length YBCO coated conductors cannot be evaluated. In this section, we present (1) the progress in ex situ BaF_2 processing of long-length YBCO coated conductors on moving substrates and (2) the known issues important to it.

1.2.2 BaF_2 Ex Situ Process

One of the better-known ex situ YBCO formation techniques is the BaF_2 process. In this process, stoichiometric amounts of Y, Cu, and BaF_2 are co-evaporated onto a substrate at room temperature. The precursor film is then converted into YBCO at an elevated temperature in a controlled atmosphere, as shown schematically in Fig. 1.8. The precursor film is heated to a conversion temperature in a humidified, reduced-oxygen environment (e.g., 740°C in 70 Torr H_2O and 130 mTorr O_2). It has been proposed that during this heat-up, the metal-oxyfluoride precursor starts to decompose in the presence of H_2O and releases HF into the environment; the decomposed precursor product is converted into YBCO according to the following schematic reactions:[20]

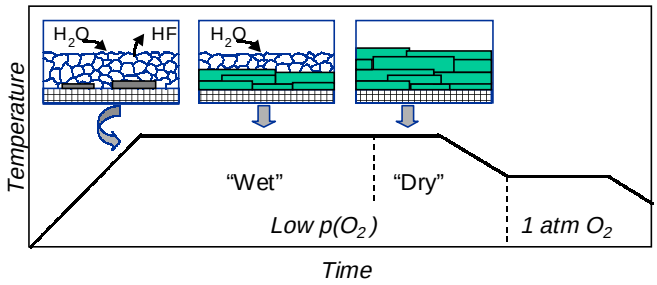

Fig. 1.8. Schematic of typical oxyfluoride decomposition/YBCO conversion schedule used in the ex situ processing of YBCO conductors.

$$Y_2O_3 + CuO + BaF_2 \rightarrow CuO + (Y\text{-}Ba\text{-}O\text{-}F) \ , \quad (1)$$

$$CuO + (Y\text{-}Ba\text{-}O\text{-}F) + H_2O \rightarrow (Y\text{-}Ba\text{-}Cu\text{-}O)_{liquid} + 2HF \ , \quad (2)$$

$$(Y\text{-}Ba\text{-}Cu\text{-}O)_{liquid} \rightarrow YBCO \ . \quad (3)$$

The critical step is when BaF_2 (or Y-Ba-O-F) decomposes, and it must be able to decompose totally and efficiently. That is, to achieve complete conversion of the precursor to epitaxial YBCO, it is necessary for the sample to be annealed in the humidified environment for a sufficient length of time so that the oxyfluoride is fully decomposed. Once this step has been accomplished, the environment is switched to "dry" to ensure that YBCO formation will proceed to completion without degradation due to moisture. Then the sample is cooled to room temperature.

This general procedure and simple longitudinal-flow reaction chambers have been used to produce short lengths of high-quality YBCO films at our laboratory and elsewhere[14-16,20,21] (see Fig. 1.9). When we attempted to process samples of longer lengths, however, YBCO conversion was found to be nonuniform.[22] The 10-cm-long sample in Fig. 1.9, deposited on RABiTS™, was converted ex situ in a simple longitudinal-flow geometry; the upstream portion of the sample has been

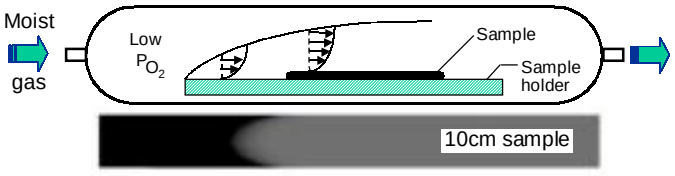

Fig. 1.9. Top: schematic of a simple longitudinal-flow quartz reaction chamber typically utilized in the ex situ processing of short-length YBCO conductors. Bottom: typical 10-cm-long YBCO conductor on RABiTS™ converted in such a reactor.

converted to YBCO, and a substantial section at the downstream end remained unconverted. We believe that this nonuniformity in conversion is largely related to the local HF/H_2O concentration ratio near the sample surface. According to Eq. (2), HF is released into the environment as H_2O reacts with oxyfluoride during its decomposition. Consequently, unless HF is efficiently removed from the sample surface, decomposition of the oxyfluoride will slow or even terminate with time, owing to a buildup of HF. When this occurs, a corresponding reduction and eventual stoppage of YBCO conversion results. This is a possible scenario during conversion of lengths in a simple longitudinal-flow chamber where the gas velocity is typically low and the effective dimension of conversion is large (i.e., the sample length). During ex situ annealing, the upstream portion of a sample will undergo the oxyfluoride decomposition/YBCO conversion reaction first, while releasing HF into the environment. In the absence of efficient removal of HF, this will lead to a local increase in HF concentration downstream, effectively reducing the decomposition/conversion rate of the adjacent material. This effect may be insignificant for short lengths, but it is likely to be important as one increases the length of the sample and may cause the nonuniformity in YBCO conversion that we have observed.

It is, of course, possible to increase the length of "wet" conversion time to obtain YBCO at the downstream portion of a long tape. However, doing so will result in the degradation of converted material at the upstream section of the tape due to excessive exposure to the humidified atmosphere. In addition, the time necessary to process a length of YBCO conductor in such a manner will be practically prohibitive. Therefore, since 1998, we have engaged in the study of a two-pronged approach that can minimize the nonuniform conversion problem while maximizing the amount of material that can be converted at one time. This approach utilizes an extended transverse-flow geometry. By employing a transverse-flow geometry in which the direction of gas flow is parallel to the width of the sample, the effective conversion distance is reduced significantly. Furthermore, the presence of an extended reaction zone along the sample length will enable the simultaneous conversion of a larger area of precursor, thereby reducing the total amount of processing time.

1.2.3 Computational Fluid Dynamics Simulations of Transverse-Flow Geometry

Prior to the design and fabrication of our extended transverse-flow reaction chamber, computational fluid dynamics simulations were performed to visualize the flow profile of a sample suspended in a transverse-flow geometry. In addition, simulations were performed to study the effects of flow rate on both gas velocity and HF concentration in the vicinity of the sample. A commercially available program was used to perform the simulation. Square meshes were generated, which represent the transverse cross section of a 4.5-cm-wide by 1-cm-high rectangular reaction chamber (see Fig. 1.10). A 1-cm-wide tape is suspended at the center of this simulated chamber such that the longitudinal axis of the tape (i.e., the length of the tape) is perpendicular to the plane of the figure. Two 125-μm-high slots are located at either side of the chamber; the slot on the left is the gas inlet and the slot on the right is the outlet, resulting in a transverse-flow geometry across the width of the sample.

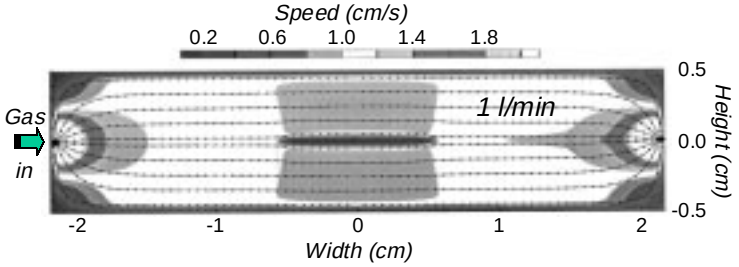

Fig. 1.10. Simulated flow profile within the transverse cross section of a transverse-flow reaction chamber. Flow rate of the gas is 1 L/min; the 1-cm-wide sample is located at the center of the chamber.

Figure 1.10 shows the simulated flow profile within the transverse cross section of the reaction chamber. It can be seen that there is no unexpected stagnant region around the sample, and uniformity of gas-flow velocity is rapidly achieved a short distance from the gas inlet. Closer examination of gas velocity in the vicinity of the sample surface reveals that gas flow is symmetric around the middle of the sample and that gas velocities are higher at the leading and trailing edges of the sample than at the middle (see Figs. 1.10 and 1.11). Figure 1.11 shows that the boundary-layer thickness increases with gas flow rate, as expected. More importantly, these simulations show that gas velocity is substantially increased at every location near the sample surface when a higher flow rate is employed. For example, at a location 100 μm above the sample surface and along the leading edge, gas velocity for the 5 L/min flow rate case is 4 times that of the 1 L/min case. This suggests that a high gas flow rate will be more effective in reducing the HF concentration near the sample surface by virtue of the higher gas velocity.

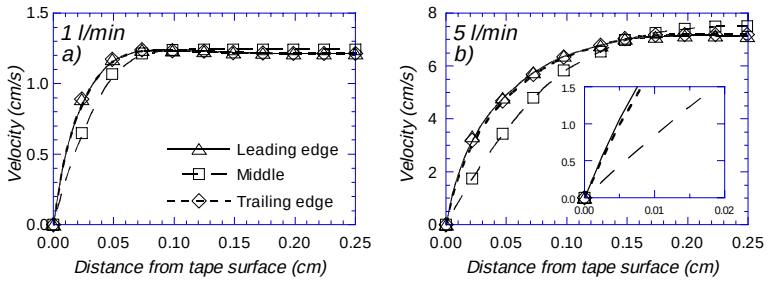

Fig. 1.11. Variation in gas velocity with distance from tape surface at various locations along the sample width for flow rates of (a) 1 L/min and (b) 5 L/min. The inset in (b) shows enhanced detail near the tape surface.

To examine the influence of gas flow rate on HF concentration near the surface of the sample, flow simulations were performed using the same mesh setup on a 1-cm-wide sample with precursor material on the top surface only. HF concentration maps were generated for the two flow rates (1 and 5 L/min) by assuming that sufficient H_2O is present to convert a 1 μm-thick precursor will be fully converted in 1 h. It can be seen in Fig. 1.12 that the highest HF concentration for a given gas flow rate is located at the surface along the downstream portion of the sample. This is in agreement with our contention that as the oxyfluoride decomposition/YBCO conversion reaction proceeds, the HF concentration will increase downstream as HF is released at the leading edge. Then it is up to the flowing gas to help sweep the HF away from the sample surface so that a sufficiently low HF/H_2O concentration ratio is present for the oxyfluoride decomposition to proceed at a reasonable pace. The ability of a higher gas velocity to remove the HF more effectively can also be seen in the figure; not only is the HF concentration lower for the 5 L/min flow rate, that the region containing the highest HF concentration is much smaller. Figure 1.13 (left) shows a more detailed analysis of changes in HF concentration near the surface of the sample. It can

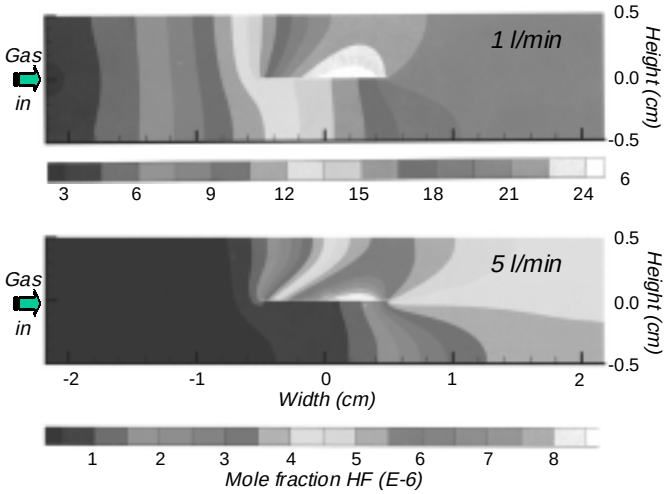

Fig. 1.12. Simulated HF concentration within the transverse cross section of a transverse-flow reaction chamber for gas flow rates of 1 and 5 L/min.

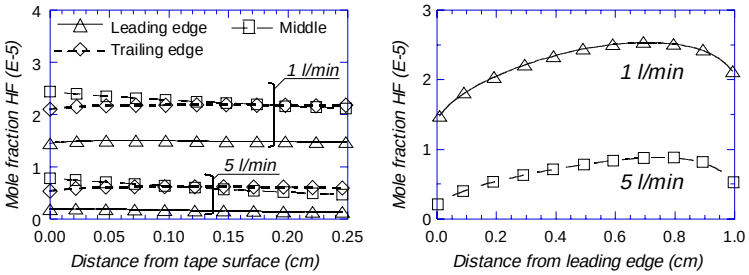

Fig. 1.13. Left: variations in HF concentration with distance from tape surface at various locations along sample width for 1 and 5 L/min flow rates. Right: changes in HF concentration at tape surface with distance from the sample leading edge for 1 and 5 L/min flow rates.

be seen from this figure that the local HF concentration at any specific location along the width of the sample does not appear to vary greatly with distance from the tape surface. Instead, HF variation along the sample width appears to be more significant. More importantly, the HF concentration at all locations is much lower for the 5-L/min flow rate than the 1-L/min case, with the reduction as high as a factor of 6. Variation in HF concentration at the surface of the sample is plotted as a function of the distance from the leading edge in Fig. 1.13 (right). It can be seen more clearly from this figure that even though the tendency of HF concentration to increase downstream remains in effect, an increase in flow rate will reduce the HF buildup significantly. Therefore, an extended transverse-flow reaction chamber with a high-flow-rate capability should enable the ex situ conversion of long-length YBCO coated conductors.

1.2.4 Reel-to-Reel Single-Module Transverse-Flow Reaction Chamber: Stationary YBCO Conversion

1.2.4.1 Design of Single-Module Transverse-Flow Furnace

An extended single-module transverse-flow reaction furnace was designed and built based on the flow simulation results (see Fig. 1.14). A reel-to-reel tape-handling system was incorporated so that the sample can be freely suspended within the reaction chamber. This capability is desirable because the presence of a sample holder will alter the gas-flow profile. Also, a tensioned reel-to-reel configuration will minimize any variation in orientation between sample and gas-delivery system due to sample expansion on heat-up. It was decided early on that a metal reaction chamber would be built because of its superior mechanical integrity and dimensional stability. Selection of the metal was based primarily on it resistance to oxidation as well as HF corrosion. After a literature survey and experimental testing, Inconel 601 was selected as the chamber material.

A modular approach was selected for the chamber design so that the longitudinal dimension of the reaction chamber could be easily expanded if the experimental results were promising. A single 30-cm-long flow module was incorporated into a 5-cm-wide by 1-cm-high housing (see Fig. 1.14). Two 1-cm-diam Inconel 601 tubes with

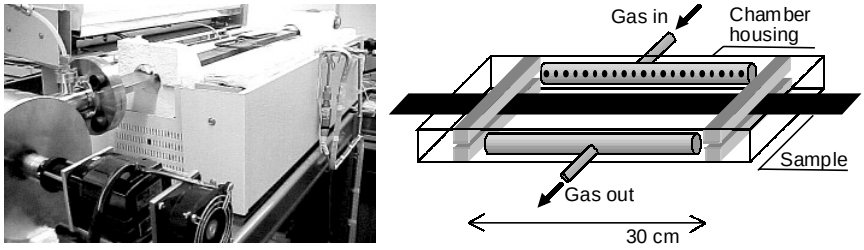

Fig. 1.14. Left: photo of the single-flow-module reaction chamber that sits in the cradle of a single-zone furnace. Right: a schematic of the 30-cm-long flow module located in the center of the 1-m-long reaction chamber housing.

125-μm holes were used as gas inlet and outlet ports. These tubes were welded in place; the holes are opposite their counterparts and in line with the sample, which is suspended between them. Reels were connected to the ends of a 1-m-long Inconel housing that sits in the cradle of a single-zone furnace. Standard components such as gas supply, water bubbler, and oxygen sensors were connected to the reaction chamber where necessary. In addition, pressure sensors were strategically located so that pressures at the gas inlet, at the gas outlet, and within the chamber could be continuously monitored.

1.2.4.2 Sample Preparation

Samples used in the ex situ conversion were prepared by co-evaporating Y, Cu, and BaF_2 onto RABiTS™ fabricated jointly by ORNL and 3M Company. Meter-length RABiTS™ were prepared by depositing ceramic buffer layers on textured Ni by a combination of reactive and rf magnetron sputtering.[23-26]

A standard RABiTS™ architecture of CeO_2(ORNL,m)/YSZ(ORNL or 3M,m)/CeO_2(3M,m)/Ni(3M,m) was used in this study. Note: In this notation, the institute within the parenthesis denotes where the work was performed, and "m" or "s" stands for moving or stationary, respectively. Both Ni annealing and buffer deposition were performed in a moving configuration on the reel-to-reel equipment. Typical buffer thicknesses are 220Å/1600Å/150Å; Ni thickness is 50 μm. As seen in Fig. 1.15 (left), XRD analyses confirmed that the RABiTS™ fabricated in an all-moving manner is highly textured. The in-plane (ϕ-scan) full-width-at-half-maximum (FWHM) of Ni, CeO_2 and YSZ are 10.6°, 11.1°, and 10.8°, respectively. There is, however, an approximately 10% second in-plane orientation that is rotated 45° from the major cube-on-cube orientation. The presence of this second in-plane orientation was found to originate from the CeO_2 seed layer.

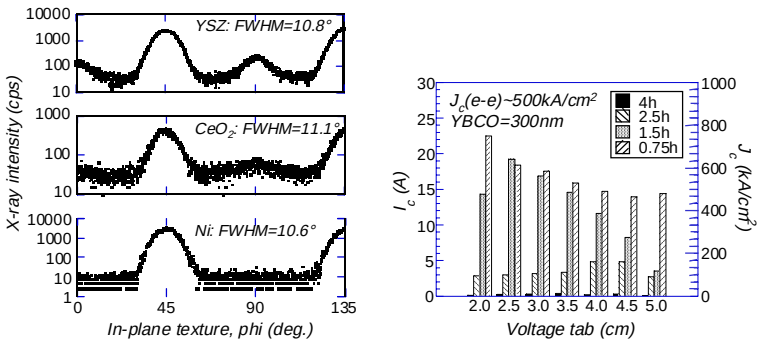

Fig. 1.15. Left: in-plane texture of typical RABiTS™ used in this work. Phi-scan FWHM of Ni, CeO_2, and YSZ layers are 10.6°, 11.1°, and 10.8°, respectively. Right: sectional J_cs of ex situ YBCO on RABiTS™ processed for various lengths of time in the reel-to-reel single-flow-module furnace.

Once the textured RABiTS™ samples were fabricated, they were loaded into a three-gun reel-to-reel electron-beam evaporation system for precursor deposition.[27] The system consists of a 15-kW electron-beam power supply with three electron-beam guns operating at a voltage of 8 kV. Source materials in the form of Y metal, Cu metal, and BaF_2 crystal were situated in three separate pockets. Precursor deposition was carried out in a H_2O partial pressure of 1×10^{-5} Torr with a total pressure of less than 6×10^{-5} Torr. At a tape traveling speed of 0.8 m/h, the precursor film was continuously deposited at a rate of 10 Å/s; the deposition rates of Y, BaF_2, and Cu were individually controlled by quartz crystal monitors. Precursor film deposited in such a fashion typically has a mean thickness of approximately 3000Å with a standard deviation of ±2.5% over the entire 1-m length. In addition, the typical Y/Ba/Cu film composition is roughly 1.05/2.1/3.0 with a standard deviation of less than ±2%.

1.2.4.3 YBCO Conversion in Stationary Mode

Because the test apparatus is a single flow-module chamber in a single-zone furnace, continuous processing by moving the sample through the length of the furnace is not possible. Instead, conversion is performed under a schedule similar to that shown in Fig. 1.8. During typical operation, a 1-cm-wide by 7-cm-long sample is spot-welded to Ni leaders and loaded into the center portion of the flow module under a constant ~1-N tension force. The sample is set to oscillate around the central location at a speed of 30-cm/h and a distance of 7-cm to avoid any conversion inhomogeneity due to possible jetting of the gas. The chamber is then purged with N_2 before backfilling with N_2-O_2 mixed gas maintained at an oxygen partial pressure of 130 mTorr. Once the flow has stabilized, the furnace is heated to 740°C at a ramp-up rate of 25°C/min. When the furnace has reached 150°C, the mixed gas is diverted through a water bubbler to attain a 70-Torr H_2O wet environment. After the furnace has reached 740°C, the sample is kept at this wet environment for a designated length of time before the gas is diverted away from the bubbler and the environment is switched to dry. The sample is further annealed at this temperature for an additional 1 h before being cooled to room temperature. Under this conversion schedule, the mode of conversion is considered stationary even though the sample is in motion because of the limited range of oscillating motion within the uniformly heated chamber.

Preliminary conversion runs were conducted to validate the design and operation of the single-flow-module furnace. To ensure sample-to-sample uniformity, four 1-cm-wide by 7-cm-long samples were cut from a 30-cm length of precursor on RABiTS™ where all depositions were performed on a moving substrate. The samples were individually loaded into the reaction chamber and heated to processing temperature as described in the previous paragraph. The lengths of wet conversion time for various samples were set at 240, 150, 90, and 45 min; the dry annealing time was kept constant at 60 min. Other processing parameters were kept constant for all four difference runs: 740°C processing temperature, 130 mTorr oxygen partial pressure, 70 Torr H_2O content, and gas flow rate of 4 L/min. Following conversion, XRD analyses of these samples did not reveal any BaF_2 diffraction peak, indicating that precursor conversions were completed in all the samples. These results are in contrast to results of similar samples converted in an older, low-flow-rate perpendicular-flow quartz furnace, where a wet conversion time of 120 to 180 min was necessary to convert precursors of identical thickness. For J_c characterization, Ag pads with 0.5-cm separation distance were deposited onto the samples so that sectional J_c values could be measured with the standard four-probe technique and 1 μV/cm criterion. Sectional J_c values of these YBCO(ORNL,s)-precursor(ORNL,m)/CeO_2(ORNL,m)/YSZ(ORNL,m)/CeO_2(ORNL,m)/Ni(ORNL,m) samples are shown in Fig. 1.15 (right). It can be seen from this figure that while all the samples are superconducting at 77 K, there is a clear influence of "over-conversion" on the J_cs of these YBCO films. As the wet conversion time is reduced, the J_c increases, reaching an end-to-end value of 500 kA/cm^2 for the 3000 Å-thick sample converted in 45 min.

Once the operation and effectiveness of the extended transverse-flow reaction chamber had been verified, we proceeded to examine the influences of various processing parameters on precursor conversion. Based on flow simulation and previous experimental observations, effects of flow rate and wet conversion time were investigated. A 1-m-long precursor (ORNL,m)/CeO_2(ORNL,m)/ YSZ(ORNL,m)/CeO_2(3M,m)/Ni(3M,m) sample was prepared in an all-moving manner. Individual 6.5-cm-long samples were cut from this stock to ensure sample-to-sample uniformity. A design-of-experiment approach based on a two-factor central composite design with continuous variables was selected for the experiment; the parameters are listed in Table 1.1. Individual samples were spot-welded onto Ni leaders and were oscillated around the center of the chamber at a speed of 30 cm/h and a distance of 7 cm. Flow rate and wet conversion time for each experimental run were set according to the values listed in Table 1.1; the remaining parameters were fixed as follows: ramp-up rate = 25°C/min, conversion

Table 1.1. Conversion parameters and resulting sample characteristics of YBCO conductors processed in the design-of-experiment study

Run No.	Flow rate (L/min)	Wet conversion time (min)	BaF_2(111) intensity (cps)	YBCO(006) intensity (cps)	Average J_c (S.D. < ±5%) (kA/cm^2)
3	0.5	143	12,830	18,654	0
7	1.0	45	80,847	26,569	0
11	1.0	180	0	56,413	48.5
2	1.0	240	0	85,703	102.1
8	2.5	45	6,756	102,880	567.1
12	2.5	60	0	124,150	747.7
4	2.5	143	0	112,515	438.6
6	2.5	200	0	108,938	313.0
10	4.0	30	1,633	85,447	373.9
1	4.0	50	0	88,852	387.3
5	4.0	90	0	106,557	416.5
9	4.0	143	0	73,371	269.5

temperature = 740°C, oxygen partial pressure = 130 mTorr, H_2O partial pressure = 70 Torr, and dry conversion time = 60 min.

Following the conversions, θ-2θ X-ray analyses were performed on each sample. All the YBCO diffraction patterns exhibited only (00*l*) peaks, indicating that the films are well aligned in the *c*-axis. Integrated BaF_2(111) intensities of the samples were analyzed to determine the extent of BaF_2 decomposition and are listed in Table 1.1. As expected, the BaF_2 signal in the samples disappeared as the conversion time for a given flow rate increased. More importantly, the length of conversion time necessary for BaF_2 to decompose decreased with increasing gas flow rate, which is in agreement with the flow simulation results. In addition to BaF_2, integrated YBCO(006) intensities were collected and are listed in Table 1.1. Variations in YBCO intensity with wet conversion time for the four different flow rates are shown in Fig. 1.16. It can be seen from this figure that, for a given flow rate, YBCO intensity initially increases with processing time. For higher flow rates (2.5 L/min and

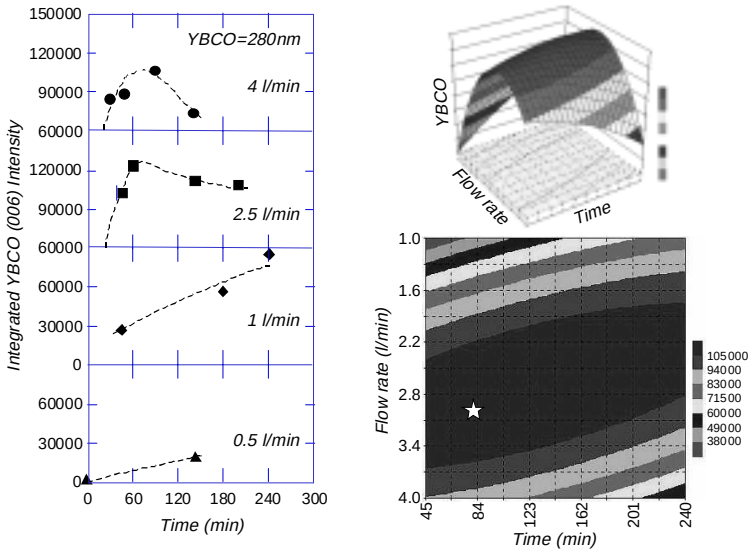

Fig. 1.16. Left: variations in integrated YBCO(006) intensity with wet conversion time for the four flow rates examined in the design-of-experiment study. Right: surface and contour plots constructed from response surface analysis of the data.

greater), the intensity reaches a maximum and then decreases on further processing. To better visualize the effect of changing processing parameters on YBCO intensity, response surface analysis was performed on the data. Surface and contour plots constructed from this analysis are shown in Fig. 1.16. The experimental data and response surface analysis both indicate that for low flow rates (less than ~1.5 L/min), an extremely long wet conversion time is necessary to achieve high YBCO counts, which is likely to be unrealistic in practice. As the flow rate is increased to 2.5 L/min, integrated YBCO intensity increases rapidly until it reaches a maximum value at approximately 60 min, then decreases. This decrease is believed to reflect the degradation of the YBCO phase in a moist environment and therefore should be avoided. As the flow rate is further increased to 4 L/min, a maximum in YBCO intensity is again seen in roughly the same conversion time as that of the 2.5 L/min flow condition. On the other hand, the maximum YBCO value found for the 4 L/min flow rate is lower than that of the 2.5-L/min condition. Because YBCO phase content, grain quality, and degree of grain alignment all contribute to its intensity, this result may signify that an optimum growth rate exists, above which degradation in grain quality or texture can occur. According to the response surface analysis, the optimum flow rate and processing time necessary to achieve maximum YBCO intensity (peak location marked by a star in Fig. 1.16) are approximately 3 L/min and 60 to 80 min, respectively, for this reaction chamber, precursor thickness, and other fixed processing parameters. If gas flow is further increased beyond 4 L/min, the oxyfluoride decomposition/YBCO formation rate may become excessive and a weaker YBCO intensity maximum may be reached at a shorter time. Coupled with this is the likelihood that YBCO degradation will occur rapidly, resulting in degraded tape performance. More extensive investigations need to be performed to examine this and other predictions from the response surface analysis.

After XRD analyses, multiple Ag contacts with a voltage-tap separation distance of 0.5 cm were sputtered onto individual samples. Seven sectional J_c measurements were performed on each sample, covering a total distance of 3.5 cm; the standard four-probe technique and a 1-μV/cm criterion were used. Average J_c values are listed in Table 1.1. Standard deviation of the J_c averages of all the samples is less than ±5%. Variations in average J_c with wet conversion time for these four different flow rates are shown in Fig. 1.17. It is immediately evident that J_c increases with processing time for slow flow rates. At higher flow rates, the J_c reaches a maximum and then decreases on further processing. Thus, the characteristic of J_c as a function of wet conversion time is identical to the behavior of YBCO(00*l*) intensity. This finding strongly suggests that relative changes in YBCO intensity can be used as a feedback parameter to optimize the J_c during processing. Response surface analysis was again performed. The surface and contour plots constructed from the analysis are shown in Fig. 1.17; the response

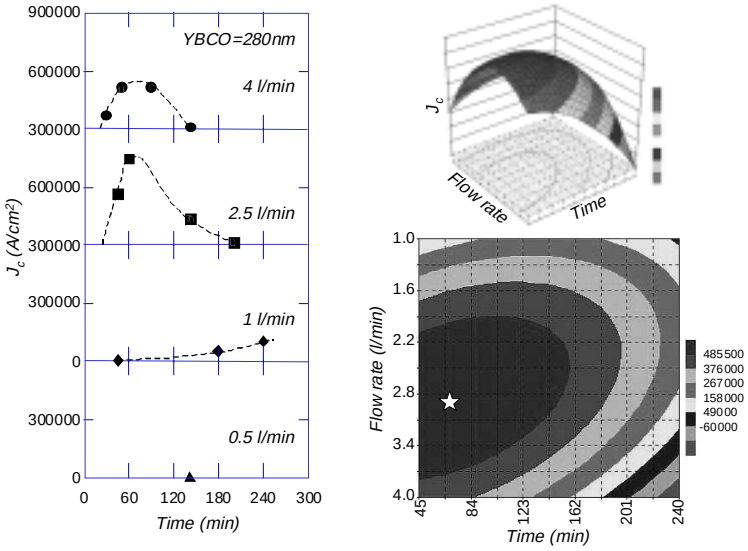

Fig. 1.17. Left: variations in average J_c with wet conversion time for the four flow rates examined in the design-of-experiment study. Left: surface and contour plots constructed from response surface analysis of the data.

surface of J_c is similar to that of the YBCO intensity. In general, the J_c for a given flow rate increases with conversion time, reaches a maximum value, and then decreases. In addition, the optimum conversion time decreases with flow rate. For the present reaction chamber, precursor thickness and fixed processing parameters (3 L/min and 60 to 70 min of conversion) represent the optimum processing conditions for J_c (marked by a star in Fig. 1.17). These predicted conditions are nearly identical to that of the YBCO intensity response surface and further support the possibility of YBCO intensity as a feedback parameter. When the two response surfaces are compared, it can also be seen that J_c is more sensitive to changes in processing conditions than YBCO intensity; for processing parameters that deviate greatly from the optimum conditions, the J_c value is zero or very low, even though the corresponding YBCO intensity may be sizable. Further design-of-experiment studies are under way to elucidate the influence and relative importance of other processing parameters.

1.2.5 Reel-to-Reel Seven-Module Transverse-Flow Reaction Chamber: Continuous YBCO Conversion

1.2.5.1 Design of the Seven-Module Transverse-Flow Furnace

Once the operation of the metallic single-module transverse-flow reaction chamber had been verified, a seven-module reaction chamber for continuous YBCO conversion was designed and built (see Fig. 1.18). Inconel 601 was selected as the building material. The chamber contains seven 30-cm-long flow modules that are identical to that of the single-module chamber shown in Fig. 1.14. Each flow module contains two 1-cm-diam Inconel 601 tubes with 125-μm holes, which serve as gas inlet and outlet ports. The tubes were welded in place; the holes are opposite their counterparts and in line with the sample, which is suspended between them. Blocks with 1.5-cm-wide slots were welded between neighboring flow modules to minimize crosstalk while allowing the tape to pass through the slot. Standard components, including gas supply, water bubblers, and oxygen sensor, were connected to the reaction chamber where necessary. In addition, multiple pressure sensors were strategically located so that pressures at gas inlets and gas outlets of different modules as well as that of the reaction chamber could be continuously monitored. Flow-modules 1 to 5 can be set to provide either a wet or dry gas environment, whereas modules 6 and 7 (downstream) remain dry at all times.

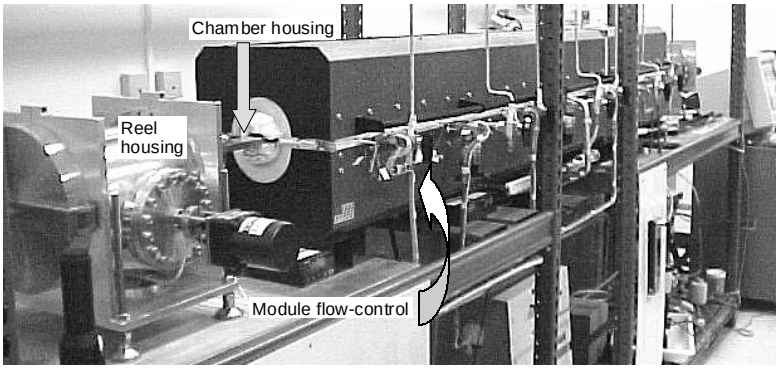

Fig. 1.18. Reel-to-reel metallic seven-module transverse-flow reaction chamber for continuous conversion of BaF_2 precursor. The chamber is situated in a 2-m-long, 22-zone furnace.

The 2.5-m-long seven-module reaction chamber is placed within the cradle of a custom-built 2-m-long 22-zone tube furnace. Temperature of the hot zones can be individually controlled such that a wide variety of thermal profiles may be obtained. By continuously moving the sample at a chosen speed through a selected thermal profile, a prescribed conversion schedule such as that shown in Fig. 1.8 for stationary conversion can be replicated. An example of a temperature profile that was employed in the 22-zone furnace is shown in Fig. 1.19. When a tape traveling speed of 0.63 m/h is used, the equivalent

stationary processing conditions can be approximated as 123 min wet conversion time and 36 min dry conversion time. In addition to conversion time, the temperature ramp-up rate, which can affect the texture and growth of YBCO, is also of interest. Because the furnace is equipped with narrow hot zones at the sample entrance end (hot zones 1 to 8), a sizable range of temperature gradients can be obtained by adjusting the settings of the hot zones. Figure 1.20 shows an example of temperature gradients that can be achieved in this furnace. For a conversion temperature of 740ºC, the ramp-up gradient can easily be varied from 14 to 70ºC/cm. Thus, by adjusting the temperature profile, tape traveling speed, gas flow rate, and other processing parameters, a multitude of conversion conditions can be explored.

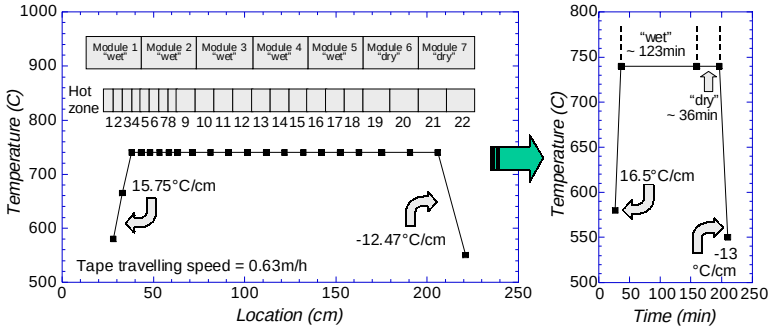

Fig. 1.19. Left: example of temperature profile employed in the 22-zone furnace. Right: the equivalent stationary conversion schedule.

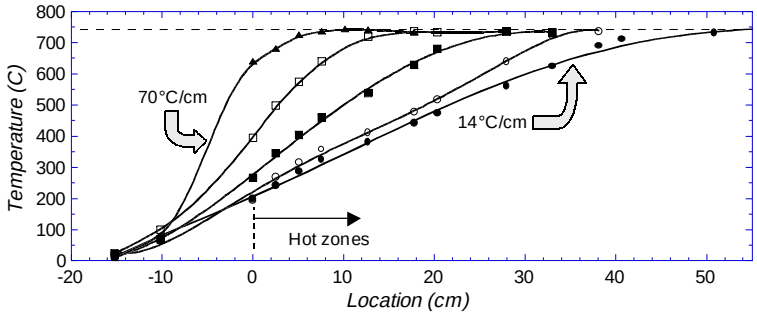

Fig. 1.20. A sizable range of temperature ramp-up gradients can be obtained by adjusting the temperature settings of hot zones.

1.2.5.2 YBCO Conversion in Continuous Mode

Preliminary runs were first performed on short tapes to evaluate the conversion characteristics of moving BaF_2 precursor in the seven-module reaction chamber. A 1-m-long precursor(ORNL,m)/CeO_2(ORNL,m)/YSZ(ORNL,m)/CeO_2(3M,m)/Ni(3M,m) was prepared on a metal substrate. Several 1-cm-wide by 7-cm-long samples were cut from the long tape and were spot-welded to Ni leaders with the front end of each sample situated outside of the furnace entrance prior to each run. Before commencement of conversion, the furnace was purged with N_2 gas and was backfilled with N_2-O_2 mixed gas that was maintained at an oxygen partial pressure of 130 mTorr and a flow rate of 3 L/min. A temperature profile was then selected, and the hot zones were heated to their respective set temperatures. Three conversion runs were conducted in identical temperature profiles with targeted wet conversion times of 90, 60 and 45 min. To achieve these conversion times, three tape traveling speeds of 0.86, 1.3, and 1.73 m/h with corresponding temperature ramp-up rates of 45, 68 and 90ºC/min were necessary. The tapes were continuously converted by moving each sample from the entrance to the exit end of the furnace. X-ray θ-2θ scans of these samples were performed and are shown in Fig. 1.21. While YBCO(00*l*) peaks are found for all the samples, the θ-2θ scans revealed that when the ramp-up rate is increased beyond a certain limit, random YBCO grains are formed during conversion [see the (103) peak in Fig. 1.21(c)]. Sectional J_c measurements, with a voltage-tap separation of 0.5 cm over a total distance of 3.5 cm, were performed. The average J_cs of the 90-, 60-, and 45-min samples are 6.8 ± 0.5 A, 7.6 ± 0.4 A, and 0.2 ± 0.2 A, respectively. These J_c results confirm that randomly oriented YBCO grains

will degrade the tape performance considerably. Agreement between J_c and X-ray results show that the temperature ramp-up rate during conversion is a parameter that has to be considered if high-performance coated conductors are to be fabricated by ex situ techniques. Depending on the furnace design, the need to reduce the ramp-up rate and avoid random YBCO formation may place a limit on sample throughput unless the ramp-up temperature gradient can be lowered.

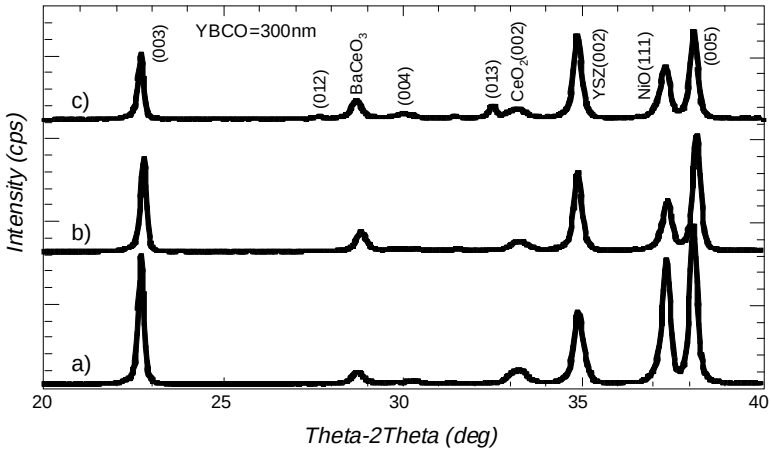

Fig. 1.21. θ-2θ scans of samples converted continuously at (a) tape speed = 0.86 m/h, ramp-up rate = 45°C/min, wet conversion time = 90 min; (b) tape speed = 1.3 m/h, ramp-up rate = 68°C/min, wet conversion time = 60 min; (c) tape speed = 1.73 m/h, ramp-up rate = 90°C/min, wet conversion time = 45 min.

Following the initial runs, a 1-cm-wide by 30-cm-long tape cut from the same batch was continuously converted in the seven-module reel-to-reel chamber at a tape traveling speed of 0.7 m/h. A silver cap layer was sputtered onto the sample for voltage and current contacts after conversion. An end-to-end J_c measurement was performed at 77 K and self-field, which provided a disappointingly low J_c of 10 kA/cm^2. To determine the location(s) of the inferior YBCO film, sectional J_c measurements were conducted at 1-cm increments; the result is shown in Fig. 1.22. It can be seen from this figure that most of the J_cs in this tape range from ~100 to ~300 kA/cm^2, with a maximum sectional value of 400 kA/cm^2. Large portions of this tape can sustain a good J_c; the origin of the low end-to-end J_c can be traced to sections between 7 and 11 cm of the YBCO film. Following J_c measurements, the Ag cap layer was chemically etched away so that the poor-quality sections in question could be examined. An optical picture of this low-J_c portion of tape is shown in Fig. 1.23; it is immediately evident that linear features that run across the entire width of the sample can be located at the low-J_c sections. The locations of these features correspond exactly to places where significant discharges occurred during precursor deposition. When a sizable discharge occurred, the system was shut down and the e-beam vacuum chamber had to be vented to air and the system cleaned. Although the inferior sections can be traced to discharge locations, the reason for the low J_cs is not immediately clear.

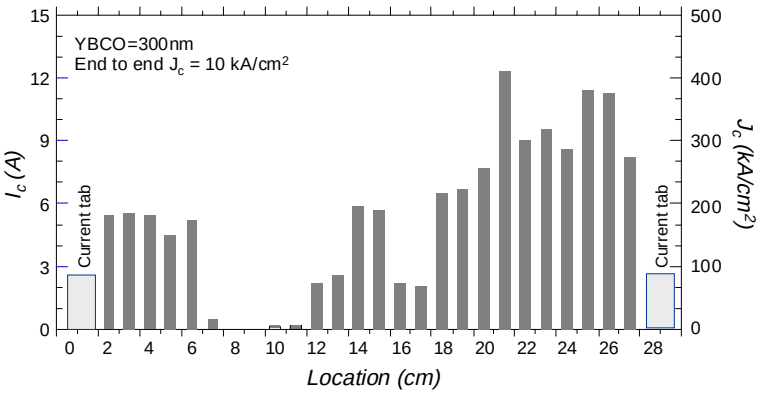

Fig. 1.22. Sectional J_cs of the 30-cm-long YBCO (ORNL,m)-precursor(ORNL,m)/CeO_2(ORNL,m)/ YSZ(ORNL,m)/CeO_2(3M,m)/Ni(3M,m) sample at 77 K and self-field. Low J_c values are located between 7- and 11-cm sections in the YBCO film.

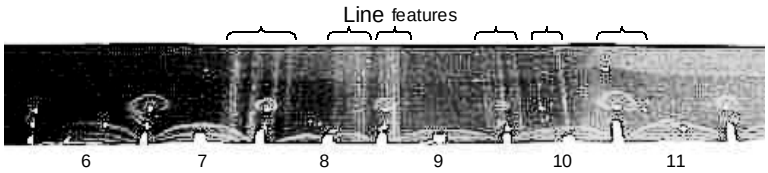

Fig. 1.23. Optical image of the YBCO tape containing low-J_c sections. The linear features running across the entire width of the tape correspond exactly to locations where discharges and accompanying system shutdown occurred during precursor deposition.

Even though SEM imaging of these features revealed an insulating granular surface structure, RBS simulation did not show any significant variation in local Y/Ba/Cu composition. Although the exact cause of these features is not known at this time, the results point toward the need to improve the operational stability of the precursor deposition system and to avoid system shutdown during deposition.

Following the largely successful conversion of the 30-cm tape, a 1-cm-wide by 1-m-long precursor sample (ORNL,m)/CeO_2(ORNL,m)/YSZ(3M,m)/CeO_2(3M,m)/Ni(3M,m) was prepared and was continuously converted at a tape traveling speed of 0.65 m/h. The appearance of the tape was carefully examined following conversion. Because no discharge had occurred during precursor deposition, no linear features similar to those shown in Fig. 1.23 were found. There was, however, a grayish region located at the gas outlet edge of the tape, a typical example of which is shown in Fig. 1.24. This feature was found along the entire length of the tape, although its width varied from location to location. XRD analyses revealed that the grayish region was richer in BaF_2 when compared with the gas inlet edge and the center of the tape. This variation in BaF_2 content indicates nonuniform oxyfluoride decomposition. A possible contributing factor to the decomposition inhomogeneity, even across this reduced-length scale, may arise from the upward curvature of the sample. Because a typical one-sided coated conductor is an anti-symmetric composite, sample curvature across the tape width will result, owing to the different thermal expansions and stress states of YBCO, buffer(s), and metallic substrate. The sample curvature can be quite pronounced, especially when a soft substrate such as annealed Ni is used.

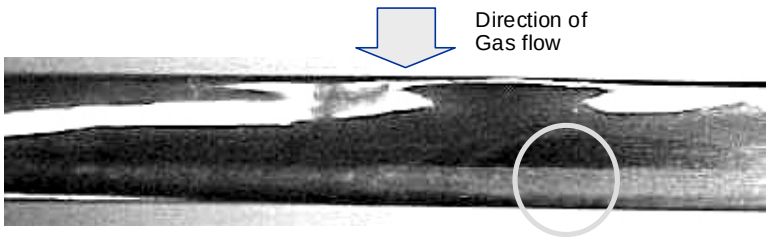

Fig. 1.24. A grayish region is found at the gas outlet edge of the 1-m-long YBCO(ORNL,m)-precursor(ORNL,m)/CeO_2(ORNL,m)/YSZ(3M,m)/CeO_2(3M,m)/Ni(3M,m) sample. The width of this BaF_2-rich region varied from location to location but can be seen along the entire length of the tape.

The influence of sample curvature on gas-flow profile was investigated by computational fluid dynamics simulations. Dimensions and mesh setup of the simulated reaction chamber were identical to those of the previous study, except that a curvature was introduced across the width of the sample (see Fig. 1.25). It can be seen in Fig. 1.25 (a) that gas flow at the vicinity of the curved surface is symmetric around the middle of the sample, just as in the case of a flat tape. However, along the precursor side (top surface) of the curved sample, gas velocities at the leading and trailing edges of the tape are now lower than that of the middle portion, owing to the increased local clearance between sample surface and chamber wall. The HF/H_2O concentration ratio at the trailing edge of such a curved sample will likely be higher, resulting in slower oxyfluoride decomposition/YBCO conversion as seen in Fig. 1.24.

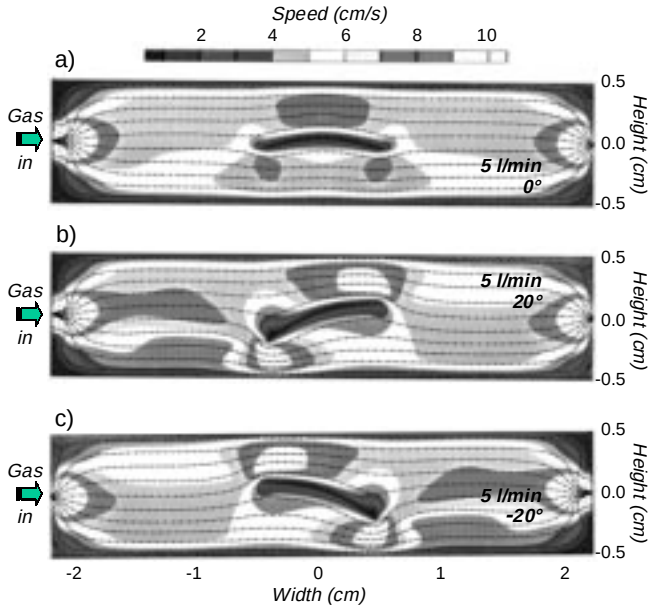

Fig. 1.25. Simulated flow profile of a curved sample within the transverse cross section of a transverse-flow reaction chamber. Flow rate of the gas is 5 L/min for a sample that is (a) leveled along the horizontal plane of the chamber, (b) tilted 20° toward the gas inlet, and (c) tilted 20° away from the gas inlet.

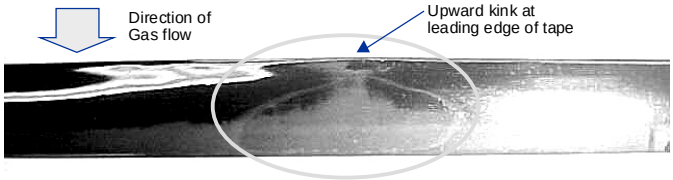

Fig. 1.26. Section of the meter-long tape that contains an upward kink at the leading edge of the sample. Flowing gas was channeled around the flaw, leading to deposition of incompletely converted material, which fanned out behind the obstacle.

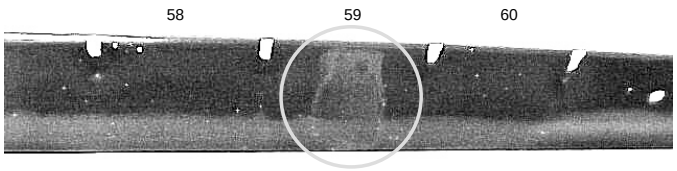

Fig. 1.27. Section of the meter-long tape that contains an imperfection in YBCO located 59 cm from the front of the tape. This blemish is not believed to be the result of anomalies during deposition or conversion.

Because the annealed Ni substrate is very soft, flaws such as kinks and nicks can result from mishandling. Local orientation of tape at and adjacent to such flaws would frequently deviate from that shown in Fig.1.25 (a). Rather, sections of tape can tilt toward or away from the gas inlet, depending on the type and directionality of the flaw. When the sample is tilted away from the gas inlet, gas velocity at the trailing edge of the tape will decrease further, leading to a greater tendency toward incomplete decomposition/conversion. This tendency can account for the varying width of the incompletely converted region along the length of the tape. More striking is the extent of incomplete conversion at the location of the flaw. Figure 1.26 shows a section of the meter-long tape containing an upward kink caused by tape-to-reel contact. This type of flaws not only tilts the sample away from the gas inlet but also acts as an obstacle that channels the gas to either side, resulting in incompletely reacted material that fans out from the flaw.

In addition to these general features, one other blemish was found at a location 59 cm away from the front of the tape (see Fig. 1.27). This imperfection was first noticed before precursor deposition and does not conform to the shape or the appearance of known flaws generally associated with precursor deposition and conversion. In addition, a priori local X-ray analyses confirmed that the spot is not associated with degradation in the texture of either the Ni or the buffer. Rather, the appearance of the spot led us to believe that it was the consequence of contamination by cleansing solvent after buffer deposition and that it could be avoided by improving care in tape handling.

To evaluate the current-carrying capability of the long tape, a silver cap layer was sputtered onto the YBCO surface, and the meter-long tape was cut into two sections (93 cm and 7 cm) because of the limited length of our oxygen annealing furnace. End-to-end J_c measurement was performed at

77 K and self-field on the 93-cm-long tape with a voltage separation distance of 89 cm. The end-to-end J_c was found to be 100 kA/cm^2, based on the 1-μV/cm criterion, even though voltage first appeared at a current density of 33 kA/cm^2. Sectional J_c measurements were performed next to study the J_c uniformity of the sample. Because our sectional J_c apparatus is limited to 30-cm-long samples, the 93-cm tape was cut into three sections. Sectional J_c values of these plus the 7-cm section are reconstructed and shown in Fig. 1.28. It can be seen from this figure that the section of YBCO film located 59 cm from the front of the tape possesses a low J_c value of 33 kA/cm^2. This corresponds exactly to the imperfection seen in Fig. 1.27 and to the current-density value where voltage was first detected in the end-to-end measurement; it is the cause of the low overall J_c of the long tape. Other than this low-J_c spot, the sectional J_c values of the entire meter-long tape are quite good; J_c ranges from ~300 to ~770 kA/cm^2 (see Fig 1.28). The variation in sectional J_c corresponds qualitatively to the width of the incompletely converted region found at the gas outlet edge of the sample, which is believed to be a major contributor to the J_c nonuniformity. The maximum attained J_c of 770 kA/cm^2 is similar to that of a short (1.5-cm-long) sample cut from the same stock and previously converted in a standard longitudinal-flow furnace, and meets the best expected performance based on the texture of the RABiTS™. While portions of this long tape possess excellent J_c, the relatively large variation in the sectional J_c values indicates that there is much room for improvement through process optimization and possible modification in reaction chamber design.

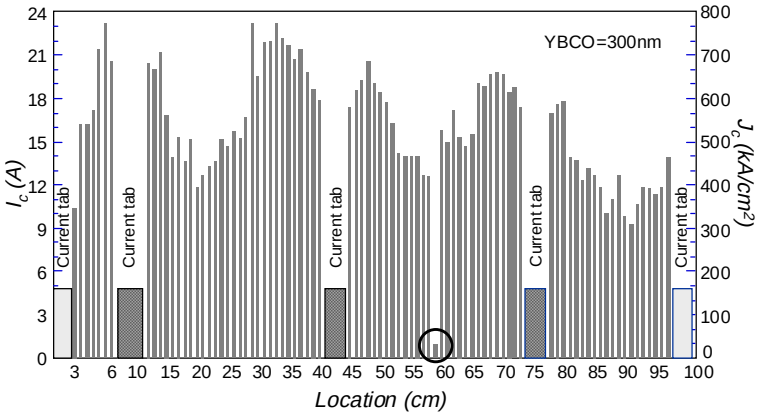

Fig. 1.28. Sectional J_cs of the meter-long YBCO(ORNL,m)-precursor(ORNL,m)/CeO_2(ORNL,m)/YSZ(3M,m)/CeO_2(3M,m)/Ni(3M,m) sample at 77K and self-field. The sample was cut into shorter sections after conversion due to the dimensional constraints of our oxygen-annealing and measurement equipment. Low J_c value is located 59 cm from the front of the sample and is highlighted by a circle.

To further explore the origins of the J_c inhomogeneity as well as the low-J_c section in the long sample, we made use of the correlation between X-ray characteristics and J_c found previously in the design-of-experiment results. For this task, we utilized our unique reel-to-reel XRD system, which was designed especially for the coated-conductor work.[26] The system, shown in Fig. 1.29, consists of a large four-circle diffractometer, a modular reel-to-reel insert for tape positioning, an X-ray source and detector, and standard computerized controls. At present, the nominal tape traveling speed is 200 m/h when the system is operating in a moving θ-2θ scanning mode at a fixed diffraction angle. This unique facility

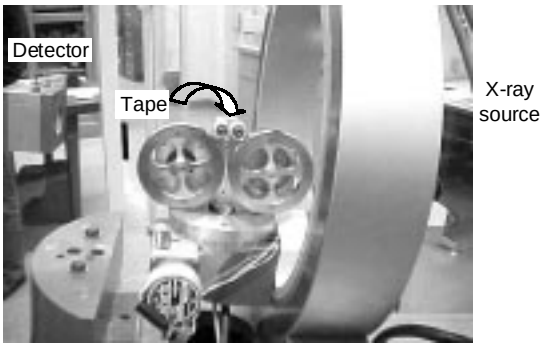

Fig. 1.29. First-generation reel-to-reel X-ray diffraction system at ORNL. Photo shows the large 4-circle diffractometer together with the modular reel-to-reel insert and location of the tape section being examined.

provides an opportunity to study relative changes in X-ray characteristics at various locations of a long tape; an investigation such as this is extremely difficult for short samples due to batch-to-batch variability. The reel-to-reel system has proven to be invaluable in the development of RABiTS™. To prepare the long YBCO(ORNL,m)-precursor(ORNL,m)/CeO_2(ORNL,m)/YSZ(3M,m)/CeO_2(3M,m)/Ni(3M,m) sample for reel-to-reel X-ray characterization, silver cap layers were chemically etched off the three tape sections originally cut from the 93-cm sample. The sections were then spot-welded together with Ni spacers in between to account for sample loss during cutting and welding. The reconstructed tape was loaded into the X-ray reel-to-reel insert, and two moving scans were performed at diffraction angles corresponding to YBCO(005) and YBCO(103). Figure 1.30 shows the changes in YBCO(005) and YBCO(103) diffraction intensities together with sectional I_c. Zero X-ray intensity values seen near 5, 40, 75, and 95 cm in the plot correspond to the Ni spacers where no YBCO was present. It can be seen from the figure that, as there was in the results of the design-of-experiment study, there is a good correlation between YBCO(005) intensity variation and the relative changes in measured sectional I_c values. There is a local intensity minimum at 59 cm (where the imperfection was identified), and another minimum of similar intensity, which can be seen at 21 cm, exhibited an I_c of ~12 A. Thus, YBCO(00*l*) intensity is a good but insufficient gauge of ultimate tape performance. Also shown in Fig. 1.30 is the variation in YBCO(103) intensity along the length of the reconstructed tape; one can see that a single maximum, which indicates the presence of a sizable amount of randomly oriented YBCO grains, corresponds exactly with the identified imperfection of low I_c. Thus, while YBCO(00*l*) intensity indicates the quality and formation of epitaxial YBCO, YBCO(103) intensity can show the locations where breakdowns in YBCO epitaxy occur. Used together, these measurements may provide a powerful on-line feedback parameter to optimize and control the quality of YBCO coated conductors processed ex situ.

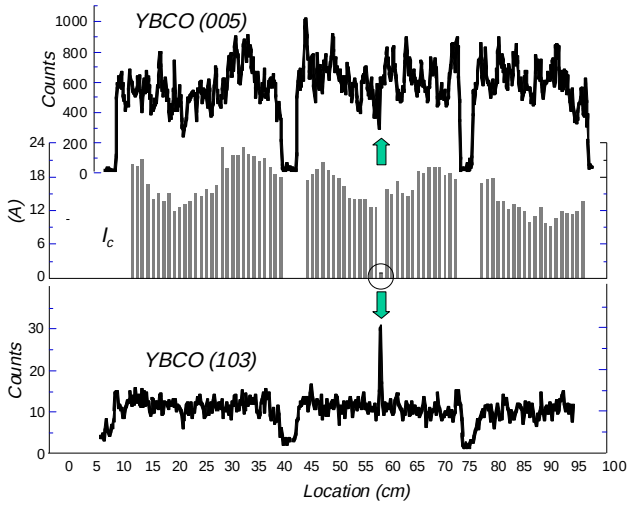

Fig. 1.30. Variations in YBCO(005) and YBCO(103) X-ray intensities with tape location. Also shown is the corresponding I_cs of the reconstructed tape. Arrows mark the locations of YBCO(005) minimum and YBCO(103) maximum. These anomalies occur exactly at the spot where the I_c is low and the identified imperfection is present.

1.2.6 Summary

With the development of flexible biaxially textured substrates, fabrication of long-length, high-J_c coated conductors may be possible. Ex situ processing of epitaxial YBCO, which separates YBCO compositional control from the epitaxial growth step, is an attractive alternative to traditional vapor deposition techniques. Early on in our investigation of long-length ex situ conversion of BaF_2 precursor on RABiTS™, we found that YBCO conversion is inhomogeneous when a simple longitudinal-flow reaction chamber is used. It is our belief that the HF/H_2O concentration ratio near the sample surface must remain low. Because BaF_2 or oxyfluoride has to decompose totally and efficiently for YBCO conversion

to proceed to completion. That is, HF has to be effectively removed from the sample following oxyfluoride decomposition. As such, an increase in gas flow rate should aid in the removal of HF.

To verify these assumptions, we performed numerical fluid dynamics simulations to visualize the gas-flow profile of a sample suspended in a transverse-flow chamber. In addition, simulations were performed to study the effects of flow rate on both gas velocity and HF concentration in the vicinity of the sample. Simulated results revealed that the gas flow is symmetric around the middle of the sample, with higher gas velocities at the leading and trailing edges. More importantly, the results showed that gas velocity is significantly increased at all locations near the sample surface when a higher flow rate is utilized. Therefore, a higher flow rate should aid in the removal of HF. This was verified in the HF concentration simulations, which revealed that while the highest HF concentration is always located at the surface along the downstream portion of a sample, both the volume and the concentration of HF can be substantially reduced when a higher flow rate is employed.

Based on these results, we selected a two-prong approach that can minimize the nonuniform conversion problem while maximizing the amount of precursor that can be converted at one time. The approach utilizes (1) a transverse-flow geometry in which the effective conversion distance is the sample width and (2) an extended conversion zone to maximize the volume of material undergoing the oxyfluoride decomposition/YBCO conversion reaction. To validate this approach, an extended single-module transverse-flow reaction furnace capable of high flow rates was designed and built. To ensure the mechanical integrity and dimensional stability of the reaction chamber, Inconel 601 was chosen as the building material. Because the chamber is located in a single-zone furnace, continuous conversion of YBCO is not possible, and the furnace essentially operates in a stationary mode. A design-of-experiment study was performed on short samples to investigate the effects of flow rate and conversion time on the characteristics of YBCO processed in the furnace. The results showed that YBCO(00*l*) X-ray intensity increases gradually with conversion time at slow flow rates. At higher flow rates, the X-ray intensity initially increases rapidly, reaches a maximum value, and then decreases on further exposure to the moist conversion environment. The variation in J_c with flow rate and conversion time for these samples is remarkably similar to that of YBCO(00*l*) X-ray intensity. These results suggest that an efficient atmospheric reaction chamber should be able to sustain significant gas flow because the time that is necessary to completely convert a length of YBCO at low flow rates may be impractical. The results also showed that, for a given furnace design, an optimum growth rate exists, above which degradation in grain quality or texture can occur. Moreover, the similarity between YBCO(00*l*) X-ray intensity and J_c suggests that relative changes in YBCO X-ray intensity may be used as a feedback parameter to optimize the J_c during ex situ processing.

Once the operation of the metallic single-module reaction chamber was validated, we proceeded to build a seven-module version of the reaction chamber. Inconel 601 was again chosen as the building material. (After 1 year of operation, the monitored flow parameters and the ability of the single-module chamber to convert YBCO have remained constant, thus validating Inconel 601 as an excellent building material.) The 2.5-m-long chamber sits in the cradle of a 2-m-long 22-zone furnace and is connected to two reels, thus enabling the continuous conversion of long-length YBCO. Preliminary studies of precursor conversion of short samples on a moving substrate showed that randomly orientated YBCO can result if a large temperature ramp-up rate is employed. When a sizable amount of random YBCO is present, the YBCO film possesses a very low J_c. Therefore, this influence of ramp-up rate on YBCO nucleation may place a limit on sample throughput unless the thermal gradient of a chosen furnace can be adjusted. Once the basic conversion parameter space of the seven-module furnace was known, a 30-cm-long sample was converted in a continuous manner. The YBCO film was found to contain linear features at certain locations that run across the width of the sample. These locations support little or no J_c and

correspond exactly to sites where significant discharges occurred during precursor deposition and when the system was shut down. While the end-to-end J_c of the processed sample is low, the majority of the sectional J_cs is satisfactory, which gave us the impetus to process longer tapes. A 1-m-long BaF_2 precursor on RABiTS™ was thus converted next. Careful examination of the YBCO appearance following conversion revealed that a BaF_2-rich region was present at the gas outlet edge along the entire length of the meter-long tape. The width of this BaF_2-rich region varied from location to location, and is believed to be the result of incomplete oxyfluoride decomposition/YBCO conversion stemming from sample curvature and flaws due to tape mishandling. In addition, a blemish could be seen visually, which is not believed to be the result of anomalies during buffer/precursor deposition or film conversion. Rather, it is believed that contamination of the tape occurred during sample transfer and thus should be possible to avoid in the future. End-to-end J_c of the meter-long tape sample was found to be 100 kA/cm^2; the less-than-stellar value was due to the low J_c at the blemish spot. Other than this ~0.6-cm-wide low-J_c spot, sectional measurements at 1-cm increments revealed J_cs that range from 300 to 770 kA/cm^2. Reel-to-reel X-ray scans of the sample showed that variation in J_c along the length of the tape corresponds qualitatively to the relative change in YBCO(00*l*) intensity. In addition, a sudden increase in YBCO(103) intensity is seen at the blemish spot. These results fortify the suggestion that X-ray measurements at selected diffraction angles may be used during sample conversion to optimize tape performance. Results obtained in this study also provide pathways to further improve the conversion process through modifications on items such as gas-delivery design and tape-transfer protocol.

1.2.7 References

1. Y. Iijima et al., "In-Plane Aligned $YBa_2Cu_3O_{7-x}$ Thin Films Deposited on Polycrystalline Metallic Substrates," *Appl. Phys. Lett.* **60**, 769 (1992).

2. R. P. Reade et al., "Laser Deposition of Biaxially Textured Yttria-Stabilized Zirconia Buffer Layers on Polycrystalline Metallic Alloys for High Critical Current Y-Ba-Cu-O Thin Films," *Appl. Phys. Lett.* **61**, 223 (1992).

3. W. D. Wu et al., "Properties of $YBa_2Cu_3O_7$ Thick Films on Flexible Buffered Metallic Substrates," *Appl. Phys. Lett.* **67**, 2397 (1995).

4. M. Bauer et al., "Large Area YBCO Films on Polycrystalline Substrates with Very High Critical Current Densities," *IEEE Tran. Appl. Supercond.* **9**(2), 2244 (1999).

5. A. Goyal et al., "Fabrication of Long Range, Biaxially Textured, High Temperature Superconducting Tapes," *Appl. Phys. Lett.* **69**, 1795 (1996).

6. D. P. Norton et al., "Epitaxial $YBa_2Cu_3O_7$ on Biaxially-Textured (001) Ni: an Approach to High Critical Current Density Superconducting Tapes, *Science* **274**, 755 (1996).

7. T. Petrisor et al., "Development of Biaxially Aligned Buffer Layers on Ni and Ni-Based Alloy Substrates for YBCO Tapes Fabrication," *IEEE Tran. Appl. Supercond.* **9**(2), 2256 (1999).

8. R. P. Wang et al., "Deposition of High-Temperature Superconducting Films on Biaxially Textured Ni(001) Substrates," *Physica C* **33,** 87 (2000).

9. M. Fukutomi et al., "Laser Deposition of $YBa_2Cu_3O_y$ Thin Films on a Metallic Substrate with Biaxially Textured YSZ Buffer Layers Prepared by Modified Bias Sputtering," *Physica C* **219**, 333 (1994).

10. M. Bauer, R. Semerad, and H. Kinder, "YBCO Films on Metal Substrates with Biaxially Aligned MgO Buffer Layers," *IEEE Tran. Appl. Supercond.* **9**(2), 1502 (1999).

11. J. E. Mathis et al., "Biaxially Textured $YBa_2Cu_3O_{7-\delta}$ Conductors on Rolling Assisted Biaxially Textured Substrates with Critical Current Densities of 2–3 MA/cm^2, *Jap. J. Appl. Phys. Lett. Part II* **37** L1379 (1998).

12. A. Ignatiev et al., "Photo-Assisted MOCVD Growth of YBCO Thick Films for Wire Applications, *Appl. Supercond*. **4**, 455 (1996).

13. V. Selvamanickam et al., "High-Current Y-Ba-Cu-O Superconducting Films by Metal Organic Chemical Vapor Deposition on Flexible Metal Substrates, *Physica C* **333**, 155 (2000).

14. M. Paranthaman et al., $YBa_2Cu_3O_{7-y}$–Coated Conductors with High Engineering Current Density, *J. Mater. Res.* 15: 2647 (2000).

15. D. M. Feldmann et al., "Magneto-Optical Imaging of Transport Currents in $YBa_2Cu_3O_{7-x}$ on RABiTS™," presented at ASC2000, Virginia Beach, Va., to be published *in IEEE Tran. Appl. Supercond*.

16. M. W. Rupich et al., "Low Cost Y-Ba-Cu-O Coated Conductors," presented at ASC2000, Virginia Beach, Va., to be published *in IEEE Tran. Appl. Supercond*.

17. S. R. Foltyn et al., "High-T_c Coated Conductors – Performance of Meter-long YBCO/IBAD Flexible Tapes," *IEEE Tran. Appl. Supercond.* **9**(2), 1519 (1999).

18. Y. Iijima et al., "Development of Y-123-Coated Conductors by IBAD Process," *Physica C* **335**, 15 (2000).

19. Y. Sato et al., "Development of $YBa_2Cu_3O_y$ Tape by Using Inclined Substrate Method," presented at ASC2000, Virginia Beach, Va., to be published *in IEEE Tran. Appl. Supercond*.

20. V. F. Solovyov et al., "Kinetics of $YBa_2Cu_3O_7$ Film Growth by Postdeposition Processing," *Appl. Phys. Lett*. **76**, 1911 (2000).

21. J. A. Smith, M. J. Cima, and N. Sonnenberg, "High Critical Current Density Thick MOD-Derived YBCO Films," *IEEE Tran. Appl. Supercond.* **9**(2), 1531 (1999).

22. R. Feenstra et al., An ex situ Processed YBCO Coated Conductor," in *Proc. 1999 DOE Superconductivity Program for Electric Systems Annual Peer Review* **1**, 361 (1999).

23. W. B. Robbins, private communication.

24. X. Cui et al., "Continuous Growth of Epitaxial CeO_2 Buffer Layers on Rolled Ni Tapes by Electron Beam Evaporation," *Physica C* **316**, 27 (1999).

25. D. F. Lee et al., "Progress in Scaling up YBCO-Coated Conductor on RABiTS™ Using the BaF_2 Precursor Approach," pp. 1-33–1-36 in *ORNL Superconducting Technology Program for Electric Power Systems: Annual Report for FY 1999*, ORNL/HTSPC-11, Oak Ridge National Laboratory, Oak Ridge, Tenn. (2000).

26. F. A. List, "Progress Toward Continuous Processing of YBCO/RABiTS™ Tape," pp. 136–1-38 in *ORNL Superconducting Technology Program for Electric Power Systems: Annual Report for FY 1999*, ORNL/HTSPC-11, Oak Ridge National Laboratory, Oak Ridge, Tenn. (2000).

27. S. W. Lu et al., "Electron Beam Co-Evaporation of Y-BaF_2-Cu Precursor Films for $YBa_2Cu_3O_7$ Coated Conductors" (manuscript in preparation).

1.3. ENHANCING THE CRITICAL CURRENT OF EX SITU YBCO COATED CONDUCTORS

R. Feenstra, B. W. Kang, A. Goyal, M. Paranthaman, D. F. Lee, P. M. Martin, D. K. Christen, and D. M. Kroeger, ORNL; P. N. Arendt, J. R. Groves, and R. F. DePaula, Los Alamos National Laboratory

A key parameter describing the performance of HTS wires is the critical current (I_c). Normalized to a width w of 1 cm, $K_c = I_c/w$ provides the link between intrinsic properties of the superconductor expressed by the critical current density (J_c) and the actual demands of the application sphere. K_c is related to J_c through the expression $K_c = J_c \times d$, where d is the thickness of the conductor. To reach a certain high-K_c

target one may increase the thickness of the conductor or, if possible, improve the intrinsic behavior (i.e., improve J_c).

These basic considerations acquire a new significance for coated conductors due to the specific conductor architecture and the novel processing involved. Unlike earlier technology featuring multifilamentary wire, the active cross section is not simply a function of macroscopic parameters such as the filament diameter or the number of filaments per conductor; rather, through the epitaxial superconductor (YBCO) coating, it is intimately related to a complex and labor-intensive process. The thickness *d* corresponds directly to the thickness of the epitaxial layer, independently of the method used to produce the YBCO or the configuration, in the form of a single thick coating, or multiple coatings on a single or multiple strands of tape. Due to rate limitations of the epitaxial growth there exists a minimum time to "build up" the YBCO coating to the (total) thickness *d*, creating a performance-dependent production rate. On the other hand, the thickness also controls intrinsic properties of the YBCO (i.e., J_c) because the structural properties of newly deposited layers depend on the quality of the existing template during the epitaxial growth. The result is a complex relation between production rate and cost whereby, to meet a given K_c criterion, considerations such as substrate quality and cost significantly enter into the analysis. Depending on the $J_c(d)$ dependence, either a multi-tape configuration with thin YBCO or single tape with thick YBCO deposit could be the most economical solution.

A target set forth by DOE for YBCO coated conductors is 1000 A/cm (at 77 K). This may be achieved as a double-sided conductor with each side having K_c = 500 A/cm. The 500-A/cm target for a single coating represents an aggressive target that will require significant advances in substrate and YBCO film-growth technology. The following analysis illustrates this point.

A J_c value that may be reproducibly obtained for thin YBCO on single-crystal substrates is $J_c \cong$ 4–5 MA/cm^2. Grain boundaries propagating from the biaxially textured substrate into the YBCO reduce the J_c of coated conductors. The reduction for the early coated conductors was as large as a factor of 10 to 20; more common for recent conductors is a reduction factor of 1.5 to 4 with J_c = 1 MA/cm^2 being a widely adopted landmark. The crystal-substrate performance defines the minimum YBCO thickness to meet the 500-A/cm target. This minimum is about 1 to 1.5 μm; however, it increases to about 2 to 5 μm for coated conductors, depending on the texture. In this thickness range growth-induced roughening effects in the YBCO likely come into play, and the desired c⊥ epitaxy is more difficult to maintain. A decreasing $J_c(d)$ dependence typically results; however, little is known for a given YBCO process about the specific causes of the J_c reduction. The present report provides an inventory of the status for the ex situ BaF_2 process for YBCO epitaxial growth, which is one of the leading processes being considered for coated-conductor implementation.

A key feature of the ex situ BaF_2 process is the separation (in time) between the material-accumulation and epitaxial-growth functions of the overall YBCO deposition process. Significant advantages for large-scale production are expected from this separation because of the simplified constraints on the physical processes producing the precursor layer (material accumulation) and the possibility to process large amounts of material at once during the post-deposition ex situ anneal. It is during this anneal that the rate-limiting step of forming the YBCO epitaxial structure takes place, controlled by a decomposition reaction of BaF_2 with H_2O vapor injected into the annealing chamber. Compatibility of the ex situ BaF_2 process with RABiTS™ and IBAD-YSZ coated conductor substrates previously was demonstrated using YBCO coatings with a fixed thickness of 0.3 mm. The optimized processing conditions for this demonstration took account of the different surfaces provided by these substrates compared to standard single crystal $SrTiO_3$ (STO); compatibility has been extended by at least a factor of 10 in the YBCO thickness with no apparent substrate degradation in the course of the prolonged ex situ anneals (lasting up to 8 h for some of thickest films).

Results from a comparative study in which YBCO coatings of various thicknesses were produced by either the ex situ BaF_2 process or in situ PLD are presented in Fig. 1.31. The RABiTS™ used for both processes consisted of rolled Ni tape supplied by an outside vendor according to ORNL specifications and produced in large quantities (>300 m) through a continuous, industrial-scale process. Short sections were cut from this tape and were annealed at ORNL to produce the biaxial texture. Buffer layers consisted of reactively grown CeO_2 or Y_2O_3 seed layers capped with YSZ/CeO_2 bilayers to establish compatibility with the YBCO.

From an apparent maximum K_c of ~30 A/cm for 0.3-mm-thick YBCO ($J_c \cong 1$ MA/cm^2), Fig. 1.31 indicates a near-linear increase of the critical current with thickness for either deposition technique, reaching ~115 A/cm for a 1.6-μm coating produced by the ex situ process and a slightly higher value of ~135 A/cm for a 3-μm film produced by in situ PLD. Significant process modifications were introduced for the ex situ YBCO process in the course of this study to access the thick-film regime. The enhanced thickness of the precursor layer apparently modified the kinetics of initial YBCO phase formation and mandated changes beyond a simple extension of the annealing duration. Similar changes were not required for the in situ PLD coatings, which were processed for the most part under identical conditions. Considering the preliminary nature of this research, the agreement between results for the two techniques is satisfactory.

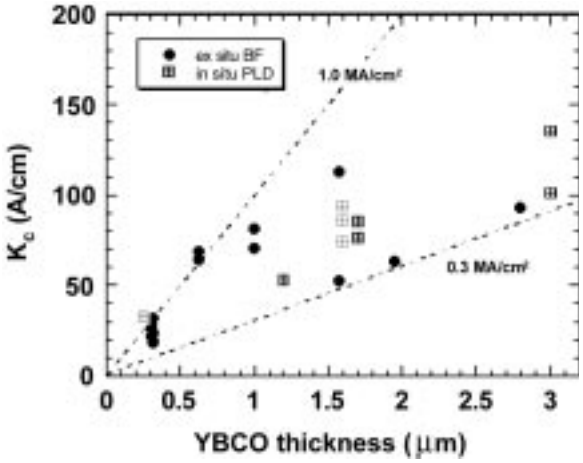

Fig. 1.31. Critical current per centimeter width of YBCO coatings produced by the ex situ BaF_2 process and in situ PLD on RABiTS™ featuring commercially produced Ni tape. Dashed lines mark expected K_c increase for constant values of the critical current density (J_c) as indicated. All data are at 77 K and self-field.

Effects related to texture and thickness for the ex situ process are compared in Fig. 1.32; the intrinsic parameter, J_c, rather than K_c, is plotted as a function of the thickness for ex situ YBCO on a range of substrate materials, including STO and YSZ single crystals (the latter provided with a thin CeO_2 cap layer), IBAD-YSZ (also with thin CeO_2 cap), and RABiTS™. The data for YBCO on commercial Ni are included in Fig. 1.31 for comparison. Lines of constant K_c assume a hyperbolic shape in this representation ($J_c = K_c/d$), and three such lines have been included for the criteria 100, 300, and 500 A/cm.

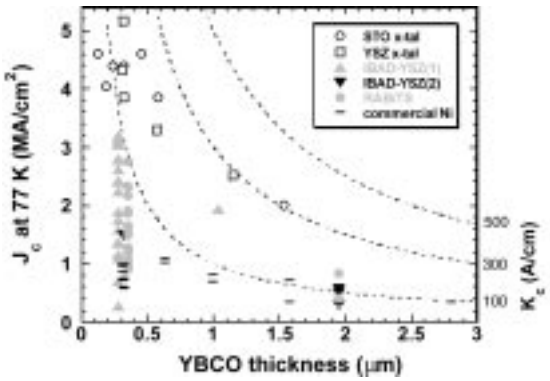

Fig. 1.32. Thickness dependence of the critical current density (J_c) of ex situ YBCO on single-crystal and buffered metal substrates. Symbols indicate the different substrates. RABiTS™ and IBAD-YSZ(1) data at 0.3 μm YBCO thickness have been slightly shifted for clarity. Dashed lines indicate J_c required to meet indicated K_c criteria of 100, 300, and 500 A/cm. All data are at 77 K and self-field.

The large data set for 0.3-μm YBCO illustrates previous work testing compatibility of the ex situ BaF_2 process with coated conductor substrate tapes as well as investigation of effects related to texture.

The RABiTS™ data selected for Fig. 1.32, with J_c between 0.8 and 2.7 MA/cm^2, reflect variations induced by a number of parameters, including metallic content of the substrate tape (pure Ni vs Ni alloys), buffer-layer architecture (chemistry of the seed layer grown directly on the Ni), YBCO processing parameters, and variations in the Ni texture. Clear correlations with these parameters can be discerned in side-by-side comparisons.

A more purely texture-related variation is indicated by the data labeled "IBAD-YSZ(1)." In a design experiment at LANL, a long (30-cm) IBAD tape was produced by a linear ion gun operated in a stationary mode with respect to the tape. Subtle variations in ion yield and beam divergence produced a continuous range of texture variations in the IBAD-YSZ along the length of the tape, indicated by a varying $\Delta\Phi$ (width of the in-plane texture measured by XRD). YBCO coatings were epitaxially grown on short sections cut from this tape; each precursor was processed in identical manner. A systematic correlation between J_c and the original position on the IBAD tape resulted, producing a systematic correlation between J_c and $\Delta\Phi$ (in the YBCO). The highest $J_c \cong 3.0–3.2$ MA/cm^2 (corresponding to $K_c \cong 90$ A/cm). Thus it correlated with the best texture of the IBAD-YSZ, whereas successively lower J_cs resulted for coatings with broader in-plane distributions.

Thick YBCO on select substrates with improved biaxial texture produced the highest K_c achieved thus far. In particular, a high K_c of 200 A/cm resulted for 1-μm YBCO ($J_c = 2.0$ MA/cm^2) on a section of IBAD-YSZ that was cut from the same part of the tape producing $J_c \geq 3$ MA/cm^2 in 0.3-mm YBCO. Tripling the YBCO thickness on this substrate effectively doubled K_c. A similarly large K_c enhancement resulted on RABiTS™ with texture quality indicated by $J_c = 1.6$ MA/cm^2 in 0.3-μm YBCO ($K_c \cong$ 48 A/cm). A 1.95-μm-thick coating on this substrate carried $K_c \cong 164$ A/cm, exceeding the performance of any of the coatings on the commercial Ni. A 1.95-μm-thick coating on IBAD-YSZ cut from a second tape with broader in-plane texture gave $K_c \cong 110$ A/cm. This IBAD tape produced a maximum $J_c \cong$ 1.5 MA/cm^2 in 0.3-μm YBCO.

Although J_c decreases with thickness for all the substrate materials considered in this study, the overall level appears to be set by the texture quality. This texture quality is reflected in the J_c measured for thin films (0.3 μm), which serves effectively as an indicator and "starting point" of any subsequent thickness dependence $J_c(d)$ or $K_c(d)$. Indeed, the rate at which K_c initially increases with the YBCO thickness is given by the J_c of thin coatings. To what extent texture-related effects have the same magnitude in thick YBCO is open to further investigation. The texture-induced J_c variation shown in Fig. 1.32 for optimally processed 0.3-mm coatings on IBAD-YSZ is about a factor of 10. At greater thickness, however, growth-induced and texture-related effects on J_c are superimposed, which would suggest a weaker role of texture alone. The rate at which J_c decreases with thickness thus is probably the strongest for substrates with the best texture.

The data hold promise that critical currents at the levels $K_c \cong 300$ A/cm or 500 A/cm may be feasible if the ex situ BaF_2 process is used. In particular, we expect that 2- to 3-μm-thick coatings on highly textured substrates (or thicker coatings on intermediate-texture substrates) should enable performance at the 300-A/cm level. Although short of the DOE target, this performance would match that of high-quality BSCCO tape (~100 A for a 3.5-cm-wide conductor) and could provide an interesting entry level for YBCO coated conductors. Further K_c enhancement to 500 A/cm (in a single YBCO coating) almost certainly will require YBCO coatings of 5 μm thick or more in addition to outstanding texture quality, which may take longer to develop. Considering the increased processing times required for such coatings, the cost-benefit would have to be weighed against the use of multiple tapes with thinner YBCO coatings, each operating at a higher J_c level.

1.4 FABRICATION OF HIGH-J_c TAPES BY EPITAXIAL DEPOSITION OF YBCO ON RABiTS™

A. Goyal, F. A. List, D. F. Lee, E. D. Specht, R. Feenstra, M. Paranthaman, X. Cui, S. W. Lu, P. M. Martin, D. M. Kroeger, D. K. Christen, B. Y. Kang, D. P. Norton, C. Park, D. T. Verebelyi, J. R. Thompson, R. K. Williams, T. Aytug, and C. Cantoni

1.4.1 Reduced Magnetism, Strengthened Substrates

Ni-Cr alloy substrates with Cr contents up to 13at%Cr were fabricated by rolling to deformations greater than 95% followed by annealing at high temperatures to form cube-textured alloy tapes. As expected, it is found that the Curie temperature decreases linearly with Cr addition. Measured Curie temperatures for alloys studied are summarized in the Table 1.2. Also indicated in Table 1.2 are measured yield strengths for the alloys. Tensile tests were performed on cube-textured, laser-machined, dog-bone samples with the stress applied along the [100] crystallographic axis. As can be seen from the table, Ni-13at%Cr alloys are essentially nonmagnetic, whereas Ni-7at%Cr alloys have a Curie temperature only slightly below room temperature. For applications above 40 K, both Ni-11at%Cr and Ni-13at%Cr would be nonmagnetic. With increase in Cr additions, the yield strength increases substantially with the Ni-13at%Cr substrate having a strength almost five times that of pure Ni.

Table 1.2. Measured Curie temperatures and tensile yield strength for Ni-Cr alloys

Composition	Curie temperature (K)	Yield Strength (MPa)
Ni	627	34
Ni-7at%Cr	250	64
Ni-9at%Cr	124	87
Ni-11at%Cr	20	102
Ni-13at%Cr	<4.2	164

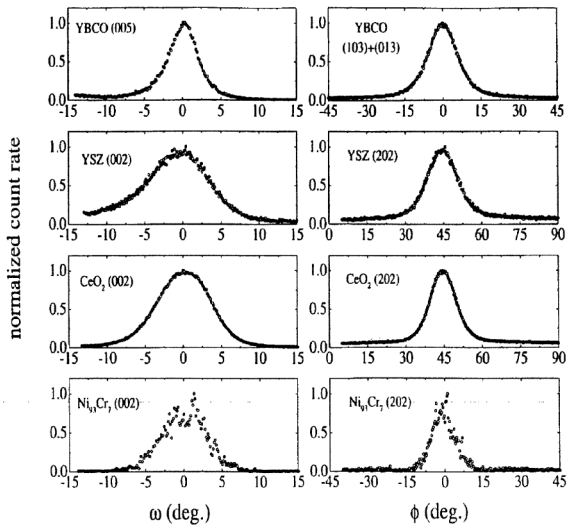

Fig. 1.33. ω-scans and ϕ-scans of oxide multilayers deposited epitaxially on a Ni-7at%Cr substrate by pulsed laser ablation.

For alloys with low Cr contents, epitaxial oxide buffer layers can be epitaxially deposited directly on the substrate under conditions similar to that developed for deposition on Ni. Figure 1.33 shows ϕ-scans and ω-scans of oxide multilayers deposited epitaxially on a Ni-7at%Cr substrate by pulsed laser ablation. Scanning electron microscopy (SEM) shows that the film is relatively dense and crack-free. The critical current density was 223,000 A/cm^2 at 77 K and 0 T.

Even though relatively good epitaxy is obtained in a significant part of the substrate, it is expected that localized oxidation and formation of chromium oxide is a problem. This issue becomes significant for substrates with higher chromium content. Typically, the deposition of oxide layers on biaxially textured Ni is performed under conditions in which NiO is thermodynamically unstable, whereas the oxide layer in question (such as CeO_2) is thermodynamically stable. For example, during electron beam evaporation of Ce to form high-quality, epitaxial CeO_2 on Ni, careful control of the partial pressures of H_2, H_2O, and O_2 is essential. The partial pressure of O_2 is kept to

a minimum and the partial pressure of H_2O is monitored to provide sufficient oxidation of Ce to form stoichiometric CeO_2. NiO formation is not thermodynamically favorable under a wide range of H_2O partial pressures, whereas CeO_2 is thermodynamically stable. Similar thermodynamic considerations show that under typical conditions for epitaxial deposition of CeO_2 on Ni, formation of chromium oxide is also expected.

To minimize the deleterious effects of chromium oxide formation, an additional step was introduced. By first depositing an epitaxial layer of Ni on the Ni-Cr substrates, the surface for epitaxy of the first oxide layer is not exposed to the Ni-Cr surface. Hence, deposition of oxide layers can be done under the same conditions developed for deposition of Ni. Furthermore, after the oxide layer depositions, the initially deposited Ni layer is diffused into the substrate. Hence this Ni layer can be considered to be transient.

Figure 1.34 shows a Rutherford backscattering spectrum (RBS) of a fully buffered Ni-13at%Cr substrate. The first CeO_2 layer was deposited by electron beam evaporation; the top two layers were deposited by rf sputtering. The various peaks observed and the layer to which they correspond are indicated in the figure. All layers have a relatively sharp interface, implying negligible interdiffusion. Also shown in the figure is the RBS spectrum obtained from the substrate after an O_2 anneal at 500°C for 1 h. The 500°C anneal in flowing O_2 is a rather harsh anneal, but it is useful to see how the substrate would hold up under such conditions. As can be seen, the RBS is hardly affected by the anneal. YBCO films were then fabricated on the substrate by using the two-step ex situ BaF_2 method. Excellent epitaxy of the YBCO film was obtained with the out-of-plane texture showing a significant improvement in the FWHM. The YBCO film had a critical current density of 1.4 MA/cm^2 at 77 K, 0 T. Moreover, the field dependence of J_c was similar to that observed for typical YBCO on RABiTS™.

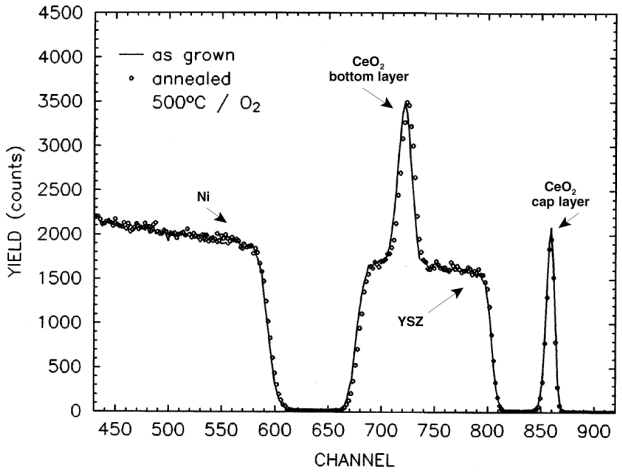

Fig. 1.34. Rutherford backscattering spectrum (RBS) of a CeO_2/YSZ/CeO_2/Ni-13at%Cr substrate. The solid line is for as-deposited RABiTS™ and the points are for the same substrate after no anneal in O_2 at 500°C for 1 h.

1.4.2 Fundamental Issues Affecting J_c of YBCO on RABiTS™

Fundamental issues affecting the critical current density of epitaxial high-temperature superconductors on RABiTS™ were examined. First, issues related to percolative pinch-off of the critical current density for long conductors due to a large grain size in the substrate and a finite width of the substrate are addressed. Second, texture stability and homogeneity in long-length substrates is discussed.

1.4.3 Effect of Large Grain Size of the Metal Substrate and the Finite Width of the Substrate

Limiting path calculations based on the technique proposed by Rhyner and Blatter[1] were performed. Instead of a square lattice, a more realistic hexagonal lattice of grains was assumed. Grain boundaries

were randomly assigned to be conducting or nonconducting, based on a total fraction, *f*, of conducting grain boundaries. The total fraction, *f*, is related to the macroscopic texture of the metal template based on a certain dependence of J_c on misorientation angle. For example, for a sample with a ϕ-scan FWHM, $\Delta\phi$, the expected grain boundary misorientation distribution (GBMD) is also guassian and has a FWHM of $\sqrt{2}\Delta\phi$. We further assume that grain boundaries with misorientations greater than 5° carry no current (i.e., they are nonconducting), and those with misorientations below 5° have J_c similar to the intragranular J_cs, and are conducting. Based on this dependence of J_c with misorientation angle and the FWHM of the GBMD, the fraction, *f*, of conducting grain boundaries can be deduced. The sample J_c is normalized so that $J_c = 1$ when all boundaries are conducting. Sample length and width are measured in units of grains. To eliminate end effects, periodic boundary conditions are applied in the direction of current flow.

To find J_c for a range of sample lengths, J_c was calculated for 20,000 samples, each 1,000 grains long. Thus the total length sampled is 2×10^7 grains. For a typical RABiTS™ sample, the average grain size is 50 μm, so the length sampled is ~1 km. Sample widths of 10, 20, 50, 100, and 200 grains were considered.

Figure 1.35 shows the calculated J_c for a 1-km-long RABiTS™ substrate with epitaxial HTS vs the width of the conductor as a function of the macroscopic texture. As indicated, reductions in J_c due to the finite width of the substrate become negligible for a width of the conductor greater than 100 grains. Typical RABiTS™ samples are 1 cm (or 200 grains) wide. Hence percolative pinch-off of J_c due to a large grain size in the substrate and a finite width of the substrate is not an issue for fabricating long-length, epitaxial HTS conductors based on the RABiTS™ technique. Another important finding can be inferred from Fig. 1.35. Typical long-length RABiTS™ samples have a texture corresponding to a FWHM of ~6 to 8° and more often are closer to 8° than 6°. Figure 1.35 indicates that the expected J_c is about ~0.3 (single-crystal J_c) for a typical FWHM of 8° for a 200-grains-wide conductor. The figure further indicates that if the texture of the substrates can be improved to obtain a FWHM of 6° or 5°, then a corresponding factor of 1.5 or 2 enhancement in J_c may be possible.

1.4.4 Texture Homogeneity in Long-Length Thermomechanically Processed Metal Substrates

Figure 1.36 shows a continuous measurement of the (200) and (111) peak intensities for a 20-m-long textured Ni substrate. The figure indicates that the (200) peak intensity is essentially constant along the 20-m length. The (111) peak intensity at all points is below the background, indicating a fully formed cube texture with no secondary textures or twins. Measurement of the in-plane and out-of-plane textures as a function of the length of the conductor show that the FWHM of the conductor is also constant along the length and shows relatively little fluctuation. Hence the expected GBMDs along the length of the tape are also expected to be constant. Because excellent texture homogeneity can be obtained in long lengths of Ni, texture inhomogeneity is not a limiting factor when long lengths of high-J_c epitaxial YBCO on RABiTS™ are fabricated.

1.4.5 Reference

1. J. Rhyner and G. Blatter, “Limiting-Path Model of the Critical Current in a Textured $YBa_2Cu_3O_{7-\delta}$ Film,” *Phys. Rev B* **40**(1), 829–32 (1989).

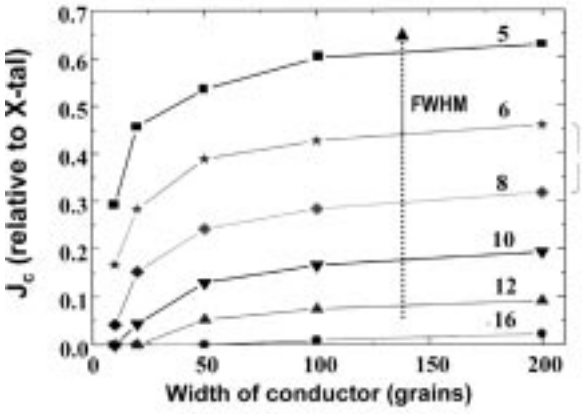

Fig. 1.35. Minimum J_c relative to that of single-crystal YBCO for 20,000 samples, each 1000 grains long (for a typical RABiTS™ Ni, the grain size is 50 μm, resulting in a sampling of ~1-km-long wire), as a function of the width of the conductor in units of grains. The different curves correspond to conductors with different FWHM of the macroscopic texture. The bracket corresponds to where typical RABiTS™ lies on this plot. Most long length Ni substrates fabricated so far have a FWHM of 8°.

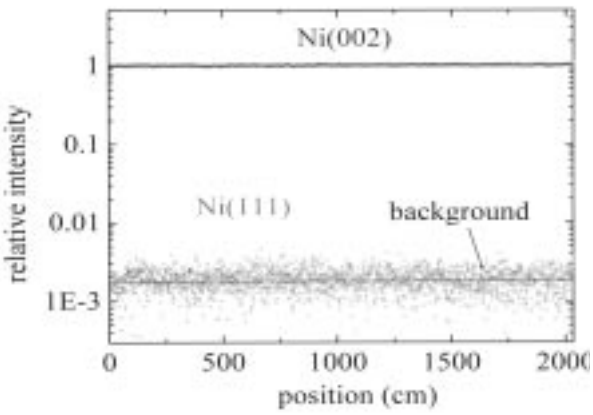

Fig. 1.36. (200) and (111) X-ray peak intensities measured continuously along the length of a 20-m-long cube-textured Ni substrate, 1 cm wide and 50 μm thick. The (200) peak intensity is essentially constant along the length. The (111) peak intensity at all points is below the average background intensity.

1.5 FABRICATION OF LONG LENGTHS OF EPITAXIAL BUFFER LAYERS ON BIAXIALLY TEXTURED-Ni SUBSTRATES USING A CONTINUOUS REEL-TO-REEL DIP-COATING UNIT

M. Paranthaman, T. G. Chirayil, F. A. List, X. Cui, A. Goyal, D. F. Lee, E. D. Specht, P. M. Martin, R. K. Williams, D. M. Kroeger, J. S. Morrell, D. B. Beach, R. Feenstra, and D. K. Christen

1.5.1 Introduction

Bulk solution techniques have emerged as potential low-cost nonvacuum processes for fabricating long lengths of YBCO coated conductors. Solution precursors can be used to grow both buffers and superconductors on roll-textured and annealed nickel. In this process, the substrates are coated with the metal-organic solution precursors at room temperature, followed by post-annealing at high temperatures to obtain highly crystalline phases. The control of precursor stoichiometry is straightforward. Buffer layers such as $REAlO_3$ (rare earth aluminate; RE = La, Nd) and $BaZrO_3$ were grown epitaxially from sol-gel alkoxide precursors on $SrTiO_3$ (100) single-crystal substrates. The $REAlO_3$ buffers grown on biaxially aligned Ni (100) substrates had a good out-of-plane texture but had two in-plane textures. However, we have recently used a spin-coating process to grow single cube-on-cube epitaxy of various RE_2O_3 (rare earth oxides; RE = Gd, Yb, and Eu) and $RE_2Zr_2O_7$ (rare earth zirconates; RE = La, Nd) directly on textured-Ni (100) substrates. To scale up this technique, we developed a dip-coating process. The dip-coating could be a batch or a continuous process. The advantage of the dip-coating process is its ability to

coat large surface areas, complex shapes, and double-sided tapes. Furthermore, material utilization is almost 100%. Although the dip-coating process has been used in various applications, to date no one has grown textured oxide buffers in lengths. It is also essential to grow dense and crack-free films. Solution-derived films crack with increasing thickness because of high-volume shrinkage as organics are removed during the heat-treatment process. As the process temperature increases, further shrinkage is caused by the amorphous-to-crystalline phase transformation and the thermal expansion mismatch between the substrate and the film. In such cases, restricting the film to a critical thickness prevents cracking. Thicker films are then achieved by multiple-coating and heat-treatment procedures. In the dip-coating process, the substrate is usually withdrawn vertically from the coating bath at a constant speed. The film thickness is directly proportional to the withdrawal velocity. The inner layer of the coating solution moves upward with the substrate while the outer layer returns to the bath. The viscosity and surface tension of the coating liquid and the force of gravity control the film thickness to certain extent. In this section we report the successful growth of epitaxial Eu_2O_3 and $La_2Zr_2O_7$ (LZO) buffer layers on textured-Ni (100) substrates in long lengths in a continuous reel-to-reel dip-coating unit.

1.5.2 Experimental Procedure

Biaxially textured Ni (100) and annealed substrates were obtained in the usual manner. After annealing, the Ni tapes were cleaned with a wet wipe soaked in isopropanol. A schematic diagram of the reel-to-reel continuous dip-coating unit is shown in Fig. 1.37. It is possible to anneal the as-rolled Ni tape in the presence of Ar/H_2 (4%) gas in a continuous mode in the reel-to-reel unit. Both ends of the annealed Ni tape were welded to Ni leaders mounted on two reels. The take-up reel was driven continuously by a stepper motor; the pay-out reel was tensioned by a variable-torque motor. The travel speed of the tape could be varied to 100 m/h. The integral reel-to-reel system, which is attached to a linear furnace, has the capability of processing up to several meters of buffered tape.

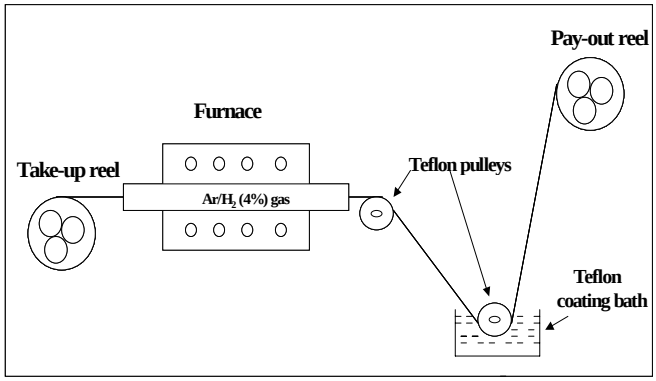

Fig. 1.37. Schematic diagram of the reel-to-reel continuous dip-coating unit.

A 2-methoxyethanol solution of europium methoxyethoxide or lanthanum zirconium methoxyethoxide was used for the dip-coating process. The details of the solution preparations were reported earlier.[1–4] The concentration of the coating solution was typically between 0.25 and 0.5 M. The Ni tapes from the pay-out reel were withdrawn from the coating bath at a constant speed of 1 to 10 m/h. The dip-coated tapes were coated on both sides and were post-annealed in a furnace, which had been preheated to 1000 and 1100°C. The flow rate of 1 atm Ar/H_2 (4%) gas was 2 to 4 L/min. The heat-treatment times typically varied from 10 min to an hour in the hot zone. After heat-treatment, the tapes were spooled on the take-up reel. The dip-coated buffers were then fully characterized by XRD, SEM, and electron back scattered Kikuchi diffraction (EBKD) patterns. On short samples of dip-coated Eu_2O_3 seeds, YSZ and CeO_2 layers were deposited by rf magnetron sputtering at 780°C and in 10 mTorr of Ar/H_2 (4%) gas. The plasma power was 75 W at 13.56 MHz. Ex situ YBCO precursors were deposited on CeO_2-buffered YSZ/Eu_2O_3 (dip-coated)/Ni substrates by electron-beam co-evaporation of Y, BaF_2, and Cu. Details of the experimental conditions were provided in the previous report.[2] The CeO_2-buffered YSZ/Eu_2O_3 (dip-coated)/Ni substrates were annealed under N_2 at 650°C for 1 h prior to the YBCO precursor deposition.

The films were analyzed by XRD. A Philips model XRG3100 diffractometer with Cu K_α radiation was used to record powder diffraction patterns. Alignment in short samples was measured by a Picker four-circle diffractometer with Cu K_α radiation, a 2-mm-diam incident beam, and a graphite diffracted-beam monochromator. The samples were oscillated 12 mm during data collection to obtain spatially averaged data. The out-of-plane alignment (omega scans) was measured by scanning the (100) planes of the film. The in-plane alignment (phi scans) was determined by measuring the (111) planes of the film. Pole figures were collected for all the layers to determine whether the film had a single-cube texture. For longer samples, alignment was measured as a function of position by repeatedly measuring rocking curves and phi scans while translating the sample. A larger Huber four-circle diffractometer was used to accommodate a translation stage. A Rigaku rotating-anode X-ray generator operating at 10 kW and equipped with an incident-beam monochromator provided a 1×1 mm^2 Cu K_α incident beam, and the sample was moved 5 mm between scans. Peak FWHMs were extracted by fitting least-squares to a Gaussian line shape. SEM micrographs were taken by a Hitachi S-4100 field emission SEM. The beam voltage was 10 kV. The thickness of the films was determined by RBS. EBKD patterns were obtained on lanthanum zirconium oxide (LZO) layers (the experimental details were published earlier). The resistivity and transport critical current density, J_c, was measured using a standard four-probe technique. Values of J_c were calculated using a 1-μV/cm criterion.

1.5.3 Results and Discussion

Typical θ-2θ scans for 60-nm-thick dip-coated Eu_2O_3 and LZO films on textured-Ni (100) substrates are shown in Fig. 1.38. The strong Eu_2O_3 (004) and LZO (004) signal from Fig. 1.38 (a) and (b) revealed the presence of a highly *c*-axis-aligned film.

Figure 1.39 shows ω and ϕ scans for the dip-coated Eu_2O_3 film. The tape was withdrawn at a rate of 1 m/h, and the film was heat-treated at 1070°C for an hour in a continuous mode. The FWHM values of Ni (002) and Eu_2O_3 (004) ω scans and Ni (111) and Eu_2O_3 (222) ϕ scans were determined at various positions along the 14-cm-long Ni tape. The texture of the film was uniform along the entire length of the tape. Similar results were also obtained on 1-m length of dip-coated Eu_2O_3 buffers. These results show that Eu_2O_3 can be grown epitaxially on {100}<001> Ni substrates in lengths. Producing low-cost nonvacuum buffer layers in long lengths is a major advancement in YBCO coated conductor technology. This process has now been reproduced at American Superconductor Corporation (ASC) to a continuous web coating through a slot die onto Ni substrates. ASC has successfully produced meter lengths of epitaxial

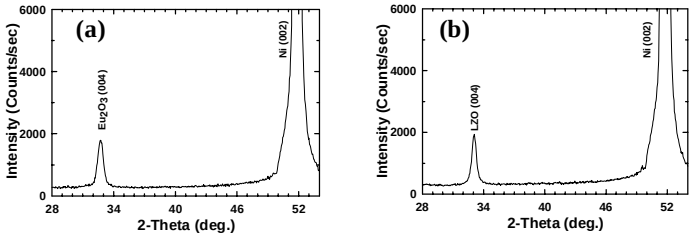

Fig. 1.38. Typical θ-2θ scans for a 60-nm-thick dip-coated Eu_2O_3 (a) and LZO (b) buffer layer on biaxially textured-Ni (100) substrate.

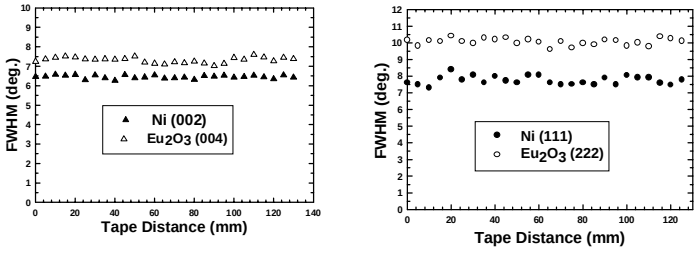

Fig. 1.39. The FWHM values of ω and ϕ scans of both Eu_2O_3 and Ni are plotted along the length of the dip-coated substrate.

Gd_2O_3 seed layers. As shown in Fig. 1.40, the XRD results from ω and ϕ scans on the dip-coated LZO film revealed good epitaxial texturing. The tape was withdrawn at a rate of 1 m/h, and the film was heat-treated at 1000°C. The FWHM values for Ni (002), and LZO (004) are 7.3° and 7.7°, and those of Ni (111), and LZO (222) are 8.7° and 8.7°, respectively. Typical Eu_2O_3 (222) and LZO (222) pole figures for 60-nm-thick dip-coated Eu_2O_3 and LZO films on textured-Ni substrates are shown in Fig. 1.41. The four-fold symmetry in (111) pole figures indicates the presence of a single-cube-textured buffer. The reel-to-reel dip-coating unit, was used to grow biaxially textured oxide buffers on textured-Ni substrates for the first time. Using similar conditions, one should be able to dip-coat other rare earth oxides and other rare earth zirconates and obtain good texture.

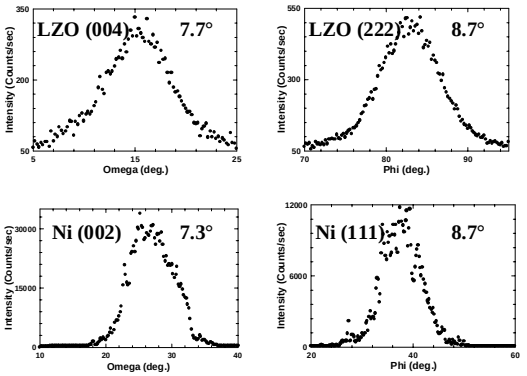

Fig. 1.40. The ω and ϕ scans for a 60-nm-thick dip-coated LZO buffer layer on biaxially textured-Ni (100) substrate. The FWHM values for each scan are shown inside the scans.

Typical RBS spectra for 60-nm-thick dip-coated Eu_2O_3 films with different annealing times at a temperature of 1170°C are shown in Fig. 1.42. The length of the hot zone in the present furnace is 10 cm. The residence time at the hot zone for 3 m/h speed is 2 min, and that for 0.3 m/h speed is 20 min. For spin-coated buffers, we typically anneal for an hour at the desired temperature in a static configuration with a constant flow of Ar/H_2 (4%) gas. As shown by the RBS spectra, the films annealed at 3 m/h had some carbon present, but films annealed at 0.3 m/h had no carbon. Similarly, we have also observed no carbon in spin-coated buffers. Hence for producing long buffers, it is necessary to increase the length of the hot zone in

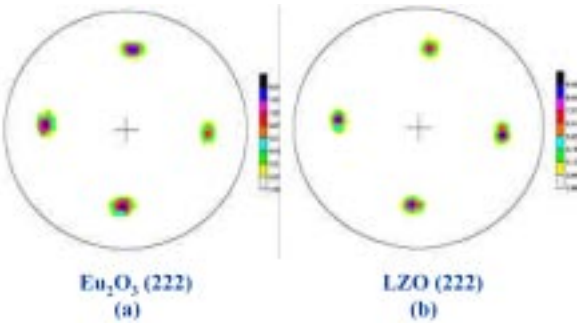

Fig. 1.41. (222) X-ray pole figures of dip-coated (a) Eu_2O_3 and (b) LZO buffer layers.

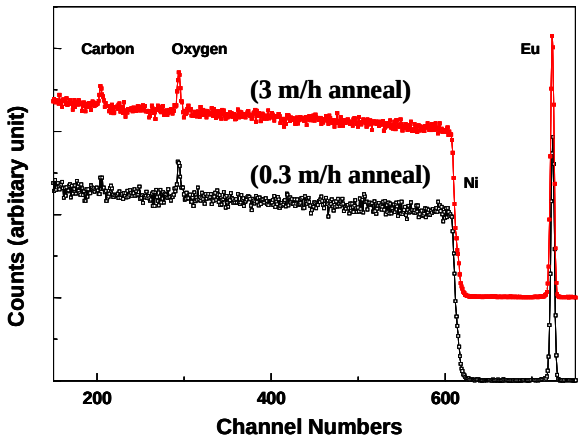

Fig. 1.42. Rutherford backscattering spectra of a 60-nm-thick dip-coated Eu_2O_3 buffer layer on biaxially textured-Ni (100) substrate with different annealing times. The spectra were measured with 5.0-MeV He^+ ions at near-normal incidence, detected at 160° scattering angle.

the furnace or to reduce the tape speed. Typical RBS spectra for 60-nm-thick dip-coated LZO buffers are shown in Fig. 1.43. The LZO films were annealed at a speed of 0.3 m/h at 1000°C, and there was no carbon present in the film. Simulation studies indicate the La:Zr stoichiometry to be 1:1. SEM micrographs for 60-nm-thick dip-coated Eu_2O_3 and LZO buffers are shown in Fig. 1.44. The dip-coated films are smooth, continuous, and crack-free. Efforts are being made to scale up the thickness and still maintain a good microstructure.

Orientation micrographs for 60-nm-thick LZO buffers are shown in Fig. 1.45. To visualize the percolative path in LZO film, all grains were color-coded with the criterion that a single color represents a percolative region of orientation changes less than 4° [Fig. 1.45 (a)], 6° [Fig. 1.45 (b)], and 8° [Fig. 1.45 (c)]. It can be seen that most of the film is percolatively connected within 8°.

Attempts to use PLD to grow YBCO films directly on the dip-coated Eu_2O_3 and LZO buffers resulted in YBCO films with poor properties. In addition, XRD showed large amounts of NiO. To be compatible with either the ex situ BaF_2 or trifluoroacetate (TFA) processes, a CeO_2 cap layer is required; YSZ also seems to be a good barrier layer. Hence, we used rf magnetron sputtering to grow both YSZ and CeO_2 layers on top of the dip-coated Eu_2O_3 seed layers. By using rf sputtering, we have always produced very dense buffer layers. High-quality YBCO films with a thickness of 300 nm were grown on CeO_2 (sputtered)/YSZ (sputtered)/Eu_2O_3 (dip-coated)/Ni substrates by using the ex situ BaF_2 process. XRD studies indicated the presence of a highly textured YBCO film. Also, the simulation of the RBS spectra for the same film indicated the film thickness for YBCO, CeO_2, YSZ, Eu_2O_3 are 300, 10, 295, and 60 nm, respectively. The T_c measured for this film was 90 K. The field dependence of J_c for the same film is shown in Fig. 1.46. The zero-field I_c measured was 16 A, which translates to a J_c of 1.1 MA/cm^2 at 77 K and self-field. The J_c at 0.5 T is 0.23 MA/cm^2. This indicates the presence of a strongly linked YBCO film. From these results, we can conclude that dip-coated Eu_2O_3 layers provide a good template for further growth of YBCO films. The performance of sol-gel dip-coated buffers approached that of the vacuum-deposited buffers. Efforts are being made to grow YBCO films on dip-coated LZO buffers with sputtered cap layers. Also, we recently reported the growth YBCO films with a J_c of 480,000 A/cm^2 at 77 K and self-field on spin-coated LZO-buffered Ni substrates with sputtered YSZ and CeO_2 top layers. For the production of long lengths of coated conductors, it is very clear that one can combine both nonvacuum and vacuum processes to deposit high-quality buffer layers. The next key step is to develop an all-solution precursor route to produce both buffers and YBCO superconductors.

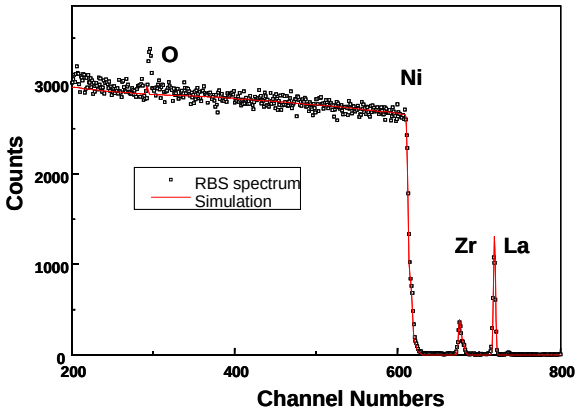

Fig. 1.43. Rutherford backscattering spectra of a 60-nm-thick dip-coated LZO buffer layer on biaxially textured-Ni (100) substrate.

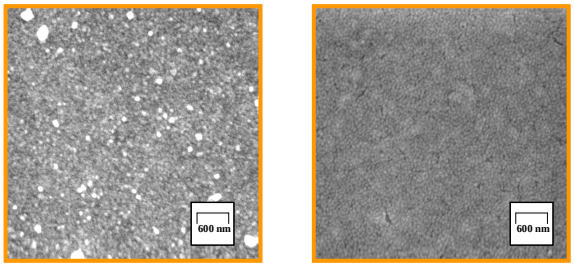

Fig. 1.44. SEM micrographs for a 60-nm-thick dip-coated Eu_2O_3 (a) and LZO (b) buffer layers on biaxially textured-Ni (100) substrates.

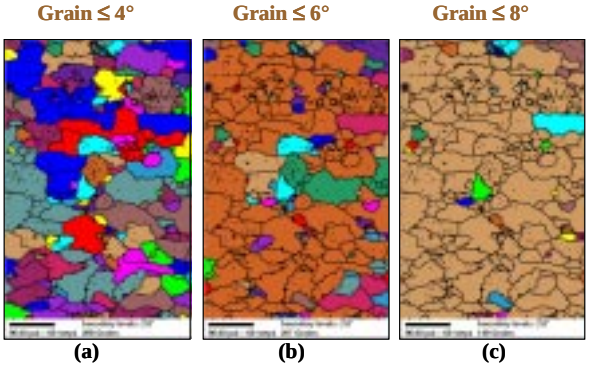

Fig. 1.45. Orientation image micrograph from a dip-coated LZO-buffered Ni substrate. BKD patterns were obtained in a hexagonal grid with a step of 0.9 μm. Variations in intensity are a reflection of pattern quality or intensity of the Kikuchi bands. Orientation image micrographs were colored with the criterion that a given color represents a percolative region within (a) 4°, (b) 6°, and (c) 8°. Clearly most of the substrate is well connected by boundaries less than 8°.

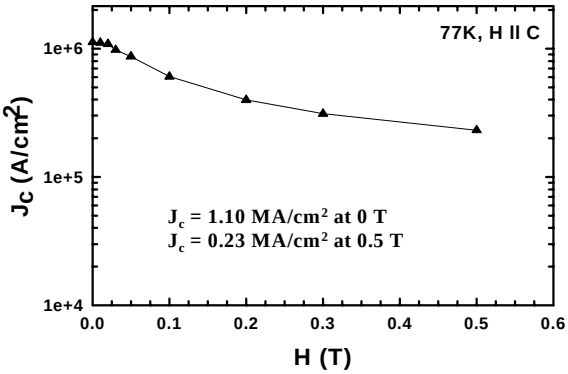

Fig. 1.46. The field dependence of critical current density, J_c, for 0.3-μm-thick YBCO film (ex situ BaF_2 process) on CeO_2 (sputtered)/YSZ(sputtered)/Eu_2O_3(dip-coated)/Ni substrates.

1.5.4 References

1. J. S. Morrell et al., "Epitaxial Growth of Gadolinium Oxide on Roll-Textured Nickel using a Solution Growth Technique," *J. Mater. Res.* **15**, 621–28 (2000).

2. T. G. Chirayil et al., "Epitaxial Growth of Yb_2O_3 Buffer Layers on Biaxially Textured-Ni (100) Substrates by Sol-Gel Process," *Mater. Res. Soc. Symp. Proc.*, **574**, 51–56 (1999).

3. M. Paranthaman et al., "Demonstration of High Current Density YBCO Coated Conductors on RE_2O_3-Buffered Ni Substrates with Two New Alternative Architectures," pp. 879–86 in *Advances in Cryogenic Engineering (Materials)*, vol. 46, ed. Balachandran et al., Kluwer Academic/Plenum Publishers (Proc. of CEC-ICMC Meeting, Montreal, Canada, July 1999), 2000.

4. T. G. Chirayil et al., "Epitaxial Growth of $La_2Zr_2O_7$ Thin Films on Rolled-Ni Substrates by Sol-Gel Process for High T_c Superconducting Tapes," *Physica C* **336**, 63–69 (2000).

1.6 FABRICATION OF LONG LENGTHS OF YBCO COATED CONDUCTORS USING A CONTINUOUS REEL-TO-REEL DIP-COATING UNIT

M. Paranthaman, T. G. Chirayil, S. Sathyamurthy, D. B. Beach, A. Goyal, F. A. List, D. F. Lee, X. Cui, S. W. Lu, B. Kang, E. D. Specht, P. M. Martin, D. M. Kroeger, R. Feenstra, C. Cantoni, and D. K. Christen (ORNL)

A low-cost, nonvacuum, solution precursor route has been developed to produce epitaxial Gd_2O_3 and Eu_2O_3 buffer layers and $YBa_2Cu_3O_{7-\delta}$ (YBCO) superconductors on biaxially textured metal substrates. On sol-gel Eu_2O_3 seed layers with sputtered YSZ and CeO_2 top layers, YBCO film with a J_c of more than 1 MA/cm^2 at 77 K was obtained. PLD was used to grow YBCO film with a J_c of 200,000 A/cm^2 at 77 K on all solution buffer layers (CeO_2/Eu_2O_3/Ni). Meter lengths of epitaxial and crack-free Gd_2O_3 buffer

layers were fabricated on cube-textured Ni-W (3 at. %) substrates for the first time. High-quality YBCO films were deposited on RABiTS™ by using a TFA precursor approach. The precursors were either spin-coated or dip-coated and decomposed in a newly developed, fast (3-h) burnout step followed by post-annealing. In a stationary burnout route, we have produced 40-cm-long crack-free YBCO TFA precursors on RABiTS™. On short segments, YBCO films with a J_c greater than 500,000 A/cm^2 at 77 K were grown on all PLD buffered-Ni substrates (CeO_2/YSZ/CeO_2/Ni).

For the promise of high-temperature superconductivity to be realized, practical processes are needed to manufacture useful lengths of HTS wires. The goal is to produce robust, economical, and scalable processes for making wire that can carry sufficient current at liquid nitrogen temperatures. The second-generation YBCO coated conductors are potential candidates. Also, YBCO coated conductors have good superconducting properties in significant magnetic fields at the liquid nitrogen temperatures. Three methods have been developed for producing long lengths of YBCO coated conductors.

The first method is ion-beam-assisted deposition (IBAD), which was developed by Iijima et al.[1] (Fujikura, Japan) and was later significantly improved at Los Alamos. In the IBAD technique, YSZ or MgO buffer templates with a biaxial cube texture were produced on polycrystalline nickel alloy substrates by using a well-collimated secondary gun directed toward the substrate at a certain angle to sputter off nonfavorable orientations during buffer layer deposition. This is followed by PLD to grow high-quality YBCO layers. The second method is the RABiTS™ process, developed at Oak Ridge. In this process the biaxial texture templates are produced in the starting nickel or nickel alloy substrates by mechanical deformation of metal rods over 95% followed by annealing. The buffer layers and YBCO superconductors were then grown epitaxially on biaxially textured nickel tapes or sheets. The third method, ISD,[2] was developed in Japan and further pursued in Europe and the United States. In this approach, the biaxially textured YSZ or MgO buffer-layer templates were produced by keeping the starting polycrystalline nickel alloy substrates at a certain angle with respect to the on-axis flux of the buffers. The YBCO layers were then deposited by PLD.

Chemical-solution epitaxy has emerged as a viable, nonvacuum process for fabricating epitaxial buffer layers and YBCO superconductors. The roll-textured nickel substrates are the ideal starting templates for this process. The major advantages of solution processes are as follows:

- The coating of metal-organic precursor solution is done at room temperature, followed by annealing at high temperatures to obtain highly crystalline phases.
- The control of precursor stoichiometry or doping is both easy and precise.
- It is completely a nonvacuum, high-volume deposition process.
- The material utilization is almost 100%, and the substrates can be coated on both sides.

To scale up the solution process, we developed a reel-to-reel dip-coating process. The dip-coated precursors could be post-annealed in a batch or in a continuous process. We have recently developed an all-alkoxide route to produce epitaxial oxide buffer layers on roll-textured nickel substrates. In this section we report our successful demonstration of the growth of epitaxial Gd_2O_3 seed layers on biaxially textured substrates with reduced magnetism in meter lengths. In addition, we will also report our recently developed fast burnout step for YBCO TFA precursors.

1.6.1 Preparation of Ni or Ni-Alloy Tapes

Both Ni substrates and Ni-W (3 at. %) (stronger substrates and substrates with reduced magnetism) were chosen for this study. Biaxially textured Ni (100) or Ni-W (3 at. %) substrates were obtained by mechanically deforming the metal rods over 95% followed by annealing at 1000 to 1200°C for 1 h in the

presence of Ar/H_2 (4%) gas. Meter lengths of 50-m-thick and 1-cm-wide as-rolled metal substrates were cleaned by sonification in isopropanol in a reel-to-reel substrate-cleaning unit. The cleaned substrates were then annealed in Ar/H_2 (4%) to get the required cube texture in a reel-to-reel annealing furnace at the optimum temperatures and time.

1.6.2 Coating and Heat-Treatment

A 2-methoxyethanol solution of europium methoxyethoxide/acetate or gadolinium methoxyethoxide/acetate precursors was used for the spin-coating/dip-coating processing of buffer layers. The solution preparations were reported earlier. The typical concentrations of the solutions were 0.25 to 0.5 M. In the reel-to-reel dip-coating unit, both ends of the annealed Ni or Ni alloy tapes were electrically spot-welded to Ni leaders mounted on two reels. The take-up reel was driven continuously by a stepper motor, and the pay-out reel was tensioned by a variable-torque motor. The textured tapes from the pay-out reel were withdrawn from the coating bath at a constant speed of 3 to 30 m/h. The tapes were coated on both sides. The coated tapes were then annealed in a preheated furnace. The furnace was kept at 1050 to 1150°C with the constant purging of Ar/H_2 (4%) gas. The tapes were annealed for a residence time of 30 to 60 min. For all solution buffers, cerium methoxyethoxide precursors were used for the CeO_2 cap layer.

For the YBCO growth, Y, Ba, and Cu TFA precursor solutions were prepared. The concentration of the solution was typically 2 M total cations. The YBCO precursor solutions were spin-coated at 2000 rpm for 120 s or dip-coated at a constant speed of 20 to 30 m/h. The coated tapes were heat-treated in two stages. The first stage is the burnout step. It is very important to obtain crack-free, featureless brown precursors at this stage. This step takes nearly 10 h, as reported in the literature. We have developed a fast (3-h) burnout step to obtain crack-free YBCO precursors. The heat-treatment step for the first burnout step is shown in Fig. 1.47. The first burnout stage resulted in amorphous Y_2O_3, Cu_2O/CuO and crystalline BaF_2 phases. The second stage is the post-annealing process during which the YBCO precursors are annealed in a controlled-atmosphere furnace equipped with wet/O_2/Ar mixtures. The YBCO conversion is typically carried out at 735°C with an oxygen partial pressure [$P(O_2)$] of 150 to 180 ppm and an H_2O dew point of 40°C. Linear gas-flow conditions were used. The process time varied from 1 to 3 h, depending on film thickness and substrate width.

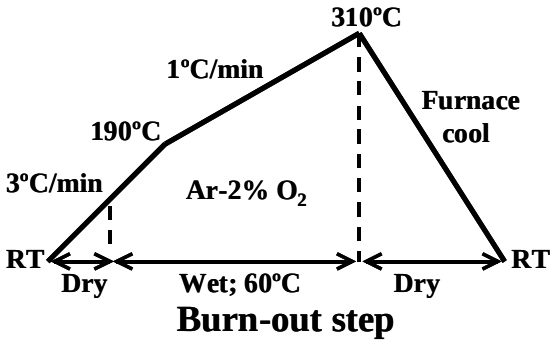

Fig. 1.47. The heat-treatment step for the first burnout step of YBCO TFA precursors.

1.6.3 Characterization

The buffer layers and YBCO superconductors were characterized by XRD, SEM, and EBKD. The thickness of both buffers and YBCO films were determined by both RBS and alpha step profilometer scans. The carbon concentrations in solution buffers have been determined by proton resonance (E_H = 1.73 MeV) from RBS. The resistivity and transport critical current density (J_c) was measured by using a standard four-probe technique. Ag contacts were made by sputtering. After Ag contacts were made, YBCO films were annealed in O_2 at 500°C for 30 min, slowly cooled to 350°C, and further furnace-cooled to room temperature in pure O_2. The voltage contact spacing was 0.4 cm. Calculation of J_c values was based on a 1-μV/cm criterion.

1.6.4 Preparation of YBCO Test Structures

On short samples of dip-coated Eu_2O_3, YSZ and CeO_2 top layers were deposited by rf magnetron sputtering at 780°C in 10 mTorr of Ar/H_2 (4%) gas. The plasma power was 75 W at 13.56 MHz. Ex situ YBCO BaF_2 precursors were deposited on CeO_2-buffered YSZ (sputtered)/Eu_2O_3 (dip-coated)/Ni substrates by electron beam co-evaporation of Y, BaF_2, and Cu. Details of the experimental conditions were reported earlier. The CeO_2-buffered YSZ (sputtered)/Eu_2O_3 (dip-coated)/Ni substrates were annealed under N_2 at 650°C for 1 h prior to the YBCO precursor deposition. The YBCO films on all solution buffers (CeO_2 (one coat)/Eu_2O_3 (four coats)/Ni) were grown by PLD at 780°C and P(O_2) of 185 mTorr.

1.6.4.1 Eu_2O_3 Buffer Layers

XRD results indicated the presence of epitaxial, crack-free 50-nm-thick Eu_2O_3 buffer layers on {100}<001> Ni substrates. Longer annealing times during processing eliminated the presence of carbon in the dip-coated buffers. (To reproducibly grow YSZ epitaxially on sol-gel seed layers, the carbon has to be removed completely from the solution layers.) On Eu_2O_3 seed layers with sputtered YSZ and CeO_2 top layers, YBCO film with a J_c of more than 1 MA/cm² was obtained. The field dependence of J_c for the same film is shown in Fig. 1.48. The J_c at 0.5 T is 0.23 MA/cm². This proves that Eu_2O_3 seed layers provide a good template to fabricate high-current-density YBCO films. On all solution buffer layers (CeO_2; one coat/Eu_2O_3, four coats), YBCO film with a J_c of 200,000 A/cm² was obtained. The field dependence of J_c for the same film is shown in Fig. 1.49. The total buffer layer thickness is 220 nm. The YBCO films on all solution buffer layers had porous microstructures. In addition, NiO impurities were also present. To further improve the current density, it is necessary to grow dense and thicker buffers.

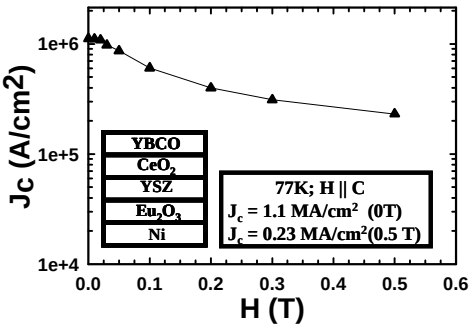

Fig. 1.48. The field dependence of critical current density, J_c, for 300-nm-thick YBCO film (ex situ BaF_2 process) on CeO_2(sputtered) (10 nm)/YSZ(sputtered)(295 nm)/ Eu_2O_3(dip-coated)(60 nm)/Ni substrates.

1.6.4.2 Gd_2O_3 Buffer Layers on Ni-W (3 at. %) Substrates

The annealed Ni-W (3 at. %) substrates are much stronger than pure Ni substrates and have reduced magnetism. The yield strength (YS) at 0.2 % is 150 to 200 MPa. This is comparable to 164 MPa YS for Ni-Cr (13 at. %) substrates. Detailed XRD studies indicate that Gd_2O_3 layers can be grown directly on Ni-W (3 at. %) substrates without any surface modifications. The FWHM values for Ni (002) and Gd_2O_3 (004) are 5.0°, and 8.9°, and those of Ni (111) and Gd_2O_3 (222) are 7.3° and 9.0°, respectively. The four-fold symmetry in the Gd_2O_3 (222) pole figure indicated the presence of a single-cube textured

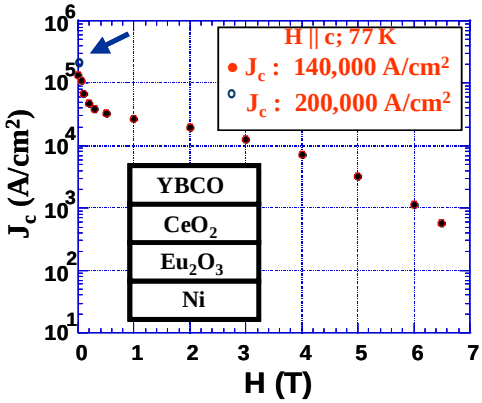

Fig. 1.49. The field dependence of critical current density, J_c, for 200-nm-thick PLD-grown YBCO film on CeO_2(solution)(20 nm)/Eu_2O_3 (solution)(200 nm)/Ni substrates.

buffer. Efforts are being made to grow superconductors on these layers. On all vacuum-buffered-Ni-W (3 at. %) substrates [YBCO/CeO_2/YSZ/Y_2O_3/Ni-W (3 at. %)], YBCO films with a J_c of 1.9 MA/cm^2 at 77 K were obtained. Meter lengths of Gd_2O_3 seed layers on roll-textured Ni-W (3 at. %) substrates were produced. The texture along the 1-m tape is shown in Fig. 1.50. The texture is uniform on most of the lengths. The SEM picture in Fig. 1.51 indicates the presence of a continuous, crack-free Gd_2O_3 buffer layer.

1.6.4.3 YBCO TFA Precursors

In a stationary burnout step, 40-cm-long, crack-free YBCO TFA precursors on RABiTS™ were produced. In a reel-to-reel continuous burnout step, 10-cm-long crack-free YBCO precursors on RABiTS™ were produced. On short samples, YBCO films on $LaAlO_3$ (100) single-crystal substrates had a J_c greater than 2 MA/cm^2 at 77 K. However, YBCO films on PLD RABiTS™ had a J_c of 500,000 A/cm^2 at 77 K. These results were obtained by means of a fast burnout precursor step. The film thickness is 0.3 μm. The field-dependence J_cs for these films are shown in Fig. 1.52. In the burnout step, the heat-treatment of YBCO precursors is rate-limiting because of the high volatility of the Cu TFA precursors. To carry out a much faster burnout step, other Cu-containing precursor chemistry has to be developed.

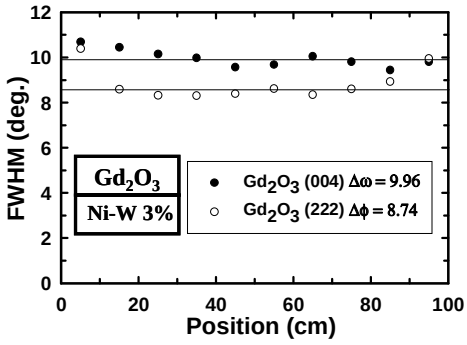

Fig. 1.50. The FWHM values of ω and ϕ scans for sol-gel Gd_2O_3 seed layers deposited on textured Ni-W 3% substrates are plotted along the length of the dip-coated substrate.

To conclude, the performance of sol-gel templates is approaching that of vacuum templates. On Eu_2O_3 seed layers with YSZ and CeO_2 sputtered top layers, YBCO film with a J_c of 1.1 MA/cm^2 at 77 K was obtained. On all solution buffer layers, YBCO film with a J_c of 200,000 A/cm^2 at 77 K was obtained. Meter lengths of epitaxial Gd_2O_3 buffer layers were fabricated on roll-textured Ni-W (3 at. %) substrates. A faster burnout step was developed for YBCO TFA precursors. YBCO films with a J_c of greater than 2 MA/cm^2 on $LaAlO_3$ substrates and greater than 500,000 A/cm^2 were obtained on PLD-grown RABiTS™.

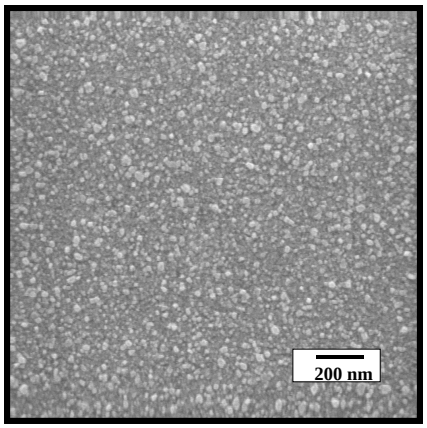

Fig. 1.51. SEM micrograph for a 20-nm-thick dip-coated Gd_2O_3 seed layer on biaxially textured Ni-W 3% (100) substrates.

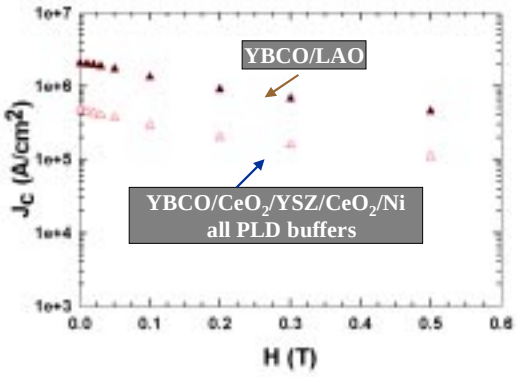

Fig. 1.52. The field dependence of critical current density, J_c, at 77 K and self-field for 0.3-μm-thick YBCO film on both $LaAlO_3$ (100) single crystals and all PLD-buffered CeO_2/YSZ/CeO_2/Ni substrates.

1.6.5 References

1. Y. Iijima et al., "In-Plane Aligned $YBa_2Cu_3O_{7-x}$ Thin Films Deposited on Polycrystalline Metallic Substrates," *Appl. Phys. Lett.* **61**, 2231–33 (1992).

2. K. Hasegawa et al., "In-Plane Aligned YBCO Thin Film Tape Fabricated by Pulsed Laser Deposition," pp. 745–48 in *Advances in Superconductivity IX*, Proc. of the 9th Intl. Symp. On Superconductivity (ISS '96), ed. S. Nakajima, and M. Murakami, Sapporo, Japan 1996.

1.7 LOW-COST Y-Ba-Cu-O_x COATED CONDUCTORS

M. W. Rupich, Q. Li, S. Annavarapu, C. Thieme, W. Zhang, and V. Prunier (ASC), M. Paranthaman, A. Goyal, D. F. Lee, E. D. Specht, and F. A. List (ORNL)

Solution-based techniques have been examined as potential low-cost processes for manufacturing YBCO coated conductors. YBCO films prepared from metal TFA precursors have achieved performance levels equaling or exceeding that of vapor-deposited films with the same thickness on CeO_2/YSZ(Xtal) substrates. Critical current densities of 4.5 MA/cm^2 and 2 MA/cm^2 have been achieved in 0.4-μm-thick YBCO films on CeO_2/YSZ(Xtal) and CeO_2/YSZ/CeO_2/Ni substrates, respectively. Textured Gd_2O_3 buffer layers have been deposited on deformation-textured Ni substrates in a reel-to-reel process. The performance of YBCO films deposited on substrates containing the Gd_2O_3 seed layers is comparable in performance to YBCO films grown on all-vacuum-deposited buffer layers.

American Superconductor Corporation (ASC) and ORNL have collaborated to develop low-cost solution-based routes for deposition of both the superconducting YBCO layer and the oxide buffer layers. Although solution-based processes have been developed for many applications, it is uncertain whether such low-cost processes can be developed for deposition of oxide layers over continuous lengths of metal substrates with the quality and uniformity required for HTS conductors. Our approach to answering this question is to characterize the solution-deposited oxide-buffer and YBCO layers and to benchmark their performance against that of similar films prepared by conventional vapor deposition techniques. In this report, we review the current status of solution-based processes for the deposition of YBCO films and oxide buffer layers and compare their performance with those of films deposited by conventional vacuum-based deposition techniques.

1.7.1 YBCO Deposition

The YBCO precursors were prepared as a stoichiometric solution of yttrium, barium, and copper TFAs by using techniques similar to those described by McIntyre.[1] The development of a solution-based deposition process for YBCO films was carried out on model substrates consisting of CeO_2/YSZ(Xtal). The CeO_2 layers, typically 20-nm thick, were deposited by rf magnetron sputtering. The YBCO precursor solutions were deposited by standard spin-coating techniques. Deposition of YBCO films on oxide-buffered metal substrates was performed with the same precursor solution by either spin coating (short samples) or web coating (long-length samples). Processing of the YBCO films (0.4 μm) consists of two steps. The first is the decomposition of the precursor to a homogeneous film of CuO, Y_2O_3, and BaF_2, which occurs between 150 and 400°C. The decomposition was carried out in either a continuous reel-to-reel oven or a static oven, depending on the sample length. The second step is the formation of the YBCO phase, which is carried out in an $O_2/H_2O/N_2$ atmosphere at 700 to 850°C. Formation of the YBCO phase was carried out in a static furnace configuration.

1.7.2 Buffer Layer Deposition

A gadolinium alkoxide precursor was used to deposit Gd_2O_3 buffer seed layers on deformation-textured Ni substrates. A laboratory web-coater was used to deposit precursor solutions on continuous lengths of Ni (up to 10 m long). The precursor films were converted to the Gd_2O_3 phase under an H_2/Ar atmosphere at 900 to 1200°C in a continuous reel-to-reel process furnace. Y_2O_3 and CeO_2 seed layers were deposited by e-beam deposition techniques developed at ORNL. The YSZ barrier and CeO_2 cap layers were deposited by magnetron sputtering at either ASC or ORNL by techniques described previously. The depositions were carried out on both static and reel-to-reel equipment.

1.7.3 Measurements

Current densities were determined by transport measurements at 77 K in self-field with a criterion of 1 μV/cm. Measurements on metal substrates were made over the full width of the substrate, typically 5 to 10 mm. Measurements on single-crystal substrates were made on ~1-mm-wide bridges. Reel-to-reel XRD characterizations were carried out on a system developed at ORNL. The oxide film thickness was determined by means of a Zygo interferometer or RBS.

1.7.4 Growth of YBCO Films on Oxide-Buffered Metal Substrates

RABiTS™-type substrates were used to test the compatibility of the solution-based YBCO deposition process with the metal substrates required for the YBCO coated conductors. The substrates consisted of CeO_2/YSZ/CeO_2/Ni obtained from ORNL or CeO_2/YSZ/Y_2O_3/Ni substrates prepared at ASC. No statistical difference was found between substrates with CeO_2 or Y_2O_3 seed layers. The YBCO precursor solutions were deposited on short-length samples (<1 cm) by spin-coating techniques and were processed under the conditions established for the model substrates. XRD analysis of the films showed only the (00*l*) reflections, indicating orientation of the YBCO *c*-axis perpendicular to the substrate surface. The films show a sharp superconducting transition, with transport J_cs up to 2.0 MA/cm^2 (77 K, self-field) obtained in 0.4-μm-thick films, as shown in Fig. 1.53. The variability of the YBCO films grown on the RABiTS™-type substrates is significantly larger than that observed on the single-crystal substrates and reflects primarily variability in the quality of the oxide-buffered substrates.

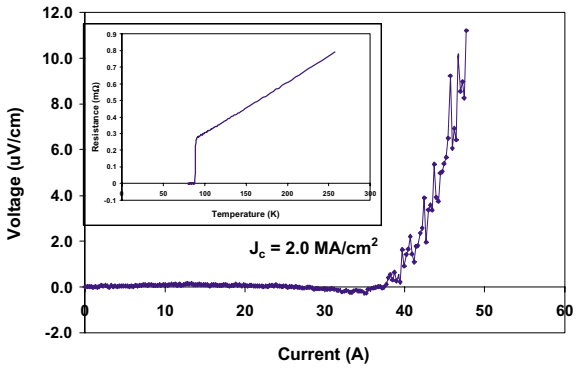

Fig. 1.53. I-V curve (77 K, self-field) for a 0.4-μm-thick YBCO film deposited by a solution-based process on a CeO_2/YSZ/Y_2O_3/Ni substrate. Insert shows the superconducting transition.

1.7.5 Deposition of Gd_2O_3 Buffer Layers on Ni Substrates

The solution deposition of oxide buffer layers has been demonstrated on short-length Ni substrates by Morrell et al.[2] However, extending this technique to the manufacture of YBCO coated conductors requires uniform texture, complete coverage, and uniform thickness over the entire length and width of the metal tape substrate. The Gd_2O_3 layers were deposited by a conventional web coater on continuous

lengths of 1-cm-wide deformation-textured Ni tape. The XRD (θ-2θ) pattern of a 50-nm-thick Gd_2O_3 film showed only the (00*l*) reflections, indicating the *c*-axis orientation of the Gd_2O_3 perpendicular with the Ni substrate.

Continuous XRD measurements, made on a reel-to-reel XRD system, confirm the uniformity of both the in-plane and out-of-plane texture over a 7-m length of Gd_2O_3/Ni tape as shown in Fig. 1.54. Measurements of the thickness of Gd_2O_3 films, with a nominal thickness of 50 nm, show a variation of ±10% over the length of the tapes. Minimal variation is observed across the tape width. These characterizations demonstrate the uniformity of the solution-deposited Gd_2O_3 layers on long-length Ni substrates. However, to be useful for the YBCO coated conductor system, they must support the growth of additional buffer layers. To test the quality of the Gd_2O_3 seed layers, YSZ barrier layers (200–400 nm) and CeO_2 cap layers (~20 nm) were deposited on Gd_2O_3/Ni tapes by magnetron sputtering. The YSZ and CeO_2 depositions were done with both static and reel-to-reel systems. From the XRD spectrum (θ-2θ) of the full buffer stack, sharp (00*l*) reflections are observed with only a small peak associated with (111) texture, indicating the quality of the buffer layers. Fig. 1.55 shows the in-plane and out-of-plane texture measured along the length of the 1-m tape by a reel-to-reel X-ray technique. Both the in-plane and out-of-plane textures of all three buffer layers are uniform along the length and are comparable to that of short-length samples prepared in static deposition systems.

1.7.6 Deposition of YBCO Films on CeO_2/YSZ/Gd_2O_3/Ni Substrates

The final qualification of the solution-deposited Gd_2O_3 buffer layers is the overall compatibility with the YBCO coatings. Figure 1.56 shows the performance of a solution-deposited YBCO film on a CeO_2/YSZ/Gd_2O_3/Ni substrate. For comparison, the performance of a comparable YBCO film deposited on a CeO_2/YSZ/Y_2O_3/Ni substrate, with all buffer layers deposited by vacuum-deposition techniques, is also included in Fig. 1.56. The

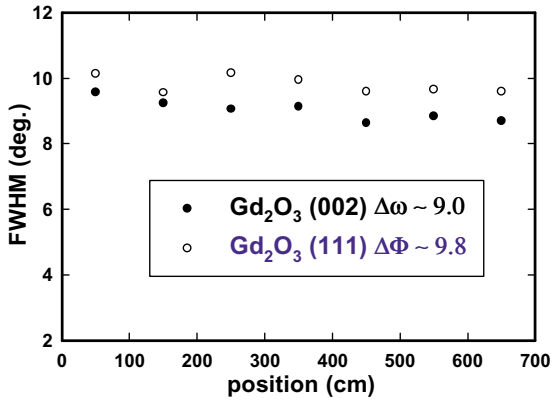

Fig. 1.54. Texture measurements obtained on a Gd_2O_3 buffer layer deposited by a solution process on a 7-m length of deformation-textured Ni tape.

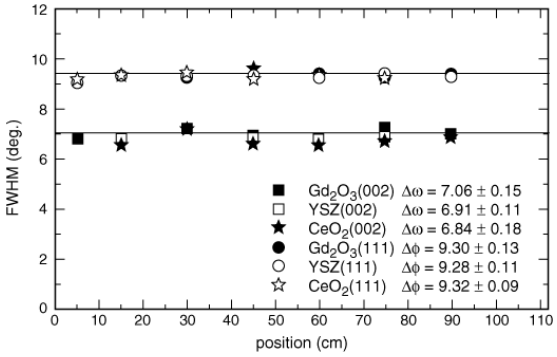

Fig. 1.55. Reel-to-reel X-ray diffraction scans showing the in-plane and out-of-plane texture of the oxide layers in the oxide buffer stack with the architecture CeO_2/YSZ/Gd_2O_3/Ni.

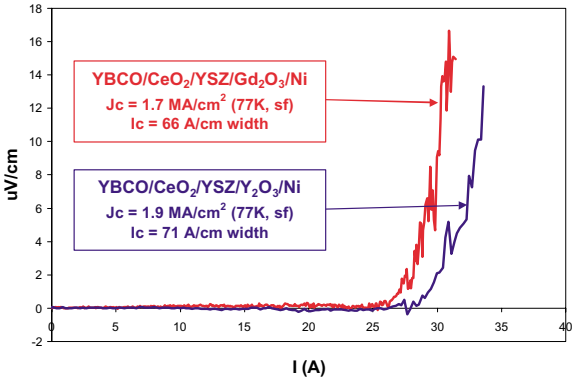

Fig. 1.56. I-V curves for 0.4-μm YBCO films deposited on CeO_2/YSZ/Gd_2O_3/Ni and CeO_2/YSZ/CeO_2/Ni substrates.

performance of these two YBCO films is nearly identical, demonstrating the compatibility of solution-based deposition processes for the YBCO coated conductor.

In summary, progress toward demonstration and development of key technologies necessary for the development of robust, high-rate, low-cost deposition technologies for the YBCO coated conductors has been reported. The successful development of these low-cost technologies into robust manufacturing processes will be required for the YBCO HTS conductors to be economically competitive with the current Bi-2223 conductors in the broad commercial HTS market.

1.7.7 References

1. P. C. McIntyre et al., "Effect of Growth-Conditions on the Properties and Morphology of Chemical Derived Epitaxial Thin Films of $Ba_2YCu_3O_{7-x}$ on (001) $LaAlO_3$," *J. Appl. Phys*. **71**, 1868–77 (1992).

2. J. S. Morrel et al., "Epitaxial Growth of Gadolinium Oxide on Roll-Textured Nickel using a Solution Growth Technique," *J. Mater. Res.* **15**, 621–28 (2000).

1.8 EPITAXIAL GROWTH OF A CONDUCTING BUFFER LAYER, $SrRuO_3$, ON SINGLE-CRYSTAL SUBSTRATES BY SOLUTION APPROACH FOR YBCO COATED CONDUCTORS

T. G. Chirayil, M. Paranthaman, C. Cantoni, D. K. Christen, and E. D. Specht (Oak Ridge National Laboratory), Chau-Yun Yang and S. E. Babcock (University of Wisconsin)

The RABiTS™ process is one of the leading techniques to develop high-current, second-generation superconducting tapes for high-field applications. High-J_c YBCO films have been grown by the RABiTS™ process by both vacuum deposition and a solution approach. Currently, we are exploring alternative buffer layers that are compatible with the BaF_2 or TFA process to deposit YBCO films. The feasibility of growing epitaxial conductive buffer layers is explored because they can provide an electrical contact between the superconducting film and the metal substrate. Conductive buffer layers can possibly aid in the current transport at the defective regions of the superconducting films.

The growth of epitaxial buffer layers by solution process was demonstrated by Shoup et al. with $LaAlO_3$ on a strontium titanate (STO) single crystal.[1] However, the LAO buffer layer on a textured-Ni substrate resulted in multiple orientations. Since then we have successfully developed the epitaxial growth of RE_2O_3 and $RE_2Zr_2O_7$ buffer layers on textured-Ni substrates with a single-cube texture. After completing the RABiTS™ architecture with sputtered YSZ and CeO_2 layers on the solution seed layers, we grew a YBCO film with a J_c value of 1.1 MA/cm^2 by PLD. The growth of high-J_c YBCO films on conductive buffer layers was demonstrated by Aytug et al.[2] by physical vapor deposition on both single crystal substrates and textured-Ni substrates. The architecture consisted of sputtered/laser ablated $SrRuO_3$ (SRO) and sputtered $LaNiO_3$ (LNO) buffer layers on LAO or STO single-crystal substrates or textured Ni substrates followed by PLD of YBCO.

Here, we report the epitaxial growth of SRO conductive buffer layers on LAO and STO single-crystal substrates by a solution process. A high-J_c YBCO film was grown on the solution SRO seed layers by PLD.

Ruthenium (III) 2,4-pentanedionate (Alfa), strontium metal, and 2-methoxy ethanol (Alfa, spectrophotometric grade) were used as received. The solution preparation was carried out under an argon gas atmosphere in a Schlenck-type apparatus. About 0.75 g of ruthenium (III) 2,4-pentanedionate and 0.164 g of strontium metal were dissolved in 50 ml of 2-methoxyethanol in separate 250-mL round-

bottom flasks and refluxed for 2 h. The two precursor solutions were mixed and refluxed for an additional hour before adjusting the concentration to 0.25 M in 2-methoxyethanol. The $SrRuO_3$ precursor solution was spin-coated onto STO or lanthanum aluminate (LAO) single-crystal substrates. The single-crystal substrates were cleaned ultrasonically in acetone for 1 h and were subsequently annealed at 900°C for 1 h under an oxygen atmosphere prior to coatings. The spin-coatings were applied with a spin-coater operated at 2000 rpm for 40 s. The samples were introduced into a furnace preheated to 900°C and were heat-treated for 1 h in flowing oxygen.

XRD of the film was done with a Philips Model XRG3100 diffractometer with Cu K_α radiation. A Picker four-circle diffractometer was used to collect pole figures and omega and phi scans. The thickness of the SRO buffer layer was determined by RBS. The SEM and cross-sectional TEM images were conducted at University of Wisconsin-Madison. The conductivity measurements were carried out with four-probe techniques.

The XRD of SRO film on LAO single-crystal substrate is shown in Fig. 1.57. The θ-2θ scan indicated two strong peaks at 22.8° and 46.6° from the SRO (100) and (200) reflections, respectively. However, the pole figure of the film showed two orientations on the LAO substrate. The orientations were determined as $(110)_{SRO}|(110)_{LAO}$ and $(553)_{SRO}|(001)_{LAO}$. However, the SRO (110) pole figure indicated that the SRO film on STO had a single-cube texture. The lattice parameters on SRO and STO are similar; therefore, the peaks could not be differentiated in the θ-2θ scan. The observation of two in-plane orientations of SRO on LAO may be due to the substrate miscut. Figure 1.58 is a secondary electron SEM image of the surface of the sol-gel–deposited SRO film. The edges of the rectangular islands are parallel to the <110> directions of the SRO pseudo-cubic unit cell.

Figure 1.59 is a diffraction contrast TEM image from a cross-sectional TEM sample. It shows three features of the microstructure: the block structure, the magnitude of the surface roughness, and the continuity of the film. Blocks of approximately rectangular cross section (in the TEM cross-sectional sample) with in-plane widths on the order of 100 nm are clear in the diffraction contrast image. They most likely produce the squared-off surface roughness seen in the SEM image. The cross-sectional transmission electron microscopy (TEM) images show that the block thickness varies by up to a factor of two, causing the local thickness to vary between 50 and 100 nm with an average of about 75 nm. The TEM cross sections also indicate that the SRO film fully covers the STO substrate and that there are no gaps between any of the blocks. The YBCO film

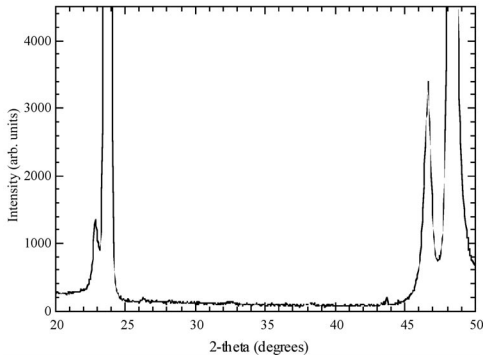

Fig. 1.57. X-ray diffraction of a sol-gel SRO film on an LAO single-crystal substrate.

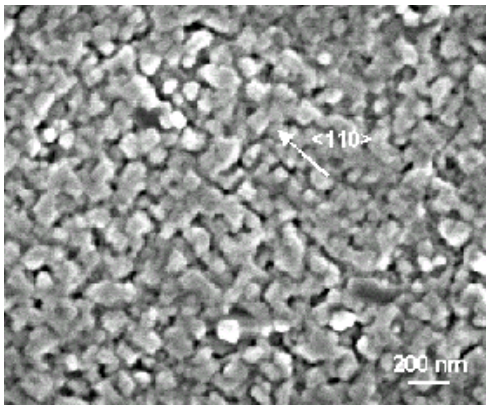

Fig. 1.58. SEM image of the surface of the sol-gel-deposited SRO film.

Fig. 1.59. TEM image from a cross-sectional TEM sample of sol-gel SRO on STO.

was deposited on the solution-based SRO buffer layer by PLD. The X-ray pattern of the sample is shown in Fig. 1.60. A *c*-axis-aligned YBCO films was obtained. The field-dependence J_c for the film is shown in Fig. 1.61. The extrapolated zero-field J_c is greater than 1 MA/cm^2 at 77 K. These results demonstrate that YBCO films with good superconducting properties can be obtained on solution SRO seed layers. Efforts are being made to grow solution SRO layers on textured-Ni substrates.

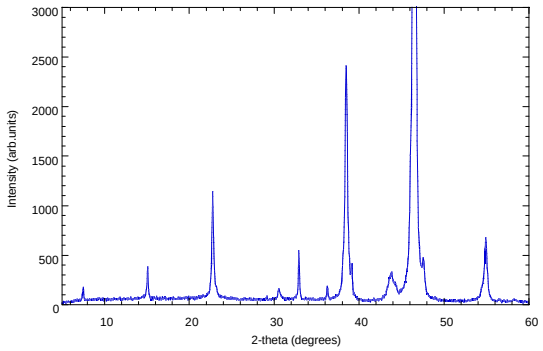

Fig. 1.60. X-ray pattern of sample YBCO film deposited on the solution-based SRO buffer layer by pulsed laser deposition.

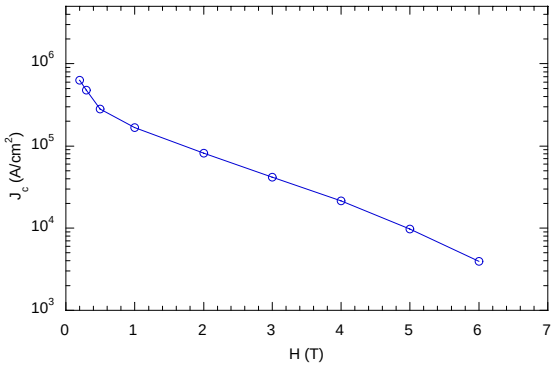

Fig. 1.61. Field-dependence J_c for YBCO film on a sol-gel buffered STO substrate.

To conclude, a solution approach was used to epitaxially grow a conducting SRO buffer layer on STO and LAO single-crystal substrates. A single-cube texture was obtained on both STO and LAO single-crystal substrates. The SEM image showed dense island-type SRO grains. No pinholes were found with cross-sectional TEM and SEM images. The YBCO film deposited by PLD had a J_c of greater than 1 MA/cm^2.

1.8.1 References

1. T. Aytug et al., "Growth and Superconducting Properties of $YBa_2Cu_3O_{7-x}$ Films on Conductive $SrRuO_3$ and $LaNiO_3$ Multilayers for Coated Conductor Applications," *Appl. Phys. Lett.* **76**, 760–62 (2000).

2. S. S. Shoup et al., "Epitaxial Thin Film Growth of Lanthanum and Neodymium Aluminate Films on Roll-Textured Nickel Using a Sol-Gel Method," *J. Amer. Ceram. Soc*. **81**(11), 3019–21 (1998).

1.9 CONDUCTIVE BUFFER LAYERS AND OVERLAYERS FOR THE ELECTRICAL STABILITY OF COATED CONDUCTORS

C. Cantoni, T. Aytug, D. T. Verebelyi, M. Paranthaman, E. D. Specht, D. P. Norton, and D. K. Christen

1.9.1 Introduction

At the stage of implementation, coated conductor tapes will have to be electrically and thermally stabilized against transient conditions in which the current may exceed I_c of the HTS coating. Coated conductors are typically formed of a 50-µm-thick metallic substrate (Ni or Ni alloys), one or more insulating oxide buffer layers with a total thickness of 0.5 to 1 µm, and an HTS film, preferably greater

than 1 μm thick. As a benchmark, we can assume that the HTS film (usually YBCO) carries a current density of 1×10^6 A/cm^2 in the superconducting state at liquid nitrogen temperatures (64 to 77 K). In the event of a transient to the dissipative regime, the power generated per unit area in such an electrically isolated 2-μm-thick HTS layer would exceed 10^4 W/cm^2, resulting in destruction.

To remove the heat generated from the HTS layer and to restore superconductivity, the superconducting film has to be electrically coupled to a conductive metallic layer. This coupling provides a lower overall resistivity during transient losses of superconductivity and, consequently, a lower dissipation in the net conductor. In addition, coupling to a good metal greatly increases the thermal conductivity of the entire tape, significantly improving the outflow of heat to the surrounding refrigerant bath, and, therefore, improving the cooling rate of the conductor. The efficiency of cooling depends on many parameters of the application design. However, we consider the simple case of steady-state heat flow removed by contact of the tape with boiling liquid nitrogen, in which the maximum temperature excursion is determined by limiting the heat flux to a value below the critical heat flux of LN_2 at 77 K (10 to 20 W/cm^2).

Electrical coupling of the superconducting film to the metal layer can be envisioned in two different ways. A textured metal substrate of sufficiently low resistivity, as in the case of pure Ni or Cu, can itself provide the necessary stability for the HTS film if the buffer layer is conducting rather than insulating. For a 2-μm-thick YBCO coating that is electrically connected to an underlying 50-μm-thick base metal tape of pure nickel, the normal-state heat flux from each unit surface area would be only about 4 W/cm^2 per tape surface, well below the critical heat flux of liquid nitrogen.

On the other hand, a conductive buffer layer is not an effective route if the substrate of choice is a Ni alloy, which typically would have a resistivity comparable to the normal-state resistivity of the superconductor (~100 μΩ-cm at 100 K). In this case, stability can be achieved by applying a metal overlayer such as Cu or Ag on the superconducting film.

Figure 1.62 shows the calculated dependence on the substrate resistivity of the metal-layer thickness necessary to maintain the transient heat flux below 5 W/cm^2 when a 2-μm-thick HTS film carrying a current density of 1 MA/cm^2, is driven to the dissipative state. The effect on the overall tape current density, J_E, is also shown. We discuss important aspects of both approaches. We report on the development of a conductive bilayer composed of LNO and SRO for Ni-based coated conductors. In addition, we address some stability issues for alloy-based coated conductors by testing transport properties of structures formed by a metal cap layer deposited on YBCO films on single crystal STO substrates.

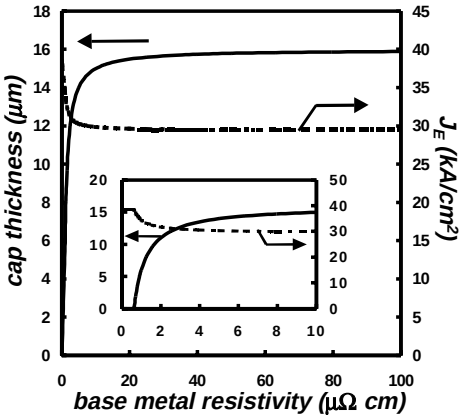

Fig. 1.62. The approximate calculated thickness of a highly conductive cap layer (Cu or Ag) required to stabilize the transient dissipative heat flux to a value ~5 W/cm^2 (2.5 W/cm^2 per tape surface), as a function of the 50-μm-thick substrate-tape resistivity. The HTS layer is taken to be 2 μm thick, carrying a current density of 1 MA/cm^2. The contact resistance between the HTS and the metal layer is assumed to be negligible. The inset shows the same plot expanded in the region of low resistivities.

1.9.2 Experimental

Both SRO and LNO are perovskite-type conductive metallic oxides with pseudocubic lattice parameters of 3.96 Å and 3.86 Å, and room-temperature resistivities of

about 300 μΩ-cm and 600 μΩ-cm, respectively. We have previously shown that highly textured LNO buffer layers can be successfully deposited onto Ni tapes, and we have subsequently optimized the deposition conditions to reproduce in these films the same degree of in-plane and out-of-plane texture of the Ni substrate. The LNO films for this study were deposited by dc sputtering from a 4-in.-diam powder target. The previously textured and annealed Ni substrates of approximately 3 × 15 mm in size were mounted on the heater block, and the chamber was evacuated to a base pressure of 1×10^{-5} mTorr. After a target presputtering, the temperature was raised to 480°C and the film was grown in a background total pressure: $P[(96\%Ar + 4\%H_2) + O_2] = 10$ mTorr, with $P[O_2]/P[96\%Ar + 4\%H_2] = 0.05–0.1$.

The LNO films show several advantages as first buffer layers for RABiTS™ tapes. They can be easily deposited by sputtering at a lower temperature than that used for other oxides (like YSZ and CeO_2); LNO deposits on Ni are dense and continuous, with no observed microcracks in films to thicknesses of 0.5 μm. However, YBCO films on LNO/Ni structures show considerably suppressed T_cs (70–75 K) because of Ni diffusion from the substrate though the LNO film into the YBCO.

Unlike LNO, SRO behaves as a good Ni diffusion barrier and is chemically compatible with YBCO, as demonstrated by the growth of YBCO films with J_c (0 T, 77 K) = 4 MA/cm^2 on SRO-buffered $LaAlO_3$ single crystals. Because we were not able to grow epitaxial SRO films directly on Ni, SRO was deposited after the first layer of LNO had been sputtered on the Ni substrate. Highly (200)-oriented SRO films were deposited by both sputtering and PLD on LNO/Ni samples that had usually been exposed to air after the LNO deposition. For both methods, the deposition temperature ranged between 600 and 650°C. The PLD deposition was carried out in a background oxygen pressure of 1 to 5 mTorr and with a laser pulse energy of 4 J/cm^2. In the sputtering system, SRO was grown in pure Ar at a pressure of 10 mTorr. YBCO films subsequently deposited on these samples showed J_c (0 T, 77 K) values of around 1.2 MA/cm^2 and therefore comparable to those of epitaxial YBCO films on standard, insulating CeO_2/YSZ/CeO_2 buffered Ni substrate. The YBCO films were deposited by PLD at a substrate temperature of 780ºC and an oxygen background pressure of 100 mTorr.

1.9.3 Discussion

Figure 1.63 shows a comparison between four-probe resistivity measurements for the Ni substrate, the net SRO/LNO/Ni parallel, and the completed YBCO/SRO/LNO/Ni structure. The thickness values are 140 nm, 150 nm, 325 nm, and 50 μm for YBCO, SRO, LNO and the Ni substrates, respectively. Because of the electrical connection between the YBCO and the Ni substrate through the buffer layers, the resistivity of the YBCO/SRO/LNO/Ni structure is nearly a factor 30 smaller, and the resistance is a factor 10^4 smaller than that of the isolated YBCO film at 100 K. However, were there complete electrical connection between the YBCO film and the Ni substrate, the resistivity shown in Fig. 1.63 for the total structure would be indistinguishable from that of the bare Ni substrate.

Cross-sectional SEM studies of the YBCO/SRO/LNO/Ni architecture have shown that the additional resistivity is possibly due to a discontinuous NiO layer that forms under the oxidizing conditions of YBCO deposition. Because NiO has a lower free energy of formation than either LNO or SRO,

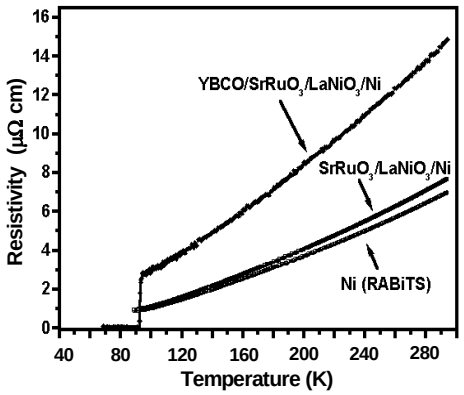

Fig. 1.63. The net resistivity measured using four-terminal potentiometric measurements of the bare, textured nickel substrate; the nickel tape coated with the conductive bilayer buffer $SrRuO_3/LaNiO_3$; and the complete structure of YBCO/SRO/LNO/Ni. The distance between current probes is 10 mm; the distance between voltage probes is 4 mm.

its formation is expected, at a rate that is dependent upon the kinetics of oxygen diffusion to the LNO/Ni interface. The formation of this insulating layer could be explained by the diffusion of Ni from the metal substrate into the LNO layer, thereby resulting in deterioration of the stability of LNO and probably formation of a polycrystalline mixture of La-O and Ni-O. The deterioration of the interface between LNO and Ni and the formation of a NiO layer (although thin and discontinuous) is not desirable for the development of a robust conductive architecture. Ongoing research is focusing on solving this problem by changing the buffer-layer architecture or by passivating the Ni surface with a different metal layer.

In the case of coated conductors that use a high-resistivity metal substrate, stabilization is carried out by depositing a metal layer on top of the superconducting film. Such a metallic film does not have to grow epitaxially on YBCO and could be deposited at room temperature. However, as in the case of the conductive buffer layers, the interface between metal and YBCO must have a low areal resistivity to provide an effective electrical connection. It is known that the YBCO surface reacts with air to form $Ba(OH)_2$ and $BaCO_3$. Humidity can give rise to other types of surface reconstruction that involve absorption of H_2O molecules inside the YBCO crystal lattice. For this reason, ex situ sputter-deposited Ag on the YBCO surface shows surface resistivities that are too high. A post-anneal in O_2 at 500°C reduces the contact resistivity to values in the 10^{-5} Ω-cm^2 range, which may be suitable. (Note: such a procedure is not possible for Cu on YBCO.) However, if the contact surface resistivity of the Ag/YBCO interface is higher than 10^{-8} to 10^{-9} Ω-cm^2, then the *I-V* characteristics of our short-segment measurements will show a resistive behavior below J_c, with a slope determined by the fraction of current that partitions into the metallic cap layer.

In the best case, the *I-V* characteristic of a metallic layer in parallel with a superconductive layer shows zero voltage up to a current equal to the I_c of the superconductor, a small nonlinear transition region for current just above I_c, and, for $I > I_c$, a linear behavior with a differential resistivity given by that of the metal layer.

To conduct controlled tests of the stabilization provided by a metal cap layer for the case of YBCO insulated from the substrate, we measured *I-V* curves of Ag/YBCO and Cu/Ag/YBCO multilayers grown on insulating single-crystal STO. The latter might simulate the ultimate stabilizing structure for coated conductors. After growth, the YBCO films were cooled in a background oxygen pressure of 400 Torr at a rate of 10°C/min. At room temperature the chamber was evacuated to a background pressure in the range of 10^{-6} Torr; a 0.1-μm-thick Ag film was deposited in situ by PLD at a temperature below 100°C, a laser pulse energy of 4 J/cm^2, and a repetition rate of 10 to 40 Hz. The samples were then annealed ex situ in a furnace at 500°C for 30 min. Finally, a Ag or Cu film of a few microns in thickness was deposited to complete the stabilizing layer. Cu films were deposited at room temperature by dc sputtering in an Ar background of 20 mTorr, with a deposition rate of 30 Å/s.

Figure 1.64 is a comparison between the *I-V* curve taken in LN_2 for an isolated 130-nm-thick YBCO film and for the same YBCO film after being electrically coupled to a 1.5-μm-thick Ag cap layer. The substrate dimensions were 3 × 13 mm. The YBCO films showed critical current densities in the range of

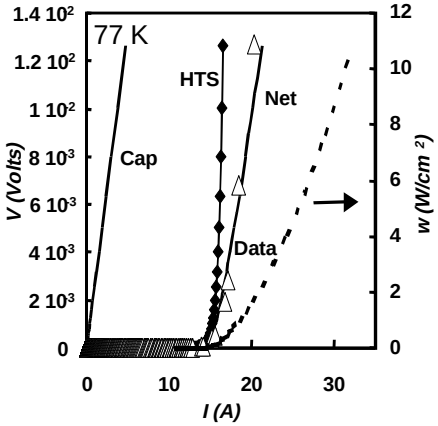

Fig. 1.64. Comparison between the *I-V* characteristics of a 130-nm isolated YBCO film (diamonds), the same YBCO film when electrically connected to a 1.5-μm-thick Ag film (net solid curve), and the Ag cap layer (cap solid curve). The dotted line indicates the power per unit area dissipated in the Ag/YBCO bilayer, assuming a negligible interface contact resistivity. The open triangles are the experimental data for the Ag/YBCO bilayer.

3 MA/cm^2 at 77 K in self-field. In the plot, the solid curves labeled "cap," "HTS," and "net" model the expected partitioning of the total current among the various layers, assuming a negligible interfacial resistance. The data agree well with the expected *I-V* curve for the net, parallel combination of the nonlinear superconductor, and the ohmic cap layer. The power dissipated in the bilayer is greatly reduced with respect to the isolated YBCO film: 1.7 W/cm^2 at $I = 1.7 \times I_c = 20$ A for the bilayer vs ~1700 W/cm^2 at the same applied current for isolated YBCO. We also noticed that the voltage measured in the bilayer below I_c lies in the noise level, indicating a sufficiently low contact resistivity of the Ag/YBCO interface.

Figure 1.65 shows the same plot generated for a sample formed of a 28-μm Cu film deposited on Ag/YBCO/STO. The Ag thickness is 0.1 μm, and the YBCO thickness is 130 nm. In this case, the stabilizing effect of the metal layer is much more evident. In fact, the linear differential behavior in the net *I-V* curve is much more pronounced for currents just above I_c, and the power dissipated at $2 \times I_c = 21$ A is only 0.24 W/cm^2.

The requirement of stabilization of a coated conductor (whether it is achieved by a metal cap layer or by an electrical connection to a low-resistivity substrate) and the requirement of maximum overall current density, J_E, are not independent. The simple model of conduction through parallel layers of different resistivities gives the dependence of J_E on the HTS layer thickness with the condition that, when the superconductor is in the dissipative state ($J_s \rangle J_c$), the power generated in the entire structure is smaller than a criterion value.

The expressions for the maximum overall current J_E and the corresponding superconducting film thickness d_s are as follows:

$$J_E^{max} = J_c \{(\rho_s - \rho_c)/\rho_s + 2[J_c^2 \rho_c^2 \rho_{m,c}^{-1}(d_m/w)]^{1/2}\}^{-1} ;$$

$$d_s = [(w\, d_m)/(J_c^2 \rho_{m,c})]^{1/2} ,$$

where $\rho_{m,c} = \rho_m \rho_c/(\rho_m - \rho_c)$, ρ_m is the resistivity of the metal substrate, ρ_c is the resistivity of the metal cap layer, d_m is the thickness of the metal substrate, J_c is the critical current density of the superconducting film, and w is the areal power dissipated in the net conductor.

Figure 1.66 shows a plot of J_E and the thickness of the stabilizing cap layer vs the YBCO thickness, assuming an upper limit of 5 W/cm^2 for the dissipated power and a J_c of

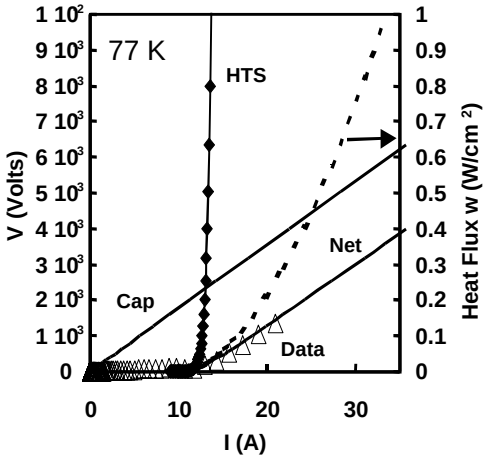

Fig. 1.65. Comparison between the *I-V* characteristics of a 130-nm isolated YBCO film (diamonds), the same YBCO film when electrically connected to a 28-μm-thick Cu film (net solid curve), and the Cu cap layer (cap solid curve). The dotted line indicates the power per unit area dissipated in the entire structure, assuming a negligible interface contact resistivity. The open triangles are the experimental I-V data for the Cu/Ag/YBCO trilayer discussed in the text.

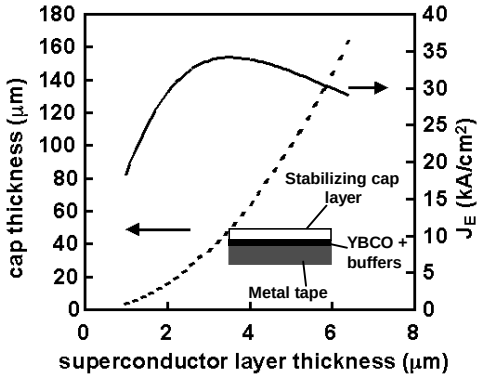

Fig. 1.66. A plot of the calculated cap layer thickness and resulting overall current density, J_E, as a function of the HTS layer thickness, for an envisioned coated conductor with a 50-μm-thick alloy substrate tape. The curves are generated for the case where J_c=1 MA/cm^2 and the generated heat flux is limited to 5 W/cm^2.

1 MA/cm^2 for the superconducting layer on an alloy tape. In this case, J_E has a maximum value of 34.1 kA/cm^2, which corresponds to a YBCO film thickness of 3.5 μm and a metal cap layer thickness of 46.3 μm. Further increase in the YBCO thickness beyond 3.5 μm, while providing more overall current, actually decreases J_E due to the rapid increase in cap layer thickness required to maintain stability.

In conclusion, further development of coated conductor tapes cannot neglect these fundamental considerations. The issues involve the thickness of a metallic stabilizing layer, its interface resistivity with the superconductor, and economic considerations, as required by stability limitations on the power generated in the dissipative regime.

1.10 GROWTH AND SUPERCONDUCTING PROPERTIES OF $YBa_2Cu_3O_{7-\delta}$ FILMS ON CONDUCTIVE $SrRuO_3$ AND $LaNiO_3$ MULTILAYERS FOR COATED CONDUCTOR APPLICATIONS

T. Aytug (ORNL); J. Z. Wu (University of Kansas), C. Cantoni, D. T. Verebelyi, E. D. Specht, M. Paranthaman, D. P. Norton and D. K. Christen (ORNL); and R. E. Ericson and C. L. Thomas (3M)

Recently, development of the RABiTS™ process emerged as a promising method for the fabrication of $YBa_2Cu_3O_{7-\delta}$ (YBCO)-based coated conductors supporting high current for electric-utility and high-magnetic-field applications operating at 77 K. The key issue in the RABiTS™ approach for conductor development is the necessity to use buffer-layer structures that are compatible with both the underlying metal substrate, Ni or Ni-alloy, and YBCO. The function of the buffer layer is twofold. It prevents the diffusion of Ni to the superconductor, and it transmits the biaxial texture of the metal substrate to the HTS film. Ideally, conductive-oxide buffer layers are preferred for coated conductors because they can provide an electrical contact between the thin HTS layer and the thick underlying metal substrate, improving electrical stability in the event of a transient to the dissipative regime. To date, buffer-layer studies have mainly concentrated on insulating-oxide buffers, and many multilayered buffers of insulating oxides have been developed for coated conductors. Development of conductive-oxide buffer layers on RABiTS™ has just begun.

In recent years, thin films of SRO, LNO, and conductive oxides have attracted considerable interest due to their potential for many technological applications. For instance, their epitaxial growth made the development of heterostructures based on superconductors and ferroelectrics possible. Both SRO and LNO are perovskite-type, conductive metallic oxides with pseudocubic lattice parameters of 3.93 and 3.83 Å with room-temperature resistivities of 280 and 540 μΩ cm, respectively. These values are close to those of orthorhombic YBCO and other high-temperature superconductors. High-quality epitaxial YBCO thin films having high superconducting transition temperatures (T_c = 91 K) and critical current densities ($J_c = 2 \times 10^6$ A/cm^2 at 77 K) can be grown on SRO-buffered single-crystal substrates. However, to date there have not been any reports on the successful growth of SRO layers on textured metals for the development of YBCO-based coated conductors. On the other hand, He et al.[1] reported recently growth of YBCO films on highly textured LNO buffer layers, successfully deposited onto Ni tapes. These YBCO films showed depressed T_c values (around 75 to 80 K) that are consistent with earlier results of YBCO films on LNO-buffered single-crystal substrates. The reason for this degradation was attributed to two possibilities: (1) direct chemical reaction between YBCO and LNO or (2) diffusion of Ni through the LNO layer into the YBCO. Hence, the observations that SRO is compatible with YBCO and that LNO is compatible with RABiTS™ has motivated the present study of SRO/LNO multilayers for a possible application as conductive buffer-layer structures for YBCO-based coated conductors. In this report, we

have made a comparative study of the structural and the superconducting properties (T_c, J_c) of YBCO films grown on multilayers of SRO/LNO and on single-layer LNO- or SRO-buffered (100) oriented LAO and STO substrates.

The deposition of LNO buffer layers was performed with a rf-magnetron sputtering system and a single-phase LNO powder target, which was pressed into a 95-mm copper tray. Typical sputtering conditions consisted of a mixture of Ar and O_2 at an Ar:O_2 ratio of 15:2, with a total pressure of 10 mTorr and a substrate temperature in the range of 550 to 600°C. The deposition rate was ~0.42 Å/s with a corresponding film thickness of about 3000 Å.

Pulsed laser deposition (PLD) was employed for the deposition of SRO and the YBCO films. A KrF excimer laser system operated at an energy density of ~3 J/cm^2 was used. During the deposition of SRO layers, the substrates were kept at 600°C in an O_2 atmosphere of 5 mTorr. The deposition of YBCO films was achieved at 780°C in 100 mTorr of O_2. After deposition, the O_2 pressure inside the PLD chamber was increased to 500 Torr. The films were then cooled to room temperature at a rate of 10°C/min. Typical film thicknesses for SRO and YBCO were 2000 Å and 3000 Å, respectively. The structures of the films were characterized with a Huber high-resolution X-ray diffractometer. A standard four-probe technique was used to evaluate the electrical properties of the samples. The values of J_c were assigned according to a 1 μV/cm criterion. Silver contacts were deposited onto the samples by dc-magnetron sputtering followed by an O_2 annealing in 1 atm for 30 min at 500°C. Secondary ion mass spectrometry (SIMS) depth profile and inductively coupled plasma (ICP) analyses of the samples were also made to document possible cation contamination of the YBCO.

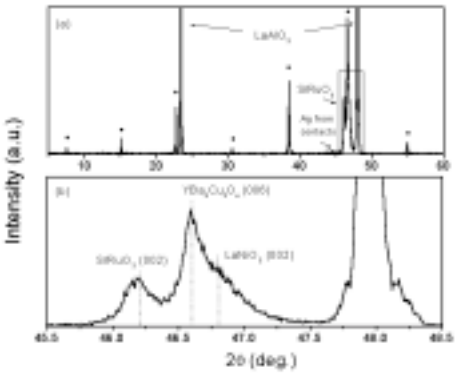

Fig. 1.67. An XRD θ-2θ scan for (a) YBCO/SRO/LNO/LAO multilayer. YBCO (00l) peaks are indicated by (•). The weak Ag peak is due to electrical contacts. (b) The LNO(002) scattering can be seen from the enlargement of the boxed region.

An XRD θ-2θ spectrum for a typical YBCO film on an SRO/LNO/LAO multilayer structure is shown in Fig. 1.67(a). The pattern indicates only (00l) reflections from both the YBCO and SRO layers, demonstrating that the YBCO/SRO/LNO layers are *c*-axis-oriented. The LNO (002) reflection can be seen as a shoulder on the YBCO (006) peak from the enlargement of the boxed region, as shown in Fig. 1.67(b). The epitaxial relation of YBCO films on the substrates is determined by XRD pole-figure analysis. The (102) pole figure of a YBCO film on SRO/LNO/LAO (Fig. 1.68) indicates a single epitaxy with YBCO(001)// substrate(001) and YBCO(110)//substrate(110). Similar crystallographic relations were observed for the YBCO/SRO/LNO/STO, YBCO/LNO/(LAO and STO), and YBCO/SRO/LAO multilayer structures.

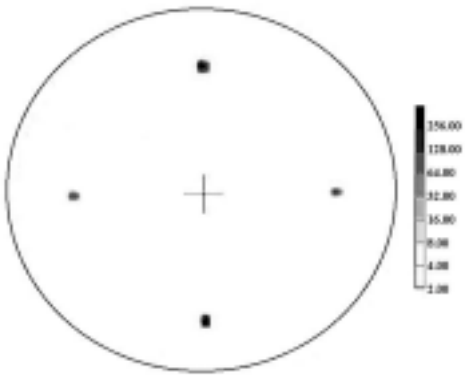

Fig. 1.68. The (102) pole figure of YBCO grown on SRO/LNO/LAO multilayer.

The differences in electrical and superconducting properties of the multilayer samples can be seen from the temperature-dependent resistivity curves in Fig. 1.69; an inset shows the enlarged view of the transition region. For comparison, the result of a YBCO film on a STO substrate is

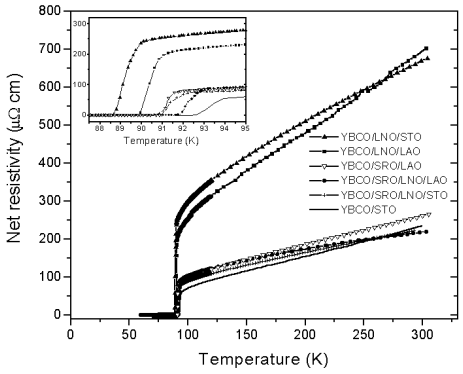

Fig. 1.69. Temperature dependence of the net resisitivity of YBCO/SRO/LNO/(LAO and STO), YBCO/LNO/(LAO and STO), YBCO/SRO/LAO, and YBCO/STO structures. Inset shows the enlarged view of the superconducting transition region.

included. Figure 1.69 shows the net resistivity (ρ_{net}), which is calculated from the total thickness of the conductive structure (YBCO + buffer layers). It is clear that an additional SRO buffer layer on LNO/(LAO and STO) improves the superconducting properties of the YBCO films by increasing T_c and decreasing ρ_{net}. The T_c of the YBCO/SRO/LNO/(LAO and STO) samples was observed to be higher than 90 K, being close to the T_c = 92 and 91 K values of the YBCO films grown on single-crystal STO- and SRO-buffered LAO substrates, respectively. However, T_cs of the YBCO/LNO/(LAO and STO) were lower than 90 K, with normal-state ρ_{net} being three to four times higher than those of YBCO/SRO/LNO/(LAO and STO). The differences in these results suggest the possible Ni contamination of the YBCO films from the LNO layers. In fact, SIMS depth profile measurements and ICP analysis of YBCO/LNO/(LAO and STO) samples qualitatively confirmed the presence of Ni in the YBCO. It is well known that Ni impurities in the superconducting structure can significantly reduce T_c and increase ρ. The expression for the resistivity ratio, ρ_{net}/ρ_Y, of an electrically connected bilayer structure can be given by

$$\rho_{net}/\rho_Y = [(A_Y + A_B)/(A_Y + (\rho_Y/\rho_B)A_B)] \ ,$$

where A_Y, ρ_Y and A_B, ρ_B are the cross sectional areas and the resistivities of the YBCO and the conductive buffer layer structures, respectively. According to this expression, ρ_{net}/ρ_Y is always >1 if $\rho_B > \rho_Y$, and <1 if $\rho_B < \rho_Y$. Because $\rho_Y \approx 300$ μΩ cm and $\rho_{SRO} \approx \rho_{LNO} \approx \rho_Y$, we should expect $\rho_{net} \approx \rho_Y$. Indeed, in contrast to YBCO films on LNO layers (where Ni contamination is an issue), the fact that ρ_{net} of the YBCO/SRO/LNO multilayer is similar to ρ_{net} of the YBCO on STO, and comparable to the one on SRO/LAO, is an indication of excellent electrical contact among all three layers. The T_c values of samples on LAO substrates appear to be ≈2 K higher than that of samples on STO substrates, suggesting that LAO serves as a marginally better substrate for growth of such buffer-layer structures. Confirmation of this effect needs further investigation.

Figure 1.70 shows the magnetic field dependence of the transport J_c for these samples at 77 K with the field applied parallel to *c*-axis. At zero applied field, all samples support high $J_c \geq 1.0 \times 10^6$ A/cm^2 with irreversibility fields (H_{irr}) ≥ 6 T. Consistently high J_c performance was observed for samples on SRO layers. Specifically, the self-field J_c of the YBCO/SRO/LNO/LAO is near 4.4×10^6 A/cm^2 with a high H_{irr} of 7.5 T (data not shown in plot for consistency). These values are comparable to those of the benchmark films of YBCO/STO ($J_c = 4.4 \times 10^6$ A/cm^2, H_{irr} = 8 T), and confirms high-quality epitaxial growth of YBCO on SRO/LNO

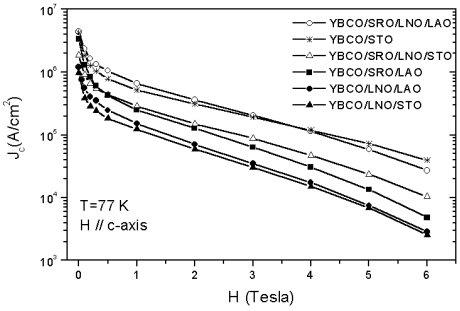

Fig. 1.70. Magnetic field dependence of J_c of YBCO/SRO/LNO/(LAO and STO), YBCO/LNO/(LAO and STO) and YBCO/SRO/LAO multilayers at 77 K. For comparison, J_c data of YBCO/STO are also included.

multilayers. However, the YBCO/LNO/(LAO and STO) multilayer structures showed somewhat lower J_c values (1.4×10^6 and 1×10^6 A/cm^2) with $H_{irr} \cong 6$ T. This is also consistent with the lower T_c values observed for the YBCO films on LNO layers. These results further support the low-level contamination of YBCO through LNO layers. Similar to the observations made in the ρ_{net} vs T data, J_c values of YBCO films on LAO substrates are also slightly higher than those on STO substrates.

In summary, structural and superconducting properties of conductive multilayer structures of YBCO/SRO/LNO, YBCO/SRO, and YBCO/LNO grown on LAO and/or STO substrates have been investigated. Highly crystalline, low-resistive and chemically compatible YBCO/SRO/LNO/(LAO and STO) samples have been obtained. The T_c and J_c of YBCO films on SRO/LNO multilayers have showed significantly higher values than those of the YBCO films grown on single LNO layers. These results indicate that the observed low-level Ni contamination of YBCO through the LNO layer can be prevented by an additional, highly stable SRO layer. This work also points to the use of the SRO/LNO structure as a potential buffer-layer architecture for the development of RABiTS™-based, fully conductive YBCO coated conductors.

1.10.1 References

1. Qing He et al., "Growth of Biaxially-Oriented Conductive $LaNiO_3$ Buffer Layers on Textured Ni Tapes for High-T_c Coated Conductors," *Physica C* **314**, 105 (1999).

1.11 EPITAXY OF $HgBa_2CaCu_2O_6$ SUPERCONDUCTING FILMS ON BIAXIALLY TEXTURED Ni SUBSTRATES

Y. Y. Xie, T. Aytug, and J. Z. Wu, University of Kansas, Lawrence; and D. T. Verebelyi, *M. Paranthaman, A. Goyal, and D. K. Christen, Oak Ridge National Laboratory*

Hg-based high-T_c superconductors (Hg-HTSs) with nominal composition $HgBa_2Ca_nCu_{n+1}O_{2n+4}$ (n = 0, 1 or 2) have superconducting transition temperature (T_c) up to 135 K, and epitaxial Hg-HTS thin films on single-crystal oxide substrates show high critical current density (J_c) values of up to 2 MA/cm^2 at 100 K and self-field.[1–6] These high T_cs and J_cs make Hg-HTSs desirable materials for high-current-carrying superconducting wire/tape applications at 77 K or higher. Due to a dramatic reduction of J_c across large-angle grain boundaries, a coated-conductor technology that employs biaxially textured metal substrates, such as Ni or Ni-alloys, becomes the most promising approach for producing high-J_c superconducting tapes.[7–9] This has motivated an extensive effort worldwide to develop HTS coated conductors. While significant progress has been made in the development of $YBa_2Cu_3O_7$ (YBCO) coated conductors, little has been achieved so far on Hg-HTS coated conductors.

An inherent difficulty associated with Hg-HTS coated conductors stems from the highly volatile and chemically active nature of Hg and related compounds. This results in a severe chemical diffusion/reaction at the interface between the Hg-HTS films and substrates, including most oxides and metals. Auger spectroscopy depth profiles had shown a broadened film-substrate interface, even in the experiment of using $SrTiO_3$ as substrate.[10] Consequently, Hg-HTS films grown on most oxide and metal substrates show poor-quality epitaxy and low J_c values, typically below 10^5 A/cm^2 at 77 K in zero applied field.[11] One possible solution for this interface problem is to search for suitable buffer layers. For example, $SrTiO_3$ shows superior chemical compatibility and lattice match with Hg-HTSs, but is difficult to deposit epitaxially on Ni substrates due to the three-component complexity, high growth temperature, and high oxygen partial pressure required. Although several metal buffers, such as Cr/Ag, have been shown to yield *c*-oriented Hg-HTS films on Ni, J_c remains relatively low due to the presence of impurities and poor in-plane alignment.[11]

To achieve high-quality epitaxy in Hg-HTS coated metal substrates, we employed the newly developed cation-exchange process[4–6,12] with two modifications: (1) oxygen atmospheric pressure, instead of that of argon,[5,6,13] was employed during growth of Tl-HTS precursor films to stabilize the oxide buffers of metal tapes, and (2) a fast temperature ramping annealing (FTRA)[14] was applied to minimize the unnecessary high-temperature processing time. In addition, a low temperature was maintained for the Tl-Hg cation exchange process. In this section, we report our recent experimental results on $HgBa_2CaCu_2O_6$ (Hg-1212) coated biaxially textured Ni tapes buffered with CeO_2/YSZ/CeO_2 tri-layers.

The biaxial texture of the Ni tapes was replicated throughout the buffer layers by epitaxial growth. Typically, such composite tapes show X-ray ω- and ϕ-scans with FWHMs of ~6° and ~7°, respectively. Details of the preparation have been described elsewhere.[15]

Fabrication of Hg-1212 films was accomplished in two major steps: synthesis of $Tl_2Ba_2CaCu_2O_8$ (Tl-2212) HTS films followed by Hg-vapor annealing of the films for conversion into Hg-1212 films. In the formation of Tl-2212 films, a precursor layer with nominal composition of $Tl_2Ba_2CaCu_2O_x$ and thickness of 450 to 1000 nm was first deposited by dc-magnetron sputtering. Superconducting epitaxial Tl-2212 films were then synthesized by using a closed-crucible heat treatment method.[16,17] For this technique, a Tl source pellet of chemical composition $Tl_{2+\delta}Ba_2CaCu_2O_x$ was made by thoroughly mixing Tl_2O_3 and $Ba_2CaCu_2O_5$ powders and pressing under 3 to 4 ton/cm^2 pressure. Several amorphous precursor films and a Tl-source pellet were enclosed inside a covered alumina crucible and then placed in a tube furnace. In an oxygen environmental gas, the whole assembly was brought up to between 800 and 830°C, annealed for 0.5 to 2 h, and then cooled to room temperature with a cooling rates of 10 to 30°C/min. Two different temperature-increasing rates were used, Set A and Set B. For Set A, the temperature-ramping rate was 10 to 20°C/min (slow temperature ramping annealing) and for Set B, ≥50°C/min (FTRA).

Tl-2212/CeO_2/YSZ/CeO_2/Ni films were then sealed in an evacuated quartz tube together with two pellets. One of these was a Hg-containing Ba-Ca-Cu-O pellet of composition $HgBa_2Ca_2Cu_3O_x$, and the other a Ba-Ca-Cu-O pellet of chemical composition $Ba_2Ca_2Cu_3O_x$. The entire assembly was maintained at 700°C for 12 h. After processing in Hg vapor, the Hg-1212 films were annealed in flowing oxygen at ~300°C for 1 to 3 h to optimize oxygen content. Due to conversion from the 2212 to the 1212 structure, a lattice contraction of ~13.3% along the *c*-axis yielded Hg-1212 films of thickness 400 to 850 nm, but no crack directly related to this lattice shrinking had occurred. Crystalline structures of the Hg-1212/CeO_2/YSZ/CeO_2/Ni films were analyzed by XRD θ-2θ spectra, ω- and ϕ-scans, and pole figures. SEM was employed to characterize the surface morphology of the samples. A standard four-probe electrical method was applied to measure the T_c and J_c of the Hg-1212 coated conductors, defining J_c at a criterion of 1 μV/cm. During the J_c measurements, a magnetic field (H) was applied parallel to the Hg-1212 *c*-axis, and the irreversibility field was defined according to the voltage-current power-law characteristic, $V \propto I^2$. At fields and temperatures above about 0.5 T and 85 K, respectively, J_c measurements were conducted over the entire sample dimensions of ~1 cm long by 0.3 cm wide. For measurements at lower fields and temperatures, the sample was photolithographically patterned to 60-μm wide lines to avoid problems of contact joule heating. Overlapping measurements were made to preclude any adverse effects of the patterning.

Our experimental results show clearly that the Hg-1212 films converted from Set B of Tl-2212 films have much higher quality in terms of surface morphology, epitaxy, and transport J_cs than that from Set A. For example, the FWHM of ω- and ϕ-scans for Hg-1212 films converted from Set B are around 7° and 9°, respectively, while that of Hg-1212 films from Set A are 9° and 15°, respectively. This explains the higher J_cs observed in the former, which is more than two orders of magnitude higher than that of the latter and suggests that the interface degradation may be minimized in the modified cation-exchange process. The results on Hg-1212 films converted from Set B are given in the following discussion.

The XRD θ-2θ spectrum of a Hg-1212/CeO_2/YSZ/CeO_2/Ni sample is shown in Fig. 1.71. The Hg-1212 (00l) peaks are strong and sharp. As shown in the inset of Fig. 1.71, the FWHM of the ω-scan spectrum (Δω) for the Hg-1212 (005) peak is 5.0°, somewhat narrower than that of the Ni substrate [7.7° for Ni (200) peak] and comparable to that of YBCO coated conductors.[15] This indicates that the Hg-1212 grains are highly *c*-axis oriented. The appearance of a weak NiO (111) peak implies that minor oxidation of the Ni interface occurs during the HTS processing. Apparently, about 25% of the Tl-2212 phase remains unconverted, as estimated from the maximum intensity of the Hg-1212 (005) and Tl-2212 (0012) peaks. Such an incomplete conversion was not observed for Hg-1212 films on single-crystal $LaAlO_3$ substrates grown under the same Hg-vapor annealing conditions.[4–6] However, the Tl-2212 precursor films on $LaAlO_3$ were grown in pure argon, instead of oxygen. A possible explanation for the incomplete conversion is that the Hg-Tl exchange rate may be influenced by the oxygen deficiency in the Tl-2212 precursor films. Further investigation is necessary to confirm this.

The Hg-1212 films are also well aligned in the plane of the substrates as evidenced from Hg-1212 (102) and (103) pole figures. Fig. 1.72 shows ϕ-scan peaks that are indicative of the in-plane alignment of the Ni, through the buffer layers YSZ and CeO_2, and the final Hg-1212 film. The ϕ-scan FWHM values (Δϕ) of the Ni (111), YSZ (111), CeO_2 (111) and Hg-1212 (102), progressively decrease somewhat from the substrate up through the top Hg-1212 layer. This is similar to that observed on YBCO coated conductors. Such a feature can occur only if the interface reaction/diffusion between the film and substrate is effectively suppressed.

The surface morphology of Hg-1212 on CeO_2/YSZ/CeO_2/Ni is dense and smooth, as evidenced in Fig. 1.73. Some voids and surface plateaus shown in this figure are also observed in Hg-1212 films on $LaAlO_3$,[5,6] and do not seem to strongly affect the supercurrent conduction. Energy dispersive spectroscopy (EDS) analysis of the impurity particles on the surface indicates that they are Tl/Hg-rich, and appear to be related to Tl-rich particles in the original Tl-2212 films.

The J_c vs H curves for a 600 nm-thick Hg-1212 on CeO_2/YSZ/CeO_2/Ni is shown in Fig. 1.74 for various temperatures. Typically, the Hg-1212/CeO_2/YSZ/CeO_2/Ni

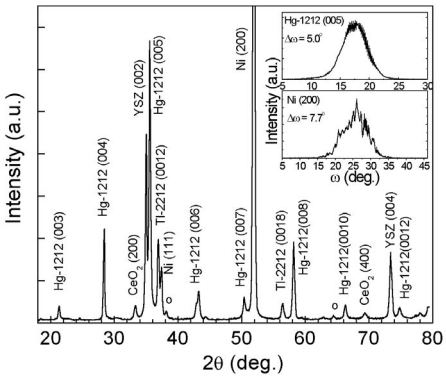

Fig. 1.71. XRD θ-2θ spectrum for a Hg-1212/CeO_2/YSZ/CeO_2/Ni sample annealed at 700°C for 12 h. Two "O" marks indicate the peaks of silver electrode contact. XRD ω-scan spectra of Ni (200) and Hg-1212 (005) peaks for this sample are shown in the inset.

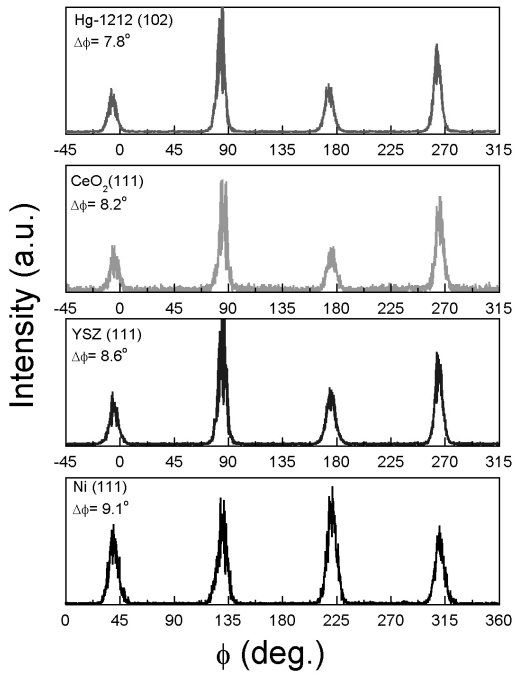

Fig. 2 Y.Y. Xie, *et al.*

Fig. 1.72. X-ray ϕ-scan spectra of Hg-1212 (102), CeO_2 (111), YSZ (111), and Ni (111) for a Hg-1212/CeO_2/YSZ/CeO_2/Ni sample. Replication of biaxial texture by epitaxy from the Ni substrate, through the buffers of CeO_2/YSZ/CeO_2, and to the Hg-1212 film is clearly.

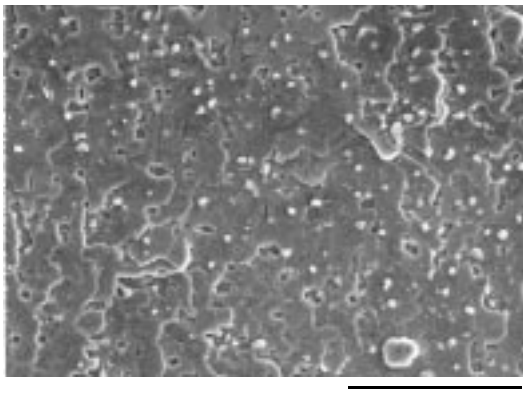

Fig. 1.73. SEM picture of a Hg-1212/CeO_2/YSZ/CeO_2/Ni sample. The surface is composed of dense, well-connected Hg-1212 grains.

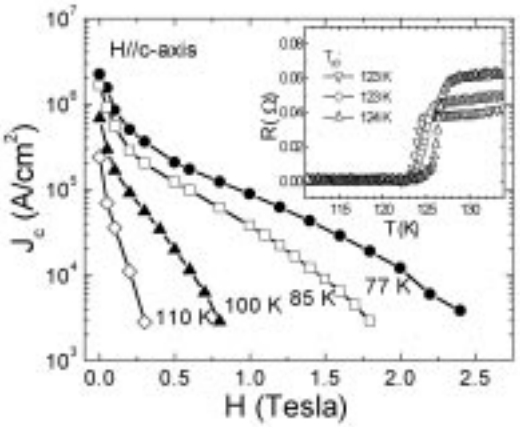

Fig. 1.74. J_c vs H curves at different temperatures for a 10-mm-long, 2.9-mm-wide, and 600-nm-thick Hg-1212/CeO_2/YSZ/CeO_2/Ni sample. The inset shows the resistive superconducting transition of three Hg-1212/CeO_2/YSZ/CeO_2/Ni samples.

samples indicate a superconducting onset transition at 125 to 127 K and reach zero resistivity at 123 to 124 K, as shown in the inset of Fig. 1.74. Prior to patterning, a critical current of 11.8 A at 100 K and of 4.1 A at 110 K was observed, corresponding to J_c values of 6.8×10^5 A/cm^2 at 100 K and 2.4×10^5 A/cm^2 at 110 K. At 77 K, J_c increases to 2.2×10^6 A/cm^2 in zero field, comparable to the best J_c on YBCO coated conductors. Irreversibility fields of ~2.4 T and ~0.8 T were observed at 77 K and 100 K, respectively. Such high T_c and J_c values suggest that these Hg-1212 coated conductors are very promising for electrical application at 77 K or higher temperatures. However, these J_c values are lower than those observed for Hg-1212 films on $LaAlO_3$ (100) single crystals.[4–5] For example, the zero-field J_cs of Hg-1212/$LaAlO_3$ are usually 4 to 5×10^6 A/cm^2 at 77 K and 1–2×10^6 A/cm^2 at 100 K. A possible reason for these differences is the presence of the unconverted Tl-2212 phases in the Hg-1212/CeO_2/YSZ/CeO_2/Ni samples. Because Tl-2212 films have lower T_cs (~108 K) and higher anisotropy, their J_c is lower than that of Hg-1212 films, especially at high temperatures. Optimization of the processing condition is necessary to complete the conversion from Tl-2212 to Hg-1212. As another factor, the quality of biaxial texture is significantly better for Hg-HTS films grown on single-crystal substrates. For example, the FWHM of the Hg-1212 (103) XRD pole is a few degrees for the coated conductor, but less than 1° for the films on single crystals. Experiments have shown that coated-conductor grain-to-grain alignments are typically sharper than the overall observed FWHM.[18] In addition, it is documented that grain boundaries with misalignment angles larger than 4 to 5° should be minimized to obtain improved J_c performance.[19]

In summary, high-J_c Hg-1212 films have been successfully coated on biaxially textured Ni substrates that are buffered with the layer sequence CeO_2/YSZ/CeO_2. Through a modified cation-exchange process, the Hg-1212 films grow epitaxially, replicating the in-plane texture of RABiTS™. Values of T_c for these films are in the range of 123 to 124 K. Zero-field J_c values are above 2 MA/cm^2 at 77 K and are up to 0.7 MA/cm^2 at 100 K. This good T_c and J_c performance provides new motivation to develop Hg-1212 coated conductors for electrical power applications at temperatures above 77 K.

1.11.1 References

1. S. N. Putilin et al., "Superconductivity at 94 K in $HgBa_2CuO_{4+\delta}$," *Nature* **362,** 226–28 (1993).

2. A. Schilling et al., "Superconductivity above 130 K in the Hg-Ba-Ca-Cu-O System," *Nature* **363,** 56–58 (1993).

3. L. Krusin-Elbaum, C.C. Tsui and A. Gupta, "High Current Densities above 100 K in the High-Temperature Conductor $HgBA_2CaCu_2O_{6-\delta}$," *Nature* **373,** 679–81 (1995).

4. J. Z. Wu, S. L. Yan, and Y. Y. Xie, "Cation Exchange: A Scheme for Synthesis of Mercury-Based High-Temperature Superconducting Epitaxial Thin Films," *Appl. Phys. Lett.* **74**(10), 1469–71 (1999).

5. S. L. Yan et al., "High Critical Current Density in Epitaxial $HgBa_2CaCu_2O_x$ Thin Films," *Appl. Phys. Lett.* **73**(20), 2989–91 (1998).

6. Y. Y. Xie et al., "Fabrication and Physical Properties fo Large-Area $HgBA_2CaCu_2O_6$ Superconducting Films," *Supercond. Sci. Tech.* **13**(2), 225–28 (2000).

7. Y. Iijima et al., "In-Plane Aligned $YBa_2Cu_3O_{7-x}$ Thin Films Deposited on Polycrystalline Metallic Substrates," *Appl. Phys. Lett.* **60**(6), 769–71 (1992).

8. X. D. Wu et al., "Properties of $YBa_2Cu_3O_{7-\delta}$ Thin Films on Flexible Buffered Metallic Substrates," *Appl. Phys. Lett.* **67**(16), 2397–99 (1995).

9. A. Goyal et al., "High Critical Current Density Superconducting Tapes by Epitaxial Deposition of $YBa_2Cu_3O_x$," *Appl. Phys. Lett.* **69**(12), 1795–97 (1996).

10. J. Z. Wu et al., "Epitaxial Growth of $HgBa_2CaCu_2O_{6+\delta}$ Thin Films on $SrTiO_3$ Substrates," *Physica C,* **277**(3&4), 219–24 (1997).

11. R. L. Meng et al., "Processing of Highly Oriented $(Hg_{1-x}Re_x)Ba_2Ca_2Cu_3O_{8-\delta}$ Tape with x~1," *Appl. Phys. Lett.* **68**(22), 3177–79 (1996).

12. Y. Y. Xie et al., "Synthesis of Hg-1223 Superconductors using a Cation-Exchange Process," *Physica C,* **322**(1&2), 19–24 (1999).

13. S. L. Yan et al., "Formation of Epitaxial $Tl_2Ba_2CaCu_2O_8$," *Appl. Phys. Lett*. **63**(13), 1845–47 (1993).

14. S. H. Yun et al., "Growth of $HgBa_2Ca_2Cu_3O_{8+\delta}$ Thin Films on $LaAlO_3$ Substrates using Fast Temperature Ramping Hg-Vapor Annealing," *Appl. Phys. Lett*. **68**(18), 2565–67 (1996).

15. C. Park et al., "Bend Strain Tolerance of Critical Currents for $YBa_2Cu_3O_7$ Films Deposited on Rolled-Textured (001) Ni," *Appl. Phys. Lett.* **73**(13), 1904–1906 (1998).

16. W. Y. Lee et al., "Superconducting Tl-Ca-Ba-Cu-O Thin Films with Zero Resistance at Temperatures of up to 120 K," *Appl. Phys. Lett.* **53**(4), 329–31 (1988).

17. M. P. Siegal et al., "Synthesis and Properties of Tl-Ba-Ca-Cu-O Superconductors," *J. Mater. Res.* **12**(11), 2825–54 (1997).

18. A. Goyal et al. "Using RABiTS™ to Fabricate High-Temperature Superconducting Wire," *JOM* **51** (7), 19–23 (1999).

19. D. T. Verebelyi et al., "Low Angle Boundary Transport in $YBa_2Cu_3O_{7-\delta}$ Coated Conductors," *Appl Phys. Lett.* **76**(13), 1755–57 (2000).

2. Technical Progress in Applications Development

2.1 SUPERCONDUCTING POWER TRANSMISSION CABLE

J. W. Lue, J. A. Demko, M. J. Gouge, P. W. Fisher, and C. A. Foster , Fusion Energy Division; J. P. Stovall, Energy Division; D. R. James and I. Sauers, Life Sciences Division; P. M. Martin, Metals and Ceramics Division

Significant progress was made during FY 2000 in three areas: the 30-m superconducting cable demonstration at Southwire, 5-m superconducting cable testing at ORNL, and cryogenic dielectric ageing experiments at Oak Ridge National Laboratory (ORNL).

During the year, the 30-m cable demonstration at Southwire became operational. The cable site and cryogenic system installation were completed during October to December 1999 (see Sect. 2.1.1). The electrical testing conducted before the cable was energized is described in Sect. 2.1.2. The testing included ac voltage withstands, measurement of critical current, extended-load current testing, and rated voltage testing. The 30-m superconducting cables were energized on January 5, 2000, for on-line testing (see Sect. 2.1.3). The cable has been successfully integrated into a 12.4-kV electric distribution system and is delivering on average more than 900 A to the Southwire manufacturing plants. The cable has operated reliably for more than 3000 h (as of Sept. 2000) and is continuing to operate.

Several different tests were conducted during the year on 5-m superconducting cables at ORNL. Fault currents were simulated and the effect on the superconducting cable was measured as described in Sect. 2.1.4. Cable termination development continued, as did the heat-load and impulse testing of the cable terminations and the cable (see Sect. 2.1.5). To manufacture a cable, the cable must be flexible enough to be rolled onto a reel. To demonstrate this capability, a cable-bend test was successfully completed (see Sect. 2.1.6). To install long lengths of cable in the field, shorter lengths must be spliced together. Section 2.1.7 describes the results of building and testing a cable splice.

The ability build longer lengths of superconducting cables has also been examined. The ac loss and thermal losses were analyzed for two different cooling arrangements to determine the benefits and limits of each (see Sect. 2.1.8). Also, potential utility applications of superconducting cables are discussed in Sect. 2.1.9.

The cryogenic dielectric ageing experiments conducted at ORNL to determine the expected life of the dielectric material used in the 30-m cables are described in Sect. 2.2.3.

Four technical papers were presented at the 2000 Applied Superconductivity Conference held in Virginia Beach, Virginia, on Sept. 17–22, 2000.[1–4] This technical progress report is drawn from the information reported in those papers.

2.1.1 30-m Cable Installation at Southwire

Southwire Company has installed, tested, and is operating the first industrial application of a high-temperature superconducting (HTS) cable system at its headquarters in Carrollton, Georgia. Southwire and ORNL have realized this operational system after an extensive four-year development effort.[1–12] Three 30-m cables (see Fig. 2.1) are powering three of the company's manufacturing plants, marking the first time a company has successfully made the difficult transition from the laboratory to a practical field application of an HTS cable. This report describes the installation, field-testing, and operation of this superconducting cable system.

The superconducting cables are installed as part of a three-phase power delivery system and are rated at 12.4 kV, 1,250 A, and 60 Hz, giving a rated system capacity of 27 MVA. A substation was constructed

to switch the cables into the power system serving the manufacturing plants. The cables are cooled with liquid nitrogen at temperatures from 70 to 80 K by a commercial cryogenic system supplied by PHPK, Inc.

Before the superconducting cables were placed into service, extensive off-line electrical testing was performed, including ac voltage withstands, measurement of critical current, extended load current testing, and rated voltage testing.

The superconducting cables were energized on January 5, 2000, for on-line testing. The cables and cryogenic system are being monitored and controlled by a programmable logic controller (PLC)-based system. The system performance is determined from trended data.

Fig. 2.1. The superconducting cable site. The three 30-m superconducting cables are shown in the center. To the left and right of the cable is the switchgear used to energize the cables. Behind the cables are the liquid nitrogen storage tank and the cryogenic system.

2.1.1.1 HTS Cable Site

The HTS cable site (inside the dotted box in Fig. 2.2) and is part of the electric system delivering power to three manufacturing plants. A switching substation constructed for the project allows either the superconducting cable or the overhead line, or both, to serve the load. A control building (shown in the lower left of Fig. 2.1) houses the electrical control and protection panel for the superconducting cable, the cryogenic control system, and a conference room. The initial preparation on the cable site began in October 1998.

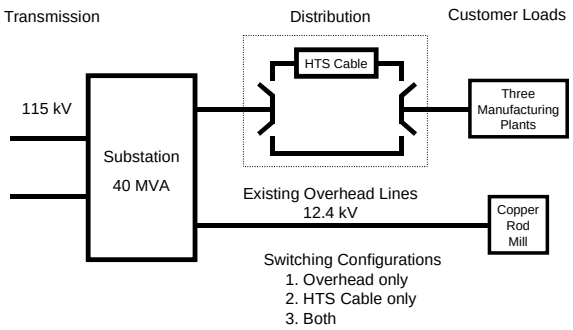

Fig. 2.2. Electrical block diagram of the HTS cable site.

Two 115-kV transmission lines provide service, one from Yates Power Plant and the other from Bremen switchyard, to the general transmission substation servicing Southwire. The transmission substation has a total capacity of 40 MVA with two 20-MVA matched, nonregulating, step-down transformers, 115 kV high side and 12.4 kV low side. The transmission switchyard is part of the Integrated Transmission System of Georgia Power Company.

Two 12.4-kV distribution feeders exit the substation. The one with the superconducting cable is the Southwire feeder; the other serves the Southwire Copper Division. Both feeders use 1033.5 ACSR (aluminum conductor, steel-reinforced), which is a typical type of conductor. The 12.4-kV protection system on the Southwire feeder is a vacuum breaker with a reclosing relay set for three reclosures before lockout. The symmetrical, three-phase fault current is around 14,000 A at 12.4 kV. The 5-m superconducting cable has been successfully tested at fault currents above this level.[3]

2.1.1.2 Cryogenic System

The HTS cable is cooled by circulating subcooled liquid nitrogen through the three cable phases. Based upon the 5-m cable testing program, the requirements for the 30-m cable cryogenic system were determined to be as follows: a heat load of 3000 W, an operating temperature range of 70 to 80 K, a flow rate of 1.3 L/s (21 gpm), and a maximum operating pressure of 10 bar.

The cryogenic system design consists of three main components: a liquid nitrogen storage tank, a cryogenic skid, and vacuum-jacketed piping. The cryogenic skid and vacuum-jacketed piping were competitively purchased from PHPK, Inc. The system was ordered in February 1999, factory tested in August 1999, delivered in September 1999, and commissioned in October 1999.

For the on-site commissioning, the following test procedure was followed:

1. visual inspection of each component,
2. functional check of machinery and instrument operation,
3. functional check of devices and indicators connected to the control system, and
4. verification of guaranteed performance parameters.

Performance testing included

1. measurements of the steady-state background heat load,
2. determination of the refrigeration capacity, and
3. monitoring of the insulating vacuum.

Demonstration of operating modes included

1. simulation of bringing on a warm phase of the cable,
2. bringing a redundant pump on line,
3. shutdown of fail-safe and emergency system, and
4. normal shutdown of the cryogenic system.

A PLC system is used to operate the cryogenic system during normal operation. System cooldown and restart are done manually due to the infrequent number of times that these operations are performed, the expense of programming, and the expected 2-year duration of the demonstration. The cryogenic system has essentially been in continuous operation since November 1999 and is quite reliable. Only minor equipment problems with some components (cryogenic valve actuator, control air compressor) were experienced.

2.1.2 30-m Cable Electrical Testing at Southwire

By mid-November 1999, the cryogenic system was in operation and the three 30-m superconducting cables were ready for testing, which was completed by December 1999. To minimize the risk to the cable system, system tests were performed incrementally and off-line. The off line testing of 30-m cables included high-voltage withstands, dc voltage/current tests, dc current load tests, and rated voltage tests. The dc voltage/current tests were repeated in June 2000 to determine cable performance after 6 months of operation, which included four to six cool-down and warm-up cycles and operation under variable loading conditions.

2.1.2.1 Voltage Withstand

The first off-line test to be performed placed voltage on the cable from a variable ac voltage power supply; voltage was applied one phase at a time to 11 to 12 kV and was held for 30 min to test the cable dielectric system. Phases 1 and 2 were maintained at 166% of rated voltage without breakdown. Phase 3, which has a slightly different geometry, was maintained at 230% of rated voltage without breakdown.

During the test, the charging current was measured. The cable capacitance was determined from the charging current and was compared with the calculated capacitance, as shown in Table 2.1. The calculated cable inductance is also shown. The cable surge impedance is 4 Ω, which is lower than that of a conventional copper cable. With this lower surge impedance, the ac superconducting cable has a longer critical length (the length at which charging current equals rated current) than that of a conventional copper cable. Thus the superconducting cable can be run in longer continuous lengths before the charging current dominates the cable's current-carrying capability.

Table 2.1. Measured and calculated capacitance
Values result in a surge impedance for the 30-m cable of about 4 Ω

	Phase 1	Phase 2	Phase 3
Capacitance–nF/m			
Measured	1.815	1.739	1.265
Calculated	1.778	1.778	1.207
Difference (%)	2.1	–2.2	4.8
Inductance–nH/m			
Calculated	31.4	31.4	38.2

2.1.2.2 DC Voltage/Current Test

To measure the dc voltage vs current relationship (V-I curve) of the cable, a 3000-A dc power supply was relocated from ORNL to Southwire. Voltage taps were temporarily installed externally to the main and shield bushings. The V-I curve was measured two phases at a time by connecting the dc power supply on two phases at one end and a short jumper between the phases at the other end. Phases 2 and 3 were measured, then Phase 1 and 2, so Phase 2 was measured twice. The V-I curves of the main conductors were measured, and then the shield conductor, as the cable is the cold dielectric design with coaxial conductors. The dc critical currents were as expected based on HTS tape performance and cable design. These tests were completed in November 1999. The V-I curve for Phases 2 and 3 is shown in Fig. 2.3; the linear behavior over most of the current range is due to the position of the external voltage taps, which involve extensive copper buswork and connectors beyond each end of the superconducting cable.

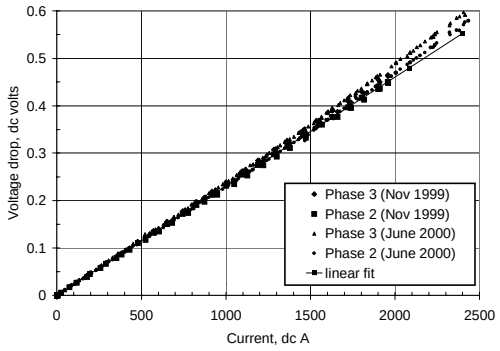

Fig. 2.3. The V-I curve for the main conductor of Phases 2 and 3.

The dc voltage/current tests were repeated in June 2000 to determine cable performance after 6 months of operation, four to six cool-down and warm-up cycles, and operating under variable loading conditions. As shown in Fig. 2.3, there has been no change in superconducting cable performance.

2.1.2.3 Extended Current Tests

Direct current load current tests were conducted to simulate average, rated, and emergency loading on the superconducting cables. As shown in Fig. 2.4, the extended load current tests were run with the dc power

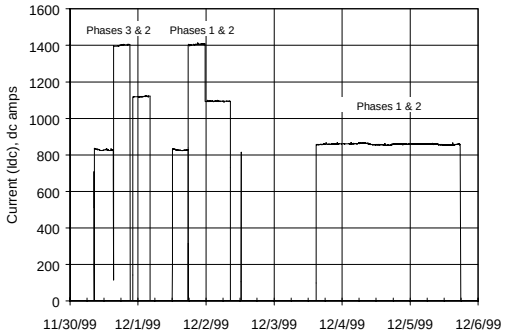

Fig. 2.4. Endurance testing on 30-m cable—dc current.

supply at ~800, 1200, and 1400 A each for 8 h on the two of the main conductors at a time. No changes in cable-cooling system temperatures were observed during these initial loading tests.

2.1.2.4 Rated Voltage Test

The substation supply was used for the next test, an extended, open-circuit, rated-voltage test. The cable breaker at one end was closed, and the other end remained opened, so no current was flowing through the cable. Phase voltage was maintained on each phase in several sequences up to 12 h. The cable dielectric performance was as designed.

2.1.2.5 Planned Outages

On November 25, a planned outage was taken to make the final changes to the substation. The day before, the cable had been put into idle mode and the cryogenic system was shut down. The day after, cryogenic system operations resumed.

2.1.3 30-m Cable Operation at Southwire

A data acquisition system records and archives key parameters of the cryogenic system, electrical system, and superconducting cable.

The current carried by Phase 1 during the month of May 2000 is shown in Fig. 2.5 and the average, minimum; maximum values for all three phases are shown in Table 2.2. The phase current imbalance of the load is very small, and as such, the graphs of the other two phases are almost identical to that for Phase 1.

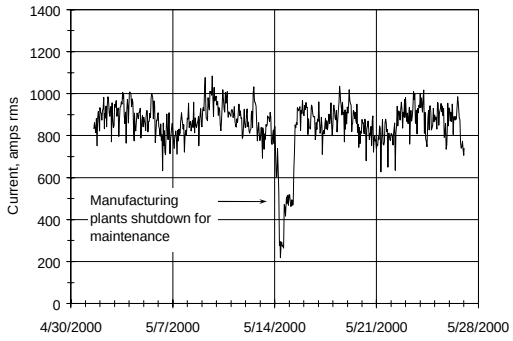

Fig. 2.5. May 2000—HTS Phase 1 current (1 h sampling).

The current carried by Phase 1 during the day of May 9, 2000, is shown in Fig. 2.6, the average, minimum, and maximum values for all three phases are shown in Table 2.2. The change in phase current around 6 a.m. and 6 p.m. correspond to work shift changes at the manufacturing plants.

Table 2.2. Operational statistics for May 2000

	Phase 1	Phase 2	Phase 3
May 2000		Current–A rms	
Average	853	863	845
Standard deviation	119	116	118
Minimum	219	244	218
Maximum	1,084	1,088	1,073
May 9, 2000			
Average	958	965	949
Standard deviation	63	61	62
Minimum	792	808	791
Maximum	1,108	1,115	1,100

The liquid nitrogen return-leg temperature variation for Phase 1 is shown in Fig. 2.7 (note: the *y*-axis value is not shown). The variation in the cable temperature is about 1 K.

The liquid nitrogen return-leg pressure for Phase 1 is shown in Fig. 2.8 (note: the *y*-axis value is not shown). The variation in the cable pressure is about 0.28 bar (4 psi).

Several cryogenic heat-load tests have been conducted, and the total cable system heat loss has been measured. The heat loss for all three phases of the 30-m cable and terminations at 600 A was found to be 1490 W. The components have been

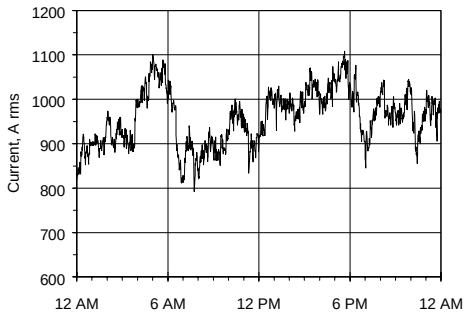

Fig. 2.6. May 9, 2000—HTS Phase 1 current (5 min sampling).

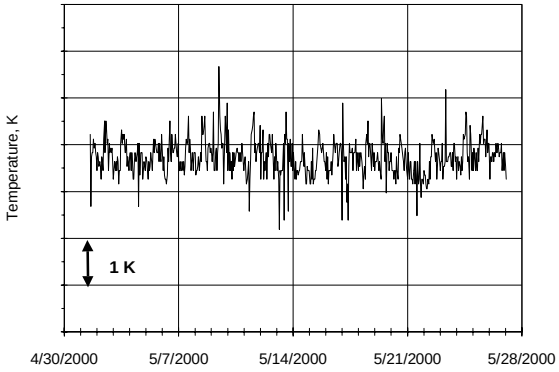

Fig. 2.7. May 2000—HTS Phase 1 return temperature (1 h sampling).

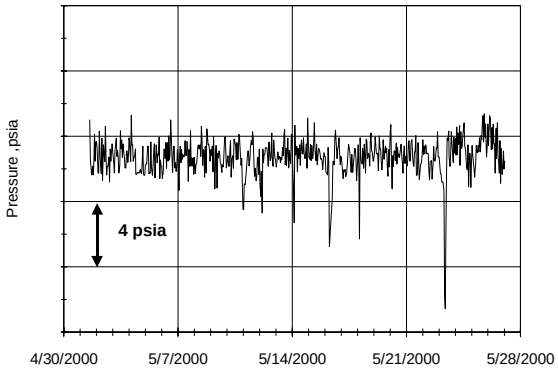

Fig. 2.8. May 2000—HTS Phase 1 return pressure (1 h sampling).

measured directly or separately, so a breakdown of the heat loss can be estimated. For each cable termination, the heat loss is 230 W, and there are six terminations. The cable cryostats, each a 7.62×12.7 cm (3×5 in.) vacuum-jacketed pipe, are 1 W/m per phase. At 600 A, the conductor and shield accounted for 0.2 W/m per phase.

2.1.4 5-m Fault-Current Tests at ORNL

Other crucial issues for the operation of the 30-m HTS cables are (1) whether they can survive the fault current (which can be more than an order of magnitude higher than the operating current) in the event of a short circuit and (2) how HTS cables and the cryogenic system would respond. Fault-current simulation tests were performed on the second 5-m HTS cable at the ORNL 5-m test facility. A 25-kA, 12-V dc power supply was reconfigured for this test. Tests were performed with fault-current pulses up to 15 kA for 0.5 s and 6.8 kA for 5 s. The cable survived all the fault-current pulses. We report the responses of the cable and the coolant during and immediately after the pulses in the following sections.

2.1.4.1 Cable Response to Simulated Fault Current Pulses

The cable was cooled down to about 81 K with liquid nitrogen (no pumping on the subcooler bath) at a pressure of about 4.7 atm and a flow rate of about 0.19 L/s (3 gpm). Short current pulses much larger than the critical current, I_c (about 910 A), of the cable were applied to the cable to simulate fault currents in case of an in-service short circuit. The voltages across the phase conductor and the joint, the current and voltage of the shield conductor, and the temperature and pressure of the coolant were monitored during the pulse and for a period after the pulse. Shots were made first with a 1-s pulse at increasingly higher current, from 4.8 to 12.8 kA. The pulse length was then increased to 2 s, and current pulses again up to 12.8-kA, were applied. The pulse length was shortened to 0.5 s, and a current of 15.3 kA was applied. The pulse length was then lengthened to 5 s, and a current of 6.8 kA was applied.

2.1.4.2 Cable and Joint Voltages

Figure 2.9 shows the current and voltage traces of the cable on a typical shot. A fault-current pulse of about 12.8 kA was programmed to be applied to the cable for 2 s. As soon as the current reached 12.8 kA, a voltage (V-cable) of about 3.2 V was developed across the cable. This and the voltage drops along the terminations and external power supply cables had apparently exceeded the power supply limit (12 V) and caused the current to drop. By the end of the 2-s pulse, the current was lowered to about 6.9 kA. However, the cable voltage continued to rise to over 5 V, indicating heating in the conductor. The cable-to-connector joint voltage (V-joint) was lowered from about 0.3 to 0.17 V—in the same proportion as the current drop.

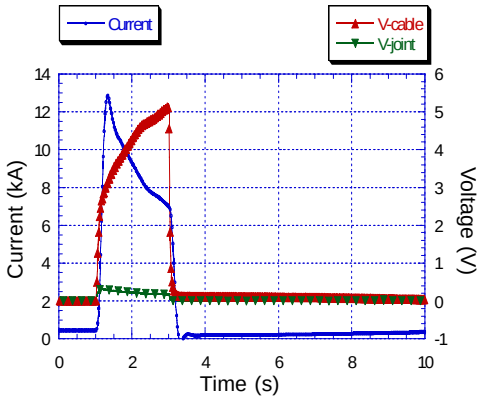

Fig. 2.9. Cable (phase conductor) and joint voltages in response to a 12.8-kA, 2-s fault-current pulse.

2.1.4.3 Cable and Joint Resistances

The cable voltage rise indicated that a temperature rise had occurred. To see more clearly how the cable heated up during the fault-current pulse, we divided the measured voltage by the corresponding current to get the resistance response of the cable. The result is shown in Fig. 2.10. At the beginning of the 12.8-kA pulse, the cable resistance went to 0.25 mΩ (compared with 0.54 mΩ at critical current) and increased to 0.72 mΩ by the end of the 2-s pulse. (The discontinuity at the beginning and end of the current pulse was due to dividing the cable voltages by the near-zero currents.) Based on the resistivity change of silver as a function of temperature, the resistance change of the cable indicated that the HTS conductor had heated to about 170 K by the end of the pulse. Although the cable voltage nearly disappeared after the current pulse (see Fig. 2.9), its resistance in Fig. 2.10 showed a relatively slow cooldown to about 0.1 mΩ 7 s later.

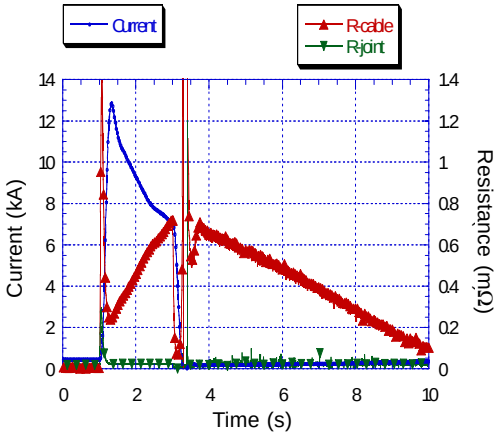

Fig. 2.10. Cable (phase conductor) and joint resistances in response to a 12.8-kA, 2-s fault-current pulse.

In the construction of the cable, the HTS tapes are separated from the coolant on the inside diameter with bedding tapes and a corrugated stainless tube and on the outside diameter with layers of Cryoflex dielectric tapes. Thus, cooling of the HTS tapes is essentially by conduction only. The heating of the HTS tapes during the fault-current pulses can be approximated as adiabatic. By integrating the product of current and voltage (the power) over the pulse in Fig. 2.9, we found that the total energy generated in the conductor in this shot was about 80 kJ. Using the silver specific-heat integral, we estimated that the conductor would heat up to about 175 K adiabatically. This is consistent with the estimated temperature rise based on the observed resistance increase. As Fig. 2.10 indicates the joint resistance remained at 24 mΩ throughout the shot. Thus, there was no noticeable temperature rise on the joint because of its better cooling condition (with direct contact with LN_2).

2.1.4.4 Cable Resistance in the Over-Current Regime

In response to an over-current, the cable resistance becomes much higher than its value at I_c. Therefore, the HTS cable possesses an intrinsic current-limitation function. Determining the extent of the rise in cable resistance during an over-current will tell the extent of the current limitation offered by the cable. From the moments the different pulsed currents reached their peaks, we found the cable resistance at all 15 over-current shots. The result is shown in Fig. 2.11 as a function of current. The 5-m cable resistance increased rapidly from 0.54 mΩ at I_c to 0.31 mΩ at 15.3 kA—nearly 600 times higher.

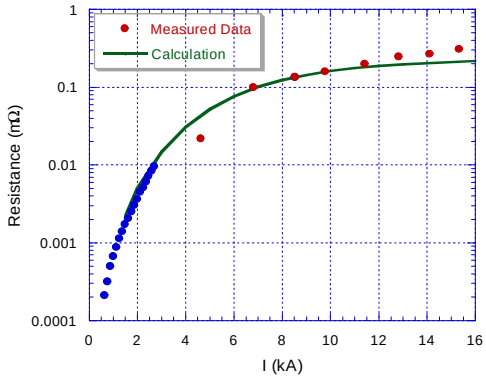

Fig. 2.11. Cable (phase conductor) resistance as a function of current. The data below 2.8 kA were taken from slow dc run shown in Fig. 2.12.

The dc V-I curve (see Fig. 2.12) showed that, above I_c, the voltage of the present superconductor increases in proportion to I to the 3.8th power (the n-value). Thus, the resistance of the superconductor at an over-current, I, can be scaled from its value of 0.54 mΩ at I_c by a factor of $I/I_c^{2.8}$. In addition to the superconductor, the present HTS tape contains 70% of silver in the composite. Given a resistivity of 0.3 mΩ-cm, the resistance of the silver matrix in the cable is estimated to be about 0.25 mΩ at liquid nitrogen temperature. The cable resistance in the over-current regime was then calculated by paralleling the scaled HTS resistance with the silver resistance. The result is shown as the calculated curve in Fig. 2.11. It is seen that the measured data follows the calculated curve very well—proving that the power-law scaling of the HTS resistance above I_c is appropriate.

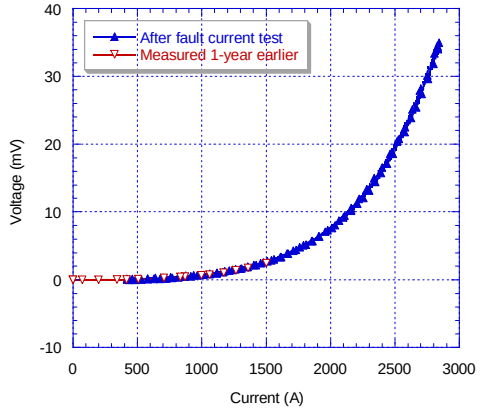

Fig. 2.12. The V-I curve of the 5-m cable after the fault-current tests compared with an earlier measurement.

The above analysis indicates that the HTS in the present cable shared the fault current equally with the silver matrix at 8.1 kA—about nine times the critical current. Below this value the current flows mostly in the superconductor; above this value more and more current flows in the silver matrix. At 15 kA, the HTS can carry only 15% of the fault current. Above 10 kA, the measured data lay above the calculated curve, indicating tape heating before the fault current reached its peak value.

2.1.4.5 Coolant Response to Simulated Fault-Current Pulses

Measured temperature changes. Because of the high-voltage drop developed across the cable during a fault over-current, the power is high and the total energy dissipation can be significant when the pulse length is long. When this energy is dumped into the coolant, the temperature and the resulting pressure rise may upset the cooling system. The shot shown in Fig. 2.9 produced the highest energy dissipation of all the shots. In Fig. 2.13, the responses of the temperature sensors are shown for this shot. The sensor "T-out" is located near the coolant outlet of the cable inside the termination; "T-far" is located at the cable side of the far-end termination. Neither of these sensors in the flowing coolant showed any

temperature rise during or after the current pulse. Only sensor "T-bus," located at the bus side of the far-end termination showed a temperature rise of about 5 K, 3 s after the pulse. The T-bus sensor was cooled by stagnant gas and was at a higher temperature of about 96 K.

The total energy produced in the cable in this shot was about 80 kJ. If half of this energy were dumped instantaneously into the liquid nitrogen in the inner pipe (the former) of the cable the temperature would rise by about 5 K. No such temperature rise was observed. The phase conductor was not cooled directly by the coolant, and it took tens of seconds for the conductor to cool (and thus to release heat to the coolant). Furthermore, the liquid nitrogen flow rate of about 0.2 m/s inside the pipe replenished the coolant fast enough to prevent any measurable temperature rise in the coolant.

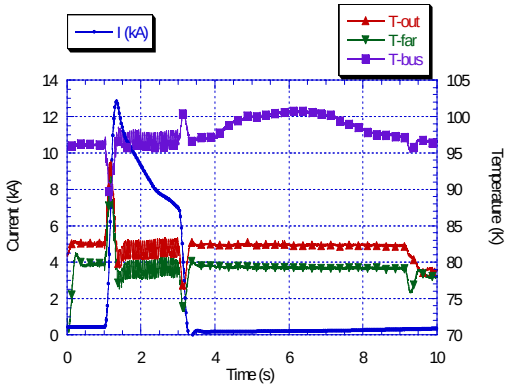

Fig. 2.13. Temperature responses of the various sensors for the 12.8-kA, 2-s over-current pulse.

Measured pressure changes. Figure 2.14 shows the corresponding pressure changes in a single shot. Contrary to the temperature response, both the inlet and outlet pressures start to rise 1 s into the pulse and reach a peak value of about 0.34 atm (5 psi) at 1 s after the pulse. Both pressure taps were meters away from coolant inlet and outlet of the cable. Apparently, the pressure wave reached them in a fraction of a second (with the speed of sound in liquid nitrogen). Because no temperature rise in the coolant was observed, we infer that the pressure rises resulted from transient heating in the terminations.

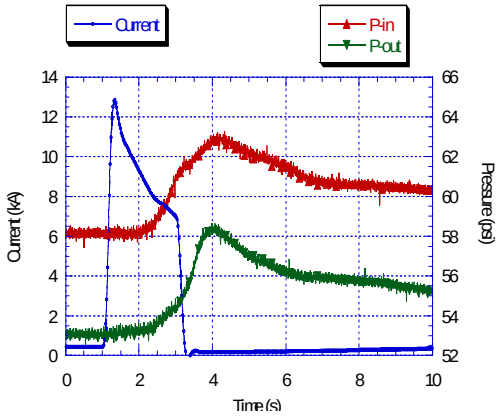

Fig. 2.14. Pressure changes in the coolant for the 12.8-kA, 2-s fault-current pulse.

Over the 1-h span of the 15 simulated fault-current shots, the accumulated temperature rise of the cable outlet coolant was found to be about 1 K, and there were no significant system pressure changes. Thus, repeated fault currents that are separated minutes apart would not upset the present HTS cable or the cryogenic system.

2.1.4.6 Shield Loop Voltage and Current

The voltage and current induced in the shield loop by the fault current in the phase conductor are other concerns. In the experiment, the two ends of the superconducting shield were tied together with copper cable and a current shunt to monitor the induced current. Fig. 2.15 shows the induced current in the shield loop for the 12.8-kA, 2-s fault-current shot. Only about 350 A and 120 A of transient currents were induced in the shield at the rise and fall of the phase conductor over-current. Part of the reason for these low values is the relatively long rise and fall time (of about 300 ms) of the over-current provided by the present power supply. If a fault current would rise faster, the induced transient in the shield would be

higher. During the 2 s of slow decrease of over-current, there was no measurable induced current in the shield.

Figure 2.15 shows that the maximum voltage developed over the shield conductor was less than 0.35 mV. Because this voltage is lower than the critical-current voltage of 0.5 mV for this cable and the induced transient current was lower than the critical current, we determined that the shield conductor stayed superconducting during the fault-current pulses.

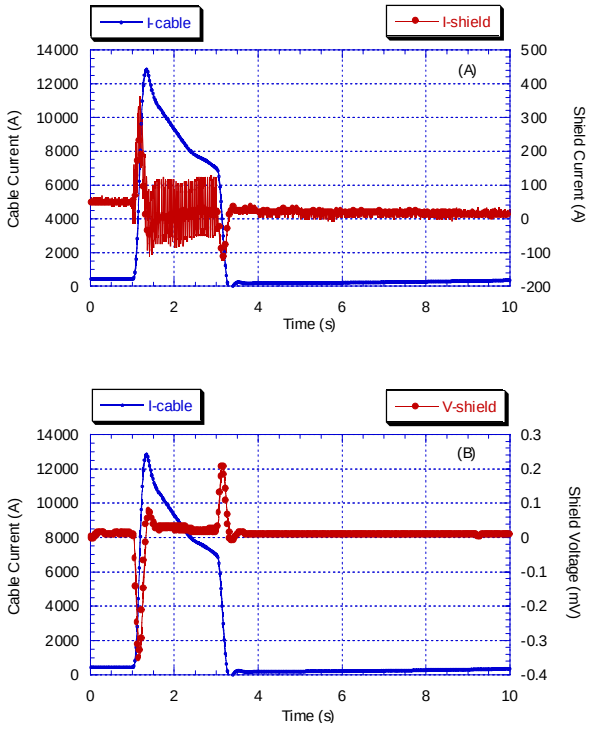

Fig. 2.15. Induced current and voltage in the HTS shield for the 12.8-kA, 2-s fault-current pulse.

2.1.4.7 DC Characteristics of the Cable

The dc V-I curve of the cable was measured after the present fault current tests to determine whether there was any significant degradation of the cable from the simulated fault current shots. Figure 2.12 shows the present V-I curve of the cable compared with a measurement made a year earlier. There is no significant difference in the two V-I curves. Between these two dc V-I measurements, the cable was subjected to high-voltage withstand tests to 18 kV, impulse tests to 90 kV, long-duration (72-h) testing at the design current and voltage, and tens of cool-down and warm-up cycles,[2,5] The cable showed no degradation in its dc characteristics throughout these tests. At the criterion of 1 μV/cm, the critical current of the cable remained at about 910 A.

2.1.4.8 Fault-Current Simulation Test Summary

In summary, fault-current simulation tests were performed at ORNL on the second 5-m HTS cable built by Southwire. A sequence of 15 shots of fault-current pulses was applied to the cable with peak current up to 15 kA—more than ten times the design current (for 0.5 s) and pulse lengths up to 5 s (at 6.8 kA). The cable survived all the fault-current pulses. A high-voltage drop (several volts as compared to 0.5 mV at I_c) was developed across the cable during the pulse that led to a drop of the fault current. The HTS cable resistance increased by two to three orders of magnitude in the presence of the fault currents. More than a 50% drop in fault current was observed. Thus, the HTS cable possessed an intrinsic current-limitation function.

No measurable temperature rise and only about 0.34 atm of pressure rise were observed in the liquid nitrogen coolant during all the fault-current shots, partly because the phase conductor HTS tapes were not in contact with liquid nitrogen. The cryogenic system was not upset by any of the fault-current shots or by the accumulated effects of the shots over the 1-h test period. Also, the induced current and voltage on the HTS shield conductor were minimal.

Finally, the dc voltage-current measurements showed no degradation in the HTS cable from the earlier high-voltage, high-current tests; thermal cycles; or the present fault-current tests.

The 30-m HTS power cable demonstration facility at Southwire is protected by breakers rated at 13 kA for 0.7 s and 8 kA for 1 s. The present laboratory simulation fault-current test results give confidence that the in-service 30-m HTS cables will survive fault currents due to any foreseeable short circuit and that the cryogenic system will not be adversely disturbed by such events.

2.1.5 Cable Termination Development

The cable termination is the interface from the superconductor operating in a pressurized liquid nitrogen environment to copper operating at room temperature at atmospheric pressure. A new pressurized termination concept,[2] developed and used on the 30-m cable system, operates with pressurized liquid and gaseous nitrogen without the need for cold electrical bushings. The entire termination is at cryogenic system pressure. Each termination has two conventional warm bushings with no significant thermal stresses. In an extended test program during 1999 and 2000, the pressurized termination successfully completed the following tests:

- extended operation at design current (1250 A ac rms) and voltage (7.2 kV phase-to-ground),
- ac withstand test to 18 kV for 30 min with no breakdown,
- overcurrent testing to 12.8 kA for 2 s, and
- measurement of termination heat loads.

The heat loads have been reduced through a series of design improvements during the past year, as shown in Fig. 2.16, with the best performance on the 30-m cable terminations.

Based on the successful test program in the 5-m cable test facility, a decision was made to use six of these pressurized terminations in the three-phase, 30-m HTS cable. The present heat load on the pressurized terminations installed on the 30-m cable with an ac current of 600 A is about 230 W per termination. This is considered reasonable because each termination has two conduction-cooled copper leads (pipes) with a theoretical minimum heat load of 44 W/kA each.

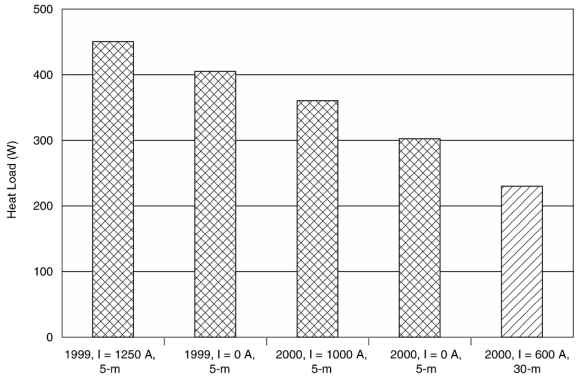

Fig. 2.16. Termination heat loads.

2.1.6 Bend Test of 5-m Cable at ORNL

A 5-m cable was removed from the test facility and was bent in a wooden fixture of the same diameter as a cable shipping spool (2.44 m). It was bent in one direction and the reverse direction four times. Cable testing before and after bending indicated no damage to the dielectric system; ac withstand and impulse loading were unchanged from previous tests. The cable critical current was reduced by about 15% after bending, as shown in Fig. 2.17.

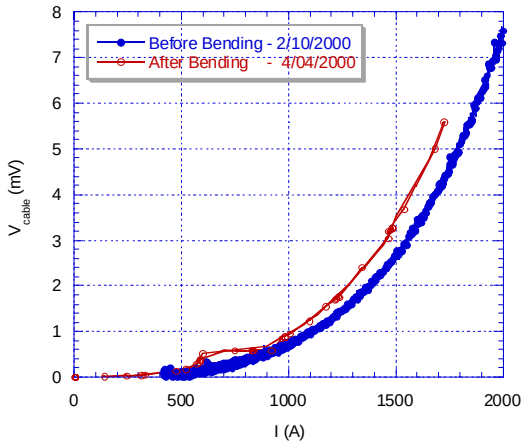

Fig. 2.17. Cable dc V-I curves before and after bending.

2.1.7 5-m Cable Splice

A cable splice has been made in the middle of a 5-m test cable at Southwire. The splice joins the HTS phase, the neutral conductors, and the Cryoflex dielectric tapes between the HTS conductors. This splice has been recently installed in the 5-m cable test facility at ORNL for testing. Initial tests were done with direct current, and the V-I curves shown in Fig. 2.18 were obtained. The critical current of the shield conductor is about 1900 A at a cable temperature of 80 K; the phase-conductor critical current is 2650 A at 77 K. The phase conductor *n* value around the critical current from the V-I curve is about 7.4, defined by the power law: $\rho = k \cdot J^n$, where ρ is cable resistivity (proportional to voltage drop) and *J* is the current density.

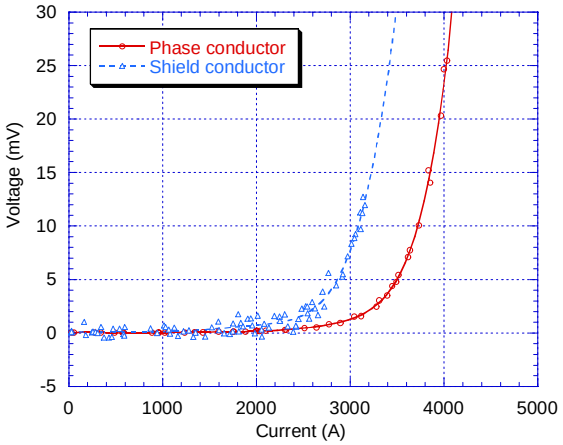

Fig. 2.18. Cable dc V-I curve for spliced conductors.

Shown in Fig. 2.19 is the temperature dependence of critical current with a linear fit to the data over a fairly narrow temperature range.

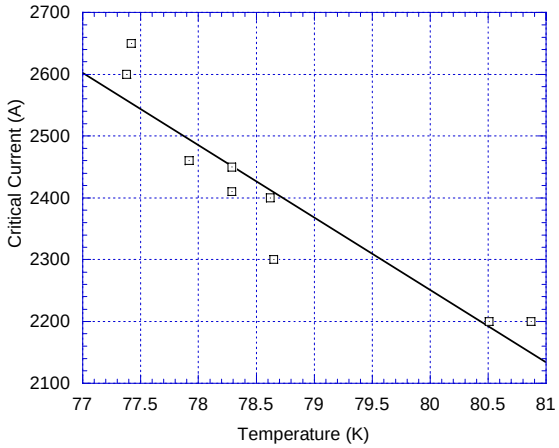

Fig. 2.19. Cable splice critical current vs temperature.

The dc characteristics of this 5-m cable with the embedded splice are much better than those of earlier 5-m test cables, primarily due to the improvement in the quality of the purchased HTS tape. Figure 2.18 shows a well-designed splice with less than 1 W of heat from the splice at the cable design current. Tests are in progress to quantify the ac losses and to confirm the ac voltage withstand capability of this cable splice.

2.1.8 Long-Length HTS Cables

The use of HTS materials for power transmission cable applications is being realized in prototype situations. It is well known that ac loss decreases as the temperature of the conductor decreases. Also, thermal losses are higher at lower temperatures, owing to the increased temperature difference between ambient and the cryogenic operating conditions. Both counterflow and parallel-flow cooling arrangements proposed in the literature significantly affect the temperature distribution along the cable. In this investigation, the counteracting ac loss and thermal losses are analyzed for both cooling configurations to determine the benefits and limits of each. The thermal insulation performance levels of materials vs those of typical systems in operation are presented. Widespread application of long-length flexible cable systems, from the refrigeration point of view, will depend on an energy-efficient cryogenic system that is economical to manufacture and operate. The counterflow arrangement will typically have a lower heat load; however, it has a length limit arising from the large pressure drop with this configuration.

2.1.8.1 HTS Cable Thermal Losses

Table 2.3. Cryostat dimensions

Nominal dimension (mm)	Counterflow	Parallel flow
Former diameter	38	38
Cable diameter	65	65
Cryostat inner diameter	75	75
Cryostat outer diameter	125	125
Return cryostat inner diameter	–	75
Return cryostat outer diameter	–	125

Cryostat. The HTS cable cryostat is taken to be a flexible double-wall construction with the dimensions listed in Table 2.3. The sink temperature, $T\infty$ = 300 K. Typical commercially available vacuum-insulated flexible cryostats have an effective, or actual field-installation thermal conductivity, k_{eff} of 0.0008 W/m per Kelvin. The local heat transfer per unit length can be calculated from Eq. (1) and depends on the local liquid nitrogen temperature, $T_{vi}(x)$, and the cryostat inner and outer tube diameters, D_{ci} and D_{co}. The temperature difference driving this heat-transfer term is typically over 220 K for the outer cryostat.

$$Q'_{cstat,i} = \frac{2\pi k_{eff}(T_{\infty} - T_{v,i}(x))}{\ln(D_{co}/D_{ci})} \quad (1)$$

Alternating-current and dielectric losses. The critical current was scaled from earlier measurements on the 5-m system.[10] From the measured linear fit in temperature, the critical current can be scaled with temperature by using a reference value of 3000 A at 77 K by the following:

$$I_c(T) = 6188.2 - 41.405T \quad (2)$$

The ac loss, P'_{ac}, in watt per meter, is computed by using the monoblock model,[15]

$$P'_{ac} = \frac{\mu_0 f I_c^2}{2\pi h^2}\{(2 - Fh)Fh + 2(1 - Fh)\ln(1 - Fh)\} \quad , \quad (3)$$

where $F = I_p/I_c$ (the ratio between the peak current in the ac cycle and the critical current of the superconductor), f is the frequency, and $h = (D_o^2 - D_i^2)/D_o^2$. The terms D_i and D_o are the inner and outer diameters of the superconductor. This study will show results for operating currents of 1500 A_{rms} and 2000 A_{rms}.

The dielectric loss depends on the design voltage of the cable. A nominal value of 0.05 W/m was assumed and is consistent with earlier work.[16]

2.1.8.2 Critical Current, Temperatures, Pressure Drops, and Refrigeration Loads

The critical current and temperature profiles are shown for the two long length cases at flows of 1000 g/s per phase and both cooling arrangements in Fig. 2.20 and Fig. 2.21. Temperature limits are clearly

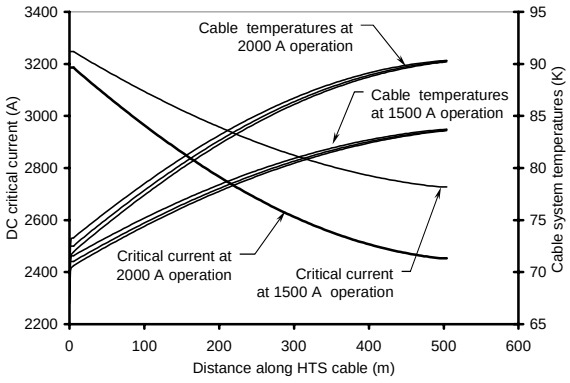

Fig. 2.20. Critical current and temperature distributions for a 500-m-long HTS cable transmission line in the counterflow cooling arrangement. The temperature rise produces a reduction in the critical current of the cable.

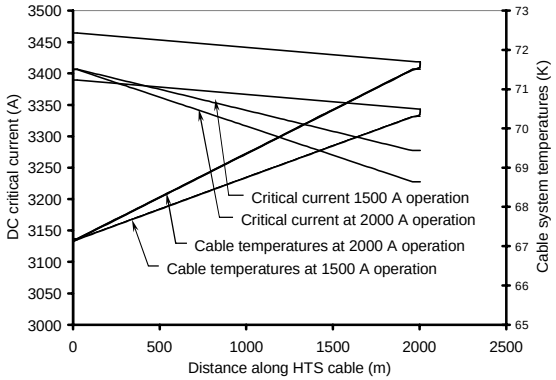

Fig. 2.21. Critical current and temperature profiles for a 2000-m-long HTS power transmission cable in the parallel cooling arrangement. The temperature rise is fairly low, maintaining a high critical current in the HTS conductor.

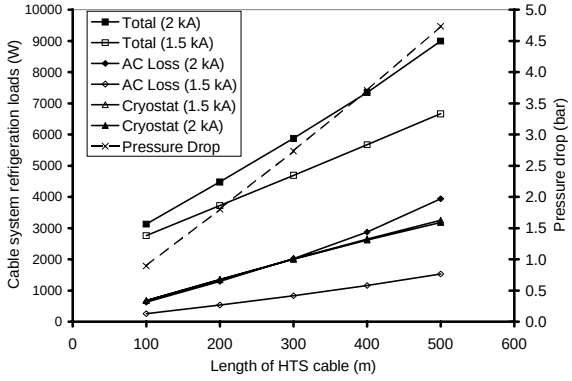

Fig. 2.22. Refrigeration loads (solid lines) and pressure-drop (dashed line) loads for a counterflow-cooled HTS power transmission system.

shown to exist in the counterflow case. In this case, the bottom temperature line is the former flow temperature, the center line is the HTS cable temperature, and the top line is the annular return flow temperature. The pressure drop for the 500-m counterflow case, shown in Fig. 2.22, is 4.7 bar. Increasing the flow to reduce the cable temperature would increase the pressure drop, which is already high, and would introduce the possibility of boiling in the cable. In both cooling arrangements the higher operating current cases produced higher temperatures, reducing the HTS cable critical current and increasing ac loss.

The refrigeration loads at 67 K and 1000 g/s per phase are shown for both cooling arrangements as a function of length in Fig. 2.22 and Fig. 2.23. These results show that running the cable at the lower current results in a significant drop in ac loss.

2.1.8.3 Factors That Limit Transmission Line Length

Many crucial factors in a HTS power transmission cable system depend on the cooling flow rate. A 250-m counterflow case and a 1000-m parallel-flow case were analyzed to determine the maximum cable temperatures and pressure drops at a current of 2000 A_{rms} at different flow rates. These results are presented in Figs. 2.24 and 2.25.

In both arrangements, higher temperatures are reached in the cable at lower flow rates. In the counterflow case, the system temperature, at which the liquid nitrogen is returned to the refrigerator, is at a lower temperature than the cable maximum. The opposite is true for the parallel-flow cooling arrangement. For low flows, the counterflow-cooled cable maximum temperatures are high enough to significantly reduce the superconducting properties of the cable. Increasing the flow reduces the maximum temperature at the expense of higher pressure drop. This is not the case for these flow rates in parallel flow, even at a length of 2000 m.

2.1.8.4 Long-Length HTS Cable Conclusions

Operational limits for long-length HTS cables depend on the cooling configuration, the cable ac loss, and thermal losses. AC and thermal losses vary with the temperature of the HTS cable and determine the flow required to keep all portions of the cable below a thermal limit. The required flows can exceed pressure-drop limits and result in formation of vapor that can degrade the cable insulation level. Detailed

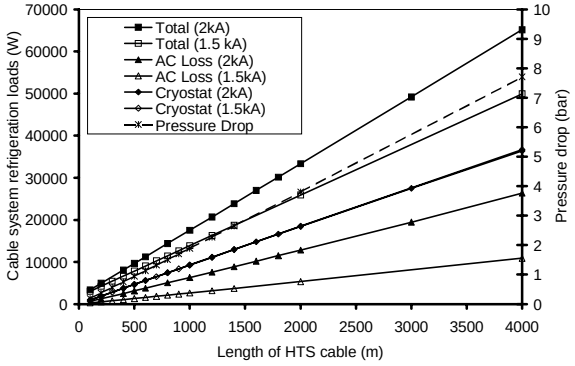

Fig. 2.23. Refrigeration loads (solid lines) and pressure drop (dashed line) for a parallel-flow-cooled HTS power transmission system.

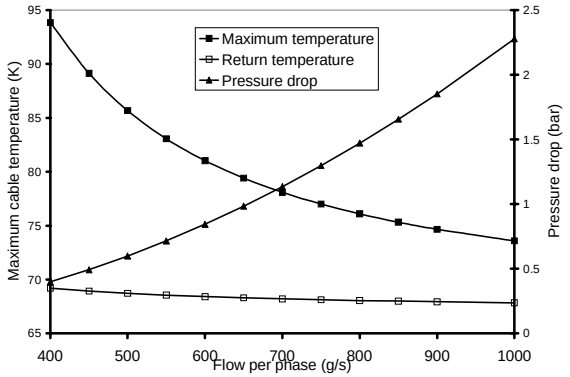

Fig. 2.24. Maximum cable temperatures and pressure drops for a 250-m-long counterflow-cooled HTS power transmission cable system.

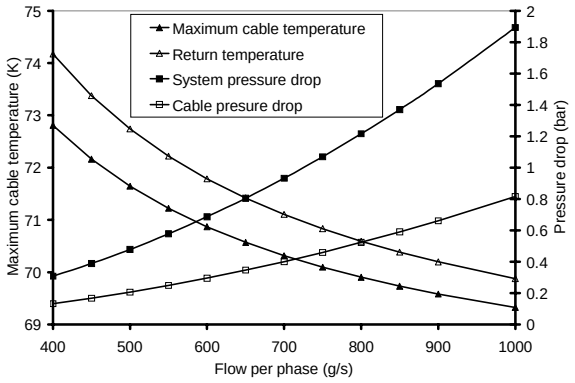

Fig. 2.25. Maximum temperature and pressure variations with flow for a 1000-m-long parallel-flow-cooled HTS power transmission cable system.

thermal analyses, such as demonstrated here, are necessary to determine the cooling configuration required to utilize HTS transmission lines most efficiently in practical applications. As more experience is gained from the operation of HTS cables, such as the Southwire system, these limits can be better defined.

2.1.9 Utility Applications

In the United States, approximately 3500 miles of high-voltage underground power cables use copper conductors to provide electricity to large metropolitan areas. These cables are aging, and many will be replaced over the next 20 years. Also, metropolitan areas continue to grow, requiring new cable capacity. Electric utility companies are looking for new cable technologies that increase power density and reduce losses and costs while maintaining the high reliability of conventional cables. Superconducting cables have the potential to meet these challenging requirements.

The cost of installing a new cable in a metropolitan area is expensive. The cable accounts for about 30 to 50% of the costs; installation is the major remaining cost. A superconducting cable can replace existing copper cables and can increase the power density by a factor of 3 to 8. The existing predominant cable design is a high-pressure oil-filled pipe-type cable consisting of a steel pipe 10.1 to 20.3 cm (4 to 8 in.) in diameter housing three copper cables and oil. These old copper cables and oil can be removed and replaced with superconducting cables with a significantly higher current capability, saving the installation costs of a new cable system.

The superconducting cable offers a new application of cables to metropolitan areas. With existing technology, high-voltage copper cables transmit power from the outskirts of cities to the downtown area,

where transmission substations lower the voltage and distribution circuits deliver power to customers. With this new superconducting technology, low-voltage, high-current superconducting cables can transmit power to downtown areas, allowing utility companies to move the high-voltage transmission substations out of the downtown area. These substations are very expensive to install and maintain in downtown areas, where land costs range from $100 to $600 per square foot.

This field demonstration has successfully shown the utility application of superconducting cables at distribution voltages and high currents. Potential utility applications include (1) substation to customer, (2) substation to substation, (3) extended substation bus, (4) substation express feeder, and (5) generating unit to step-up transformer.

2.1.10 References

1. J. P. Stovall et al., "Installation and Operation of the Southwire 30-Meter High-Temperature Superconducting Power Cable," paper 4LK04 presented at 2000 Applied Superconductivity Conference.

2. M. J. Gouge et al., "Development and Testing of HTS Cables and Terminations at ORNL," paper 4LGa02 presented at 2000 Applied Superconductivity Conference.

3. J. W. Lue et al., "Fault Current Tests of a 5-m HTS Cable," paper 2LB08 presented at 2000 Applied Superconductivity Conference.

4. J. A. Demko et al., "Practical AC Loss and Thermal Considerations of HTS Power Transmission Cable Systems," paper 2LB09 presented at 2000 Applied Superconductivity Conference.

5. J. W. Lue et al., "5-m Single-Phase HTS Transmission Cable Tests," to be published in *Advances in Cryogenic Engineering*, Vol. 45.

6. J. A. Demko et al., "Cryogenic System for a High Temperature Superconducting Power Transmission Cable," *Adv. in Cryo. Engr*., Vol. 45, Plenum Press, NY, 2000. Accepted for publication.

7. J. W. Lue et al., "Test of Two Prototype High-Temperature Superconducting Transmission Cables," *IEEE Trans. Applied Superconductivity,* Vol. 7, pp. 302–305, June 1997.

8. U. Sinha et al., "Design and Construction of LN_2—Cooled Prototype Superconducting Transmission Cable," *IEEE Trans. Applied Superconductivity,* Vol. 7, pp. 351–354, June 1997.

9. J. A. Demko et al., "Testing of the Dependence of the Number of Layers on the Performance of a One-Meter HTS Transmission Cable Section," *IEEE Trans. Applied Superconductivity,* Vol. 9, pp. 126–129, June 1999.

10. M. J. Gouge et al., "HTS Cable Test Facility: Design and Initial Results," *IEEE Trans. Applied Superconductivity,* Vol. 9, pp. 134–137, June 1999.

11. J. W. Lue et al., "AC Losses of Prototype HTS Transmission Cables," *IEEE Trans. Applied Superconductivity,* Vol. 9, pp. 416–419, June 1999.

12. J. W. Lue, M. S. Lubell, and M. J. Tomsic, "AC Losses of HTS Tapes and Bundles with De-coupling Barriers," *IEEE Trans. Applied Superconductivity,* Vol. 9, pp. 793–796, June 1999.

13. GASPAK, version 2.2, Cryodata, Niwot, CO, 1989.

14. G. Bogner, "Transmission of Electrical Energy by Superconducting Cables," in *Superconducting Machines and Devices*, S. Foner and B. Schwartz, eds., New York: Plenum Press, 1974, pp. 430–431.

15. G. Vellego and P. Metra, "An Analysis of the Transport Losses Measured on HTSC Single-Phase Conductor Prototype," *Supercond. Sci. Tech.* Vol. 8, pp. 476, 1995.

16. G. H. Morgan and J. E. Jensen, "Counter-Flow Cooling of a Transmission Line by Supercritical Helium," *Cryogenics*, May 1977.

2.2 SUPERCONDUCTING TRANSFORMER PROJECT

A U.S. Department of Energy (DOE) Superconductivity Partnership Initiative (SPI) project is under way to develop HTS utility power transformers. The SPI team is led by Waukesha Electric Systems (WES) with team partners IGC-SuperPower (IGC), Rochester Gas and Electric Company, and ORNL. In Phase I of the SPI, a 1-MVA HTS transformer was designed, built, and tested. The HTS windings were designed to operate near 25 K. The SPI is now in Phase II, with the objective of building a 5/10-MVA HTS transformer and testing it on the utility power grid to power the WES main transformer manufacturing plant. This transformer will also operate with windings at temperatures well below 77 K.

The team met several times to consider analysis and detailed designs for the 5/10-MVA transformer as well as conceptual designs for the 30-MVA transformer, the development of which is the ultimate goal of the project. The 5/10-MVA transformer design is being carried out as a scaledown of the final 30-MVA design. A new cryocooled ac loss test facility was put into operation, and three sample coils provided by IGC were tested. Electrical insulation tests focused on solid insulation materials, with the objective of validating their capabilities to handle the 25-kV operating voltage and 150-kV basic impulse level (BIL) of the 5/10-kV transformer.

2.2.1 AC Loss Testing

The variable-temperature liquid helium cryostat used on the earlier ac loss tests for the 1-MVA transformer had poor temperature stability for calorimetric tests and was expensive to operate. A new cryocooled ac loss test cryostat was commissioned early in the year for further tests on sample coils for the 5/10-MVA transformer. The cryocooler is a Cryomech GB-37 unit that provides over 30 W of cooling power at 20 K. Figure 2.26 is a photograph of the cryostat, which was mounted in a standard liquid helium dewar. The inner vessel of this dewar was evacuated to provide good thermal insulation for the cryocooler cold head and the sample. The dewar had its own liquid nitrogen shield, which provided additional radiation shielding. The sample coil was supported independently of the cold head and had flexible thermal connections to allow for thermal contraction. The sample support structure was maintained at roughly 40 K by the cryocooler first stage. The sample was thermally connected to the cold head through its leads and by flexible sheet-copper straps between the cold head and the outer surface of the sample coil. Grease, indium foil, or both were used in all mechanical joints to improve thermal contact.

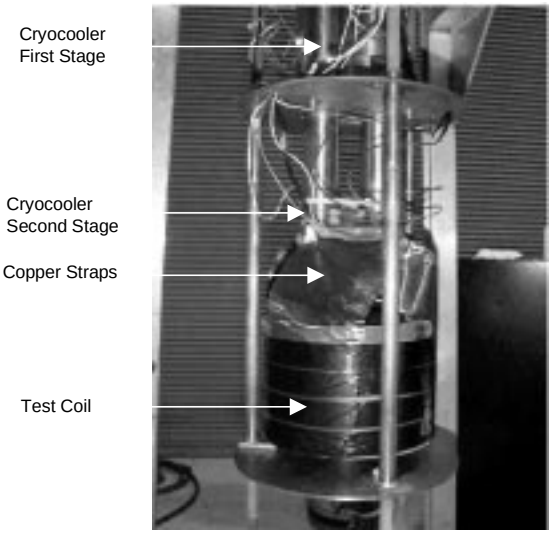

Fig. 2.26. Cryocooled AC loss test cryostat.

Temperature sensor voltages on the various turns in the sample coil were monitored while approximately 10-s pulses of ac current were applied. The initial *dV/dt* slopes for each current pulse were converted to ac loss power by comparing them with the slopes observed with known heat input from a heater co-wound with the conductor. This use of initial slopes is in contrast to the use of equilibrium temperature rise by most other workers. It allows fast, accurate spatial resolution of local losses on individual conductor turns before thermal diffusion alters the initial temperature gradients. If the heater

and conductor are in close thermal contact, definitive loss measurements can be made with no information required about either the effective heat capacity of the test coil or its thermal contact to the refrigerator.

Three test coils were provided by IGC during the fiscal year. Figure 2.27 is a photo of a typical test coil. Each coil had concentric primary and secondary windings in a configuration similar to that in the 5/10-MVA transformer. Because there was no iron core, the two windings were connected in series to ensure that they had equal currents. The two windings were connected to buck each other's magnetic flux so that there was net flux primarily only in the gap. This arrangement realistically reproduced the flux configuration in the windings of a transformer. The windings were supported by G-10 fiberglass mandrels and were enclosed in a cylindrical G-10 shroud with an overall diameter of 18.5 cm and a height of 12.5 cm. The test coils had wide copper foil leads that could be easily clamped to the cryocooler cold stage to allow direct cooling of the conductor.

Fig. 2.27. Typical AC loss test coil.

The coils were instrumented with voltage taps across various sections of the windings and with eight Allen-Bradley carbon resistors mounted on individual turns as thermometers. A calibrated Scientific Instruments RuO thermometer was also installed to provide an absolute temperature check for the carbon resistors. The bulk of the instrumentation was on the outer winding in each test coil. The outer winding also had a heater wound on top of the superconductor to supply a known heat input for calibration of the ac loss measurements. This heater was designed not to produce any appreciable eddy current heating during the ac current tests.

Test Coil 1 was wound with a surface-coated Bi-Sr-Ca-Cu-O (BSCCO)-2212 tape conductor with a self-field critical current of 8 to 10 A at 77 K. This conductor was of interest as a close simulation of the behavior expected for future second-generation surface-coated Y-Ba-Cu-O (YBCO)-123 tapes. Test Coils 2 and 3 were wound with multifilamentary BSCCO-2223 tape with a self-field critical current of about 24 A at 77 K. This tape was narrower than the BSCCO-2212 tape, allowing a more compact winding with higher current density.

Theoretical studies by IGC have indicated that the coil configuration has a strong effect on the its ac losses. Two different proprietary winding configurations were identified to be particularly promising for producing low losses. These configurations were designated as "1" and "2." Table 2.4 summarizes the parameters of the test coils.

Table 2.4. Parameters of ac loss test coils

Test coil	Conductor	Width (mm)	Winding configuration
1	BSCCO-2212	6	1
2	BSCCO-2223	4	2
3	BSCCO-2223	4	1

The test coil was cooled only by its leads and through the G-10 structure; therefore, cooldown was slow and about 10 h was needed to reach the minimum temperature of 20 to 25 K. This did not cause problems because the cryocooler could be operated overnight unattended. A heater on the cryocooler cold stage was used to reach higher temperatures. The temperature distribution in the test coils was uniform within ±2 K at the

start of each ac current run. Overall operation of the experiment was much easier and less labor-intensive than earlier ac loss tests with a liquid-helium-cooled variable-temperature cryostat. This along with the excellent temperature stability and unattended-operation capability of the cryocooler made its initial cost well worthwhile.

Figure 2.28 shows a typical plot of the resistance thermometer voltages vs time at 30 K for short duration pulses with successively increasing ac current on Test Coil 1. Voltages are plotted in arbitrary units. Each time the ac current was applied, sharp drops in resistance were seen, corresponding to heating of the resistor by the ac losses in the adjacent conductor. The strongest heating was seen on resistors R1 and R7, which were on the top and bottom turns of the outer coil and in a considerable perpendicular magnetic field. The heating was noticeably less severe on R6 and R8. These two resistors were mounted on the middle turns of the outer and inner windings. These turns had the lowest perpendicular field and thus the lowest ac losses. The test coil temperature increased by about 3 K during the run; this temperature increase is not characteristic of that expected for the actual transformer windings, which will be thermally coupled to the cryocooler much more tightly than the test coil. Similar plots were obtained during the calibration runs, except that the heater had roughly the same effect on all the turns, as expected.

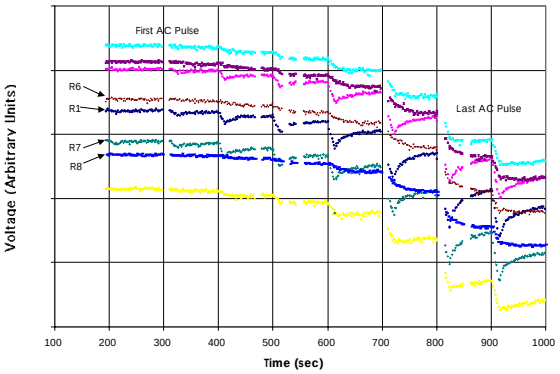

Fig. 2.28. Resistance thermometer voltages vs time—AC current pulses on Test Coil 1 at 30 K.

Figure 2.29 shows the comparative performance of the three test coils at one temperature and current. The plots show the losses per unit length in arbitrary (but consistent) units vs the turn location in the winding in percent. The zero percent points were at the end turns on the outer winding and had the highest losses. The losses decreased on turns successively closer to the center of the winding. These low center losses are characteristic of the losses designed and expected for nearly the entire primary and secondary coils in the 5/10-MVA transformer. Test Coil 2 showed a peak in the losses 25% below the top end of the winding. This anomalous behavior was traced to variations in the conductor critical current. The dc V-I curves for this sample showed that the conductor near the loss peak had considerably lower-than-average critical current compared with the rest of the sample, and the conductor near turn 1 had considerably higher-than-average critical current.

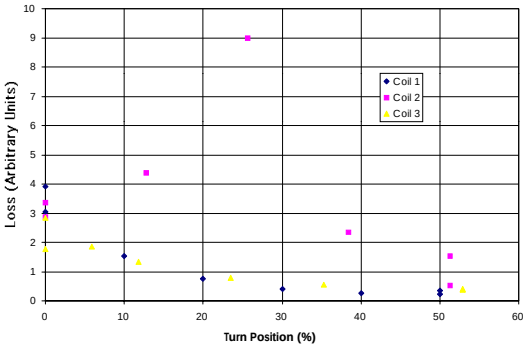

Fig. 2.29. Comparison of AC test coil AC losses.

The ac loss data for the central turns of the test coils were compared to two idealized theoretical models that give upper and lower limits for the expected losses for each winding scheme, assuming a uniform critical current in the HTS material. The measured ac losses vs current on Test Coil 2, which used winding configuration 2, did not compare favorably with the theoretical models. The details of these calculations are proprietary. The tests with configuration 1 for Test Coils 1 and 3 were close to the calculated lower-limit values. These measurements have guided and to a large degree substantiated the

basic winding design and projected losses for the 5/10-MVA HTS transformer. In the future, more test coils will be investigated, and variable-frequency tests will be performed to determine the relative roles of coupling and hysteresis in the ac losses. It should also be possible to perform electrical loss measurements on test coils in the same apparatus with a bridge circuit and a lock-in amplifier.

2.2.2 Transformer Design Studies

The team met on several occasions to work out detailed designs for the 5/10-MVA transformer. The unit will incorporate several features of the commercial 30-MVA design to provide extended operation at twice rating and to remain superconducting through a 10× fault current and a 3-day power outage. Table 2.5 compares the specifications of the two transformers.

Table 2.5. Comparison of transformer specifications

	5/10-MVA	30-MVA
Connection	3-ϕ, Δ/Y	3-ϕ, Δ/Y
Pri/sec voltage (kV)	24.9/4.2	138/13.8
Pri/sec BIL (kV)	150/50	550/110
Pri/sec current (A)	67/694	72/1255
Overload ratings		
10× (s)	2	2
2× (h)	48	48
3-day power outage handling	Backup motor/generator	Backup motor/generator
Cooling system	Cryocoolers	Cryocoolers
Instrumentation	Local	Remote

During the fiscal year, a planned task for ORNL on wireless instrumentation development was replaced by a new task to carry out analysis, design, and testing on the cryogenic cooling system for the 5/10-MVA transformer windings. ORNL will design, procure, and assemble the components of this system on a subflange that will be shipped to the WES site for final testing and integration into the 5/10-MVA transformer. Analysis for the system is nearly complete, and detailed design and procurement will take place early in FY 2001. IGC has identified an appropriate commercial wireless instrumentation system and will take the lead in further efforts with it.

2.2.3 High-Voltage Insulation Development

Development work on high-voltage insulation progressed from the generic studies carried out in the previous fiscal year to verification tests on samples that simulate key features of the 5/10-MVA dielectric design. Thermal-cycling and dielectric-breakdown tests were carried out on selected epoxy materials. AC withstand, BIL, and lifetime tests were carried out on a cylindrical-electrode sample. Verification studies were also carried out on cooling-system components that will be subjected to high voltage. Tests on proposed concepts for the 5/10-MVA bushing/downlead and delta connection systems will begin early in FY 2001. Results are summarized in Sect. 2.3 of this report.

2.3 INSULATION STUDIES AT ORNL IN SUPPORT OF SUPERCONDUCTING POWER APPLICATIONS

D. R. James and I. Sauers

ORNL is conducting research into the aspects of multi-component insulation systems for use in power apparatus. Efforts have been concentrated on development of basic techniques for use in measurement and characterization of cryogenic insulation, construction of new apparatus, and application-specific testing of proprietary systems.

Insulation systems studies require a careful blending of basic, small-scale, scientific measurements and theory of dielectrics with larger, more elaborate sub-scale engineering studies. The small-scale studies provide guidance and understanding of the breakdown mechanisms and the initial information needed to design the sub-scale experiments. The sub-scale experiments are generally proprietary in nature, expensive, and crucial to the overall success of larger-scale applications.

Bulk breakdown of small-scale systems is well characterized in the literature; therefore, the program efforts are concentrating on the dielectric performance at the interface between two different insulating materials and large-scale studies of bulk performance. The systems under study include vacuum-solid, gas-solid, liquid-solid, and solid-solid interfaces. The dielectrics and high-voltage research facility includes a high bay, high-voltage laboratory, and a control room for impulse testing cryogenic model cable; a laboratory where model cables can be constructed in-house; and another laboratory housing a shielded room for making partial-discharge and breakdown measurements. A high-voltage, high-pressure cryostat is used to perform sensitive partial-discharge and aging studies on short lengths of model HTS cables.

During the past year dielectrics testing for HTS cable has included aging tests on short lengths of simulated HTS cable for periods up to 24 h, the initiation of phase-resolved partial-discharge testing, and the testing of a model cable splice. Testing of dielectrics for HTS transformers has concentrated on cast epoxy in both parallel-plane and cylindrical geometries made from different epoxy materials and additives.

2.3.1 Electrical Insulation for HTS Cable

2.3.1.1 Splice Tests

The length of HTS cables is limited to the manufacturer's cable facility length and that which can be put on a reel and transported. Hence it is important to demonstrate that two cables can be successfully joined together with a splice. Where the dielectric and conductor join, there is a field enhancement due to the nonuniformity, which can lead to premature breakdown unless the field is reduced by proper grading. Toward this end a dielectric splice design was tested on a model cable. Figure 2.30 shows a schematic of the splice test. The following tests, which were conducted in liquid nitrogen (LN_2) at system pressure, were successfully performed and passed:

- 30-min ac withstand at 2.5 times operating voltage (18 kV_{rms}),

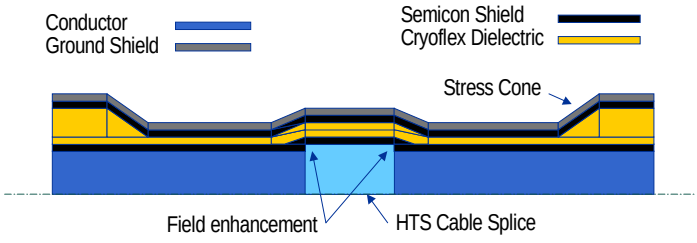

Fig. 2.30. Schematic of model cable splice test.

- partial discharge level less than 1 pC at 18 kV,
- passed ac voltage breakdown test at 10 times the rated voltage, and
- passed 110-kV BIL impulse test (1.2 × 50 μs, negative impulse)

2.3.1.2 Model Cable Aging Studies

A small model cable dewar has been set up for aging studies and partial discharge (PD) analysis. This chamber consists of an outer dewar as a LN_2 bath to hold temperature at or near 77 K and an inner dewar test vessel that will withstand 15 bar absolute pressure. Small model cables are wrapped on 2-in. diam., 19.5-in. stainless steel mandrels on a lathe specially adapted for cable wrapping. The mandrel is suspended from the high-voltage feedthrough by a thin-walled stainless steel extension rod that, along with thermal insulation disks, maintains the temperature transition gradient. An automated high-pressure LN_2 fill system has been installed that consists of level sensors for both inner and outer dewars, solenoid fill valves, a standard fill dewar and a high-pressure fill dewar for the inner chamber. This automated system allows continuous aging studies to be conducted during the day, overnight, and on weekends without personnel needing to be present. The duration of the aging study is recorded on a strip chart; an automatic timer shuts off the system when a breakdown occurs.

An innovative PD system has been developed for model cable-aging studies. Conventional PD detectors connected to the high-voltage bus have difficulty locating the source of PD, which could be anywhere in the system. In the present setup the ground tapes over the stress cone regions are isolated from the ground over the test section of the model cable. Separate leads are brought out so that the PD signals from cable test region and stress cones can be isolated. Special PD detection devices were built for each of the ground leads, which can be analyzed on a digital scope. Also, a state-of-the-art digital PD detection system, purchased from Power Diagnostix, allows a full digital representation of the PD. This system consists of modular A/D converters, preamplifiers, amplifiers, and filters that input to a laptop. The systems can display PD as a function of phase angle, magnitude, and frequency of magnitude; this feature allows interpretation of PD signatures for different sources of PD, such as butt gaps, surface discharge, voids, and delaminations. It has capability for cancellation of known noise pulses, which interfere with the true PD from the cable. We have just begun to work with this system, but it shows great potential for diagnostics. This system is also portable, so that it can be easily carried to other sites for measurements.

Cryogenic dielectric model cable aging studies are used to predict cable lifetime. The lifetime of cables follows the conventional aging relationship, $t\,E^n$ = constant, where t is the lifetime, E is the applied electric field, and n is the life constant characteristic of the insulation material and system being tested. Aging tests are performed by setting the ac voltage or electric field at a constant value and measuring the time to failure. The field is changed, and the test repeated for a new cable. Several tests at the same field are generally required to get reasonable statistics. Weibull statistics can also be used to determine the best value for a given voltage. A log-log plot of the field vs lifetime gives a straight line with the life constant n as the negative slope.

A number of aging studies were performed on large (4-ft) model cables in the large dewar (see Fig. 2.31). The predicted 30-year lifetime is determined from the aging curve by extrapolating the “best fit” of the aging relationship to the data. In the case of the present data, the operating stress of the Southwire cable is several times lower than the predicted field strength for 30 years. Aging data were measured for times up to 24 h. Conducting aging studies for as long a time period as practical improves the accuracy of the prediction. The automated LN_2 fill system on the small dewar will allow longer tests (up to two weeks or more) to be performed.

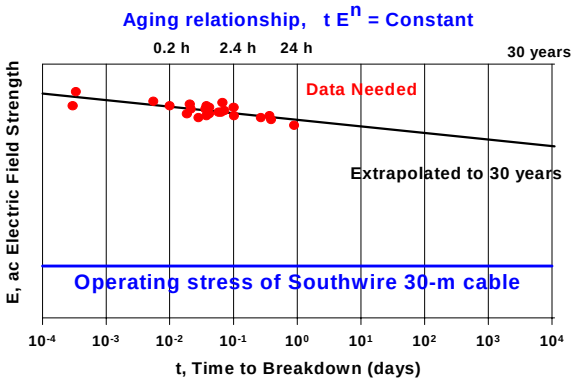

Fig. 2.31. Time-to-breakdown, *t*, vs applied electric field, *E*, for model cables at liquid nitrogen temperature. The solid line through the data points represents a best fit given by the aging relationship tE^n = constant. The fitted line extrapolated to 30 years exceeds the operating stress of the Southwire cable (indicated by the horizontal line).

2.3.1.3 Cryogenic Dielectric Materials Studies

A program was begun to examine alternative cryogenic dielectric materials. Until this study, we had focused primarily on Cryoflex, a proprietary dielectric tape produced by Southwire. There has been little additional work in this area since the advent of low-temperature superconductors (LTSs) and work on the LTS cable projects some 20 years ago. Since that time a number of new materials and reformulations of old materials have been developed and warrant examination. New production procedures have reduced cost on some materials that had been ruled out on the basis of cost alone. Some of the desirable properties of cryogenic dielectrics include the following:

- High dielectric strength, including puncture strength and surface flashover.
- Low partial discharge/aging. Some materials are degraded more rapidly by PD than others.
- Low dissipation factor. Reduces losses due to the dielectric.
- Thermal compatibility. Thermal contraction of different materials must match to avoid cracking of the dielectric. Material must withstand thermal cycling.
- Mechanical strength of solids. Mechanical properties of dielectric tape are important for lapped tape designs.
- Thermal conduction. High thermal conduction is desirable to dissipate any generated heat.
- Dielectric constant. Ideally the dielectric constant should match that of LN_2.

Mechanical properties are being evaluated by Southwire. The following measurements are under way at ORNL to evaluate candidate materials:

- ac breakdown,
- impulse breakdown,
- partial discharge and aging,
- dissipation factor, and
- thermal shock tests.

2.3.2 Transformer Project

2.3.2.1 Temperature Cycling Tests on Solid Dielectrics

Solid dielectric materials must be thermally compatible with the conductors they insulate. If there is a thermal mismatch of any materials, cracking of the dielectric may occur on cooldown; and cracking will usually result in dielectric failure and/or mechanical-strength failure. Thermal cycling tests were performed on selected epoxy materials. The so-called “dunk tests” used is an extreme test of the material. A steel bolt is cast in epoxy, and the piece is immersed rapidly in LN_2 without precooling. The sample is

removed after 5 min and is warmed to room temperature. This procedure is repeated 25 times or until the sample fails. A number of materials crack on the first or second dunk, indicating a significant stress in the material due to mismatch of the thermal contraction. Although normal cooling for equipment is expected to be much more gradual, this extreme test can rapidly screen out materials on that basis and can identify some particularly good ones. Figure 2.32 shows examples of tests on two of the epoxy samples.

Fig. 2.32. Thermal shock tests of candidate epoxy materials.

High-voltage breakdown tests were performed on those materials that passed the dunk test.

2.3.2.2 Breakdown Studies of Selected Epoxy Materials

Breakdown tests were performed on a number of materials in various electrode geometries, such as sphere-sphere and plane-plane. Sphere-sphere geometry results in significantly higher breakdown strengths due to the stressed volume effect. The electrical breakdown of solids is related to the number of defects in the material; i.e., a weakest-link model. The volume of material under high electric stress between spheres is relatively small compared with that of planes; hence the number of defects is smaller, resulting in a lower probability of breakdown for a given applied field. Therefore, breakdown measurements were generally conducted with a plane-plane geometry in which the flat areas of the planes were approximately 0.875 in. Gaps of 0.5 and 1.0 mm were used. A special jig was fabricated to cast six sets of electrodes at the same time. Each set of electrodes (except for the leads) was totally encased in the epoxy. Breakdown tests were performed (1) at room temperature in an oil bath to prevent flashover around the outer surface of the epoxy and (2) at 77 K in a LN_2 bath.

The materials studied included epoxy resins with various hardeners, filled epoxies, and composite materials. Four or five samples of each type were run to obtain better statistics. The ac breakdown strength in LN_2 was generally about twice that at room temperature. This result is consistent with literature values. The impulse-to-ac ratio in LN_2 was found to be approximately 2. Table 2.6 gives the breakdown strengths of several epoxies and includes comments on the thermal properties. The compounds are not identified for proprietary reasons. There is some significant variation in the strengths

Table 2.6. Breakdown strengths (in kV/mm and kV/mil) for various epoxy materials at room and liquid nitrogen temperatures

Material[a]	kV_{rms}/mm	kV_{rms}/mil	Temp	Thermal shock
Epoxy A	73.5	1.879	Room	Fail lst
Epoxy B	70.3	1.79	Room	Pass 25
Epoxy B	142.3	3.62	LN_2	Pass 25
Epoxy B (impulse 1.2/50 μs)	274.8	6.98	LN_2	Pass 25
Impulse ratio at LN_2	2			
Epoxy C	82.5	2.100	Room	Fail 1st
Epoxy D	77	1.960	Room	Fail 1st or 2nd
Epoxy E	49.5	1.26	LN_2	Pass
Epoxy F	39.1	0.9909	LN_2	Good; 20
Composite A	15.7–35.4	0.4–0.9	LN_2	Cracking
Composite B	41.8	1.060	LN_2	Good

[a]The compounds are not identified for proprietary reasons.

between the different epoxies. The spread in data for a given epoxy can be significant; therefore, numerous samples should be run to obtain reliable statistics.

2.3.2.3 Cast Epoxy High-Voltage Withstand Testing

A small insulation model was devised wherein a set of electrodes with practical geometry was cast in an epoxy composite system. The sample was precooled slowly in LN_2 vapor and was then immersed in LN_2 at atmospheric pressure. The leads were spread far apart to avoid flashover in the air above the liquid. The system withstood 65 kV ac rms (2.5 times operating) for 30 min and withstood three impulse lightning surges (1.2 × 50 μs waveform) at 153 kV(BIL test). Figure 2.33 shows the sample prior to testing. Future tests on such samples will include aging, PD, and tan delta for dielectric loss.

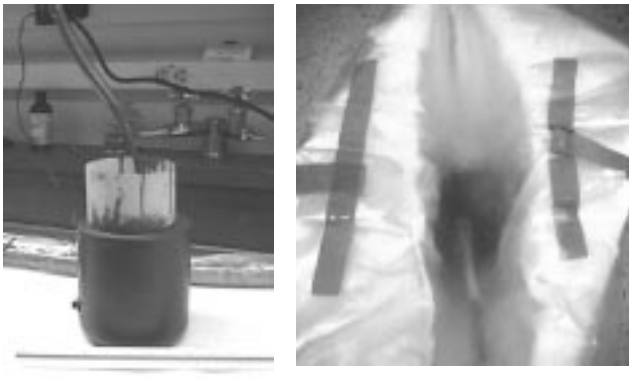

Fig. 2.33. Cast epoxy electrodes (on left) and sample immersed in liquid nitrogen bath at atmospheric pressure for high-voltage withstand and breakdown tests (on right).

2.4 MARKET AND TECHNOLOGY ASSESSMENT

Ivars Gutsmanis, HOBE Corp.; T. P. Sheahen, SAIC

2.4.1 Cryogenic R&D Assessment

In general, the status of cryogenic R&D in the world can be described as follows: “if HTS power devices need higher efficiency and lower price, then the market will provide it when sufficient demand is shown to exist” without any added incentive. Several technologies are identified as potential breakthroughs, the most obvious being pulse, tube refrigeration and improved compressor performance. However, certain improvements in materials or components (flexure bearings) could provide higher reliability and enhanced performance.

2.4.2 Cryogenic Roadmap and Implementation Plan

The paper, “Method Estimating Future Markets for High Temperature Superconductors,”[1] describes the analysis methods used in the unpublished report, *Analysis of Future Prices and Markets for High Temperature Superconductors*.[2] The paper states the economic case for continuing second-generation HTS conductor R&D and initiating cryogenic R&D.

There is a strong link between the assumptions made in the economic analysis concerning cryogenic performance and the intended pathway of cryogenic R&D as expressed in the latest draft of the *Cryogenic Roadmap*.[3] If one assumes that HTS conductor performance is sufficient to allow the use of liquid nitrogen for cooling purposes, the cost of LN_2 at 5 to 6 cents per liter is so low that direct cryocooling is not economical with present cryogenic refrigeration technology. For economic parity, cryocooler performance must achieve the goals stated in the *Cryogenic Roadmap* of $25 to 30/kW-cold and 25 to 30% of Carnot efficiency. In reality, a hybrid system is needed to allow smaller cryocoolers for normal operations and stored LN_2 for emergency overloads.

2.4.3 References

1. “Method Estimating Future Markets for High Temperature Superconductors,” *IEEE Proceedings on Applied Superconductivity* (to be published).

2. J. W. Mulholland, T. P. Sheahen, and D. W. McConnell, *Analysis of Future Prices and Markets for High Temperature Superconductors*, unpublished.

3. T. P. Sheahen and B. W. McConnell (eds.), *Cryogenic Roadmap*, submitted to the U.S. Department of Energy by the Steering Committee.

3. Summary of Technology Partnership Activities

3.1 BACKGROUND

Oak Ridge National Laboratory (ORNL) is a key participant in the U.S. Department of Energy's (DOE's) national effort on electric power applications of high temperature superconductivity (HTS). ORNL has formed effective teams that combine the resources of the Laboratory with the entrepreneurial drive of private companies. New technology partnership mechanisms, a feature of the ORNL Superconducting Technology Program for Electric Power Systems since its inception in 1988, have resulted in 41 superconductivity "pilot center" cooperative agreements and 7 cooperative R&D agreements (CRADAs). Eight cooperative agreements and three interagency agreements were active during FY 2000. In addition, licensing agreements, joint inventions, and joint publications with the private industry partners have ensured that there *is* technology transfer throughout the program.

Technology partnering on Laboratory-industry teams can occur in several ways. Spinoff technology partnering involves the licensing of patentable Laboratory inventions to industry, continued product or process development to the point of demonstration of precommercial viability, or both. In the ORNL program, the cooperative development level of technology partnering is emphasized: joint Laboratory-industry teams work on problems that (1) requires combined resources and expertise and (2) have a clear objective of precompetitive research and technology development. For the project to succeed, each partner depends on the success of the other. Most of the cooperative projects with private industry and the Laboratory precompetitive research and development (R&D) projects involve developing key technology in which commercialization of the results is expected to occur after a minimum of 3 to 5 years.

3.2 RELATIONSHIP TO THE DOE MISSION

The ORNL program mission is that of its program sponsor, DOE's Office of Power Technologies, Superconductivity Program: to develop the technology base necessary for industry to proceed to commercialization of electric energy applications of HTS. HTS will enable new energy-efficient motors, transformers, and transmission lines and will also provide electric power equipment manufacturers with strategic technology for global competitiveness. Electric utilities can defer acquisition of new transmission rights-of-way with successful introduction of superconducting cables. System stability and protection will be enhanced with the introduction of fault-current limiters. Distributed utility systems in the future, which will include distributed generation systems, will benefit from the small size and weight of the next generation of electric power equipment. In addition, oil-free power transformers and cables will provide a cost-effective, more environmentally friendly option for the utility sector.

3.3 FUNDING

DOE funding for the ORNL program, a summary of funds-out cooperative agreements and subcontracting activities in 2000, are shown in Tables 3.1, 3.2, and 3.3.

3.4 TECHNOLOGY PARTNERSHIP APPROACH

Our interdisciplinary approach uses many of the resources available at ORNL to meet the program goals for joint Laboratory-industry development of HTS technology for electric power applications. Our

Table 3.1. Superconducting Technology Program funding: authorization and outlay by fiscal year

	New budget authorization/outlay ($ × 1000)				
	1996	1997	1998	1999	2000
Direct scientific and technical[a]	2,995	3,046	5,356	5,416	5,616
Management and outreach	310	310	400	400	400
Subtotal—ORNL	3,305	3,356	5,756	5,816	6,016
Subcontracts[b]	1,290	1,021	2,437	3,244	4,099
Funds-out cooperative agreements[c]	286	789	589	795	585
Total program	4,881	5,166	8,782	9,855	10,700

[a]Includes ORNL capital equipment.

[b]Details are provided in separate table. Funds-out cooperative agreements provide partial financial support to U.S. industry for cost-shared cooperative R&D.

[c]Includes interagency agreements (NIST, NASA, NSF).

superconductivity agreement mechanism interlinks R&D projects with industry and universities that optimize utilization of facilities, expertise, and program resources for the benefit of all participants. This program also coordinates the ORNL activities with the other national laboratories, government agencies, university centers, and industry groups.

Cooperative agreements ensure that technology development is industry-driven. The Office of Technology Transfer and Economic Development and patent counsel work together to place these agreements. Where appropriate, these efforts are coordinated with projects within ORNL that are funded by the DOE Office of Science, as well as Work for Others and ORNL Laboratory Director's R&D Fund projects.

Effective funds-out to industry is used to supplement industry cost share. In FY 2000, $4.66 million in funds-out to industry and universities was provided through cooperative agreements and subcontracts. To keep industry involved from the start of the program and to ensure commercialization potential, all of these technology-partnering mechanisms are augmented by CRADAs, user agreements, and licensing activities.

Responsiveness to American industry has high priority in this program. An ORNL ad hoc technical review committee, consisting of a project manager, a scientific coordinator, a manager for conductor development, and a manager for applications development, reviews all inquiries from industry and recommends projects for possible funding. This review ensures that (1) the proposed work fits the program mission, (2) the work is collaborative, (3) there is legitimate commercial interest, and (4) the work is feasible. Substantial private-sector cost share is required on cooperative agreements.

ORNL provides support to the DOE Headquarters (DOE-HQ) Superconductivity Program for Electric Power Systems by identifying, guiding, and monitoring R&D at ORNL and ORNL subcontractor sites and by performing coordination, analysis, and planning of activities related to the national program.

Some of the various activities performed as part of this task include the following:

- technical, project, and budget guidance;
- project identification and development;
- exploratory R&D;

Table 3.2. Superconductivity Program summary of cooperative agreements as of September 30, 2000

Participant	Approved term	Type[a]	Total agreement cost share ($K)			Technology area
			By DOE		By	
			To ORNL	To industry	industry	
American Superconductor	8/15/96-4/30/2001	FI	1000	0	1785	BSCCO-2223 Wire Development Group and SBIR project
EURUS Technologies	9/9/99-9/9/2001	C	150	0	500	Development of buffered, textured metal metal substrates for superconducting wires
MicroCoating Technologies	9/15/97-3/31/2002	FI	150	0	1100	Develop coated conductor technology
NASA Kennedy Space Center	4/15/2000-4/14/2001	IAG	0	60	61	Cryogenic thermal insulation system requirements for HTS applications—development of long flexible cryostats
NIST—Gaithersburg	9/93-11/2000	IAG	0	750	750	BSCCO and TBCCO phase diagram support
NIST—Boulder	3/98-2/2001	IAG	0	562	562	Electromechanical properties for superconductor applications
NSF Science & Tech. Policy Institute (RAND)	4/15/2000-10/14/2001	IAG	0	200	0	HTS critical issues study
Oxford Instruments	1/94-1/31/2002	C	1050	0	1275	Develop technology for dip-coated BSCCO-2212 wire and RABiTS™
Southwire Company	2/1/97-9/30/2001	FO	6066	500	6631	Develop HTS cable technology
3M-Southwire-LANL-ORNL	4/3/97-2/3/2001	C				Development of HTS wire using coated conductor technologies
3M					2458	
Southwire					480	
LANL				1680[b]	2938	
ORNL			1800			
Waukesha Electric Systems	6/15/97-12/31/2001	FO	1425	250	1258.4	HTS transformer
Total Active Agreements			11641	2322	16860.4	
Total Completed Agreements			13224	5220.6	14702.7	
TOTALS			24865	7542.6	31563.1	

[a]NFE = No-Funds-Exchange; FO = Funds-Out; FI = Funds-In; IAG = Interagency Agreement; and C = CRADA.
[b]DOE to LANL.

Table 3.3. FY 2000 active subcontracts

Subcontractor	Term	Obligated amount	Subject
Imtech	10/3/94–2/29/00	358	Assist research on HTS materials
	3/1/2000–2/28/01	66	
Massachusetts Institute of Technology	4/29/96–9/30/00	475	Stability of HTS conductors and coils
New—(competed)	6/1/00–5/31/02	190	Stability and quench protection
Florida State University (competed)	6/1/00–5/31/02	125	Stability and quench protection
Oak Ridge Inst. for Sci. and Edu. (competed)	Ongoing	680	Postdoctoral research fellowships
Energetics, Inc. (competed)	4/96–2/00	1160	Technical and analytical support to ORNL
New—(competed)	4/18/00–3/31/01	407	
Bob Lawrence & Associates	2/17/97–2/16/99	375	Technological and economic benefits assessment and market study
New—(competed)	3/15/99–1/14/02	373	HTS outreach
University of South Carolina	4/1/98–3/31/99	10	High-temperature conductor development
	7/1/99–9/30/01	20	and characterization
Stanford University (competed)	10/1/98–9/30/01	1097	Ion-beam-assisted deposition of buffer layers and in situ deposition of YBCO by electron beam evaporation
University of Wisconsin (competed)	10/1/98–9/30/01	1124	BSCCO critical currents and microstructure, YBCO coated conductor microstructure, and pulse tube cryocooler
University of Houston (competed)	10/1/98–9/30/01	407	Research into high-rate photon-assisted MOCVD for YBCO onto buffered, textured metallic substrates
Marshall O. Pace	12/98–12/99	18	High-voltage breakdown studies on
	12/99–12/00	18	cryogenic insulation
Western Technology, Inc.	3/1/99–11/30/99	24	Cryogenic system analysis for electric power sector
National Conference of State Legislatures	3/22/99–3/21/00	19	State Legislative Report on Superconductivity
Boston College	6/28/99–2/18/01	99	Development of Epitaxial Film Growth and Properties
MicroCoating Technologies (competed)	11/1/99–5/15/01	760	Coated conductor research
3M (competed)	2/1/00–7/31/00	447	Coated conductor research
IGC (competed)	6/7/00–12/7/00	250	Coated conductor research
Hobe Corp	3/3/00–2/28/01	42	Analysis of cryogenic R&D
SAIC	7/15–12/31/00	45	Preparation of cryogenics implementation plan
University of Florida	10/1/00–9/30/01	53	HTS Films and Buffers on Biaxially Textured Copper
University of Kansas	5/00–5/01	49	Hg-based HTS coated conductors

- support of consultants and subcontracts providing technical, program, or technology partnering support;
- identification, placement, and technical monitoring of subcontractors, review committee members, and workshop guests;
- guidance and support on technology partnering;
- publication of reports and proceedings from workshops;
- identification and initiation of cooperative agreements, interagency agreements (i.e., National Institute of Standards and Technology), and memoranda of understanding;
- distribution of reports to program managers;
- preparation of assessments to address technical, economic, regulatory, and institutional issues in the DOE program;
- coordination of interlaboratory technical team meetings;
- assistance to the DOE-HQ program manager in preparation of the Superconducting Technology Program Annual Operating Plan;
- collection and dissemination of programmatic information and program-wide assessments;
- assistance in organizing the HTS Wire Development Workshop [in partnership with Argonne National Laboratory (ANL) and Los Alamos National laboratory (LANL)]; and
- review of industrial collaboration opportunities through multilaboratory meetings and conference calls.

ORNL works with the other program laboratories to address such issues as communication among program participants, workshop and meeting implementation, planned competitive solicitations and superconductivity agreements, and coordination of technical and economic assessments.

An Industrial Overview Committee is charged with reviewing program activities and advising Laboratory management as to program progress, policy, and direction. The committee consists of representatives of electric utilities, original equipment manufacturers, and HTS wire manufacturers. This committee meets occasionally at ORNL, ANL, or LANL.

3.5 PROGRAM INVENTIONS AND PATENT LICENSE AGREEMENTS

A summary of the new invention disclosures for FY 2000 is shown in Table 3.4. All patent license agreements since 1988, and issued patents in FY 2000, are shown in Tables 3.5 and 3.6, respectively.

Table 3.4. Superconducting Technology Program invention disclosures in FY 2000

ID No.	Subject	Submitted by
826	Methods of Fabricating Polycrystalline, HTS Conductors with Reduced Weak-Link Effects at Grain Boundaries	A. Goyal and D. M. Kroeger
871	Method and article of fabricating a textured, buffered substrate	A. Goyal
872	Method and article of fabricating a substrate which has an extremely sharp biaxial texture by controlled abnormal grain growth	A. Goyal
873	Method and article of fabricating a substrate which has an extremely sharp biaxial texture	A. Goyal
875	A textured, buffered substrate and devices thereon	A. Goyal
876	Method and article of fabricating a substrate with a certain microstructure for growth of epitaxial oxides, nitrides as well as electromagnetic device layers such as high temperature superconductors	A. Goyal
877	Method and article of fabricating powder-in-tube and thick film superconductors to get high performance by simple microstructural modification	A. Goyal
878	Method of depositing epitaxial metal layers on a substrate	A. Goyal
879	Superconducting Transistor based on a tunable dielectric base	S. Pennycook and D. K. Christen
889	Method of depositing an electrically conductive film on a roll-textured metal/alloy substrate and articles formed therefrom	M. Paranthaman, T. Aytug, and D. K. Christen

Table 3.5. Superconducting Technology Program patent license agreements

1039-X
Superconductive Components, Inc. (complete)
1640-X (RABiTS™)
Midwest Superconductivity, Inc. (complete)
Oxford Superconducting Technology
CCVD, Inc., dba MicroCoating Technologies
EURUS Technologies
3M
American Superconductor Corporation

Table 3.6. Superconducting Technology Program patents issued in FY 2000

Patent No.	Date Issued	Title
5,964,966	October 12, 1999	Method of Forming Biaxially Textured Alloy Substrates and Devices Thereon
5,968,877	October 19, 1999	High-T_c YBCO Superconductor Deposited on Biaxially Textured Ni Substrate
5,972,847	October 26, 1999	Method for Making High-Critical-Current-Density $YBa_2Cu_3O_7$ Superconducting Layers on Metallic Substrates
6,055,446	April 25, 2000	Continuous Lengths of Oxide Superconductors
6,077,344	June 20, 2000	Sol-Gel Deposition of Buffer Layers on Biaxially Textured Metal Substances
6,106,615	August 22, 2000	Method of Forming Biaxially Textured Alloy Substrates and Devices Thereon
6,114,287	September 5, 2000	Method of Deforming a Biaxially Textured Buffer Layer on a Textured Metallic Substrate and Articles Therefrom

4. Events, Honors, and Awards

4.1 PATENT LICENSE AGREEMENT WITH AMERICAN SUPERCONDUCTOR CORPORATION

Oak Ridge National Laboratory (ORNL) and American Superconductor (ASC) celebrated the signing of a patent license agreement for ORNL's Rolling Assisted Biaxially Textured Substrate (RABiTS™) superconducting wire technology on May 30, 2000. The group also announced a new funds-in cooperative research and development agreement (CRADA) to develop YBCO/RABiTS™ wires using ASC's proprietary "trifluoroacetate TFA" approach (see Figs. 4.1 and 4.2).

Fig. 4.1. Pictured (left to right): Bill Oosterhuis (DOE Office of Science), Jim Daley (DOE Office of Energy Efficiency and Renewable Energy), Jim Reafsnyder (DOE-ORO), Frank Borman (American Superconductor), Linda Ponce (Office of Congressman Zach Wamp, R-Tenn.), Greg Yurek (American Superconductor), and Larry Dickens and Bob Hawsey (ORNL).

Fig. 4.2. Pictured (left to right): Mike Gouge (ORNL), Frank Borman (American Superconductor), and Parans Paranthaman (ORNL).

4.2 ORNL PART OF "COLLABORATION SUCCESS" AWARD-WINNING TEAM

The Superconductivity Materials Group of ORNL is participating in an effort that has earned a Collaboration Success Award from the Council for Chemical Research. The organization selected the Wire Development Group, of which the ORNL Superconducting Materials Group in the Metals and Ceramics Division is a major participant, for its "outstanding contribution" to the advancement of HTS wire technology. The nine-year-old collaborative Wire Development Group also includes research teams from ASC, Argonne and Los Alamos national laboratories, and the University of Wisconsin.

ORNL's Superconducting Materials Group was part of the effort focusing attention to the effect deformation processing on the density and texture of the precursor powder prior to heat treatment. ORNL scientists Don Kroeger, Dominic Lee, and Bob Williams concentrated on development of novel mechanical deformation procedures, analysis and interpretation of the wire's microstructures, and exploration of alternative fabrication concepts of the bismuth compound.

In the United States, more than seven percent of electricity is presently wasted due to resistance in wires. Superconductors can carry electric current with almost no energy loss due to resistance. The council determined the research that played a key role in ASC's establishment of a leadership position in reliable HTS wire manufacturing. ASC recently decided to scale up production of this technology to yield millions of meters of bismuth compound superconducting wire per year by 2002. The composite wire produced by ASC is being used in numerous first-generation HTS electric power systems, including transmission lines, motors, transformers, and fault-current limiters.

4.3 ORNL ANNUAL AWARDS NIGHT

A five-division team of scientists and engineers from ORNL recently received double honors at ORNL's annual Awards Night celebration. The team won a Technical Achievement Award for their efforts with Southwire Company that led to the world's first HTS cable system to power an industrial plant. In addition, the entire group was also honored with ORNL's "Engineer of the Year" Award. (See Fig. 4.3.) John Stovall of ORNL's Energy Division and J. Winston Lue of the Fusion Energy

Fig. 4.3. ORNL's "Engineers of the Year" Award Team. Back row (left to right): G. C. Barber, D. O. Sparks, A. Fadnek, M. J. Gouge, J. P. Stovall, P. W. Fisher, and D. R. James. Front row (left to right): V. Patania, A. Ellis, P. M. Martin, I. Sauers, J. A. Demko, and J. W. Lue. Team members not pictured: S. W. Schwenterly, C. Foster, and R. D. Benson.

Division represented the team as project manager and principal investigator, respectively, at the awards banquet held in Knoxville, Tennessee.

4.4 FEDERAL LABORATORY CONSORTIUM EXCELLENCE IN TECHNOLOGY TRANSFER AWARD

Bob Hawsey, director of ORNL's Superconductivity program, accepted an award from the Federal Laboratory Consortium (FLC) in November 2000 on behalf of ORNL's team of engineers and scientists who are collaborating with the Southwire Company of Carrollton, Georgia, in developing and commercializing HTS power cables (see Fig. 4.4). The project, conducted as part of DOE's Superconductivity Partnership Initiative, has combined the scientific expertise of one of the DOE's multiprogram research laboratories with the entrepreneurial drive of a leading U.S. wire and cable manufacturer.

The FLC's overall mission is to add value to the federal agencies, laboratories, and their partners to accomplish the rapid integration of R&D resources within the mainstream of the U.S. economy. At the same ceremony, Larry Dickens, of ORNL's Office of Technology Transfer and Economic Development, was awarded the Commercialization Manager of the Year plaque for his professional achievement and dedication to detail in developing new mechanisms and approaches for increased licensing opportunities, revenue generation, and sponsored research for ORNL (see Fig. 4.5).

Fig. 4.4. Bob Hawsey receives award on behalf of the ORNL Southwire Cable Project team from David Appler, FLC Vice-Chairman.

Fig. 4.5. Larry Dickens receives the Commercialization Manager of the Year Award from David Appler, FLC Vice-Chairman.

4.5 SOUTHWIRE WINS STATE OF GEORGIA GRAND AWARD

The Southwire Company's HTS Power Delivery System has taken second place overall in the Georgia Engineering Excellence Awards competition. The HTS project won first place in the R&D category and received the state Grand Award. The project was recognized during an awards ceremony and reception in February 2001 in Atlanta.

5. Presentations/Publications

S. Annavarapu, L. Fritzemeier, Q. Li, A. Malozemoff, V. Prunier, M. W. Rupich, C. Thieme, W. Zhang, M. Gopal, I. Seleznev, M. J. Cima, M. Paranthaman, A. Goyal, and D. F. Lee, "Progress Towards a Low-Cost Coated Conductor Technology," *Physica C* **341-348,** 2319–22 (2000).

T. Aytug, J. Z. Wu, C. Cantoni, D. T. Verebelyi, E. D. Specht, M. Paranthaman, D. P. Norton, D. K. Christen, R. E. Ericson, and C. L. Thomas, "Growth and Superconducting Properties of $YBa_2Cu_3O_{7-}$ Films on Conductive $SrRuO_3$ and $LaNiO_3$ Multilayers for Coated Conductor Applications," *Appl. Phys. Lett*. **76**, 760–62 (February 2000).

T. Aytug, J. Z. Wu, B. W. Kang, D. T. Verebelyi, C. Cantoni, E. D. Specht, A. Goyal, and M. Paranthaman, "An All-Sputtered Buffer Layer Architecture for High-J_c $YBa_2Cu_3O_{7-}$ Coated Conductors," *Physica C* **340**, 33–40 (2000).

R. N. Bhattacharya., H. L. Wu, Y.-T. Wang, R. D. Blaugher, S. X. Yang, D. Z. Wang, Z. F. Ren, Y. Tu, D. T. Verebelyi, and D. K. Christen, "Improved Eelectrodeposition Process for the Preparation of Superconducting Thallium Oxide Films," *Physica C* **333**, 59 (2000).

C. Cantoni, D. P. Norton, D. K. Christen, A. Goyal, D. M. Kroeger, D. T. Verebelyi, and M. Paranthaman, "Transport and Structural Characterization of Epitaxial $Nd_{1+x}Ba_{2-x}Cu_3O_y$ Thin Films Grown on $LaAlO_3$ and Ni Metal Substrates by Pulsed-Laser Deposition," *Physica C* **324**(3–4), 177–86 (1999).

T. G. Chirayil, M. Paranthaman, D. B. Beach, D. F. Lee, A. Goyal, R. K. Williams, X. Cui, D. M. Kroeger, R. Feenstra, D. T. Verebelyi, and D. K. Christen, "Epitaxial Growth of $La_2Zr_2O_7$ Thin Films on Rolled Ni-Substrates by Sol-Gel Process for High T_c Superconducting Tapes," *Physica C* **336** 63–69 (2000).

X. Cui, F. A. List, D. M. Kroeger, D. F. Lee, M. Paranthaman, A. Goyal, B. W. Kang, E. D. Specht, and P. M. Martin, "Continuous Deposition of Ex-Situ YBCO Precursor Films on Rolling-Assisted Biaxially Textured Substrates by Electron Beam Evaporation," submitted to *Physica C*.

X. Cui, F. A. List, D. M. Kroeger, D. F. Lee, M. Paranthaman, A. Goyal, B. W. Kang, E. D. Specht, P. M. Martin, and W. B. Robbins, "Continuous Deposition of Ex-Situ YBCO Precursor Films on Rolling-Assisted Biaxially Textured Substrates by Electron Beam Evaporation," accepted for publication in *Physica C*.

A. Goyal, D. F. Lee, F. A. List, E. D. Specht, R. Feenstra, M. Paranthaman, X. Cui, S. W. Lu, P. M. Martin, D. M. Kroeger, D. K. Christen, B. W. Kang, D. P. Norton, C. Park, D. T. Verebelyi, J. R. Thompson, R. K. Williams, T. Aytug, and C. Cantoni, "Recent Progress in the Fabrication of High-J_c Tapes by Epitaxial Deposition of YBCO on RABiTS," paper submitted to Proceedings of the International Symposium on Superconductivity, Tokyo, Japan, October 14–16, 2000.

A. Goyal, E. D. Specht, R. Feenstra, D. F. Lee, F. A. List, M. Paranthaman, D. M. Kroeger, and D. K. Christen, "Factors Affecting the Critical Current Density of Epitaxial HTS Conductors on RABiTS," extended abstract submitted to Proceedings of the International Workshop on Critical Currents, Fukuoka, Japan, October 17–19, 2000.

R. A. Hawsey, D. M. Kroeger, and D. K. Christen, "Development of Biaxially Textured $YBa_2Cu_3O_7$ Coated Conductors in the U.S.," p. 561 in *Advances in Superconductivity XII, Proceedings of the 12th International Symposium on Superconductivity*, ISTEC, Springer-Verlag, Tokyo (2000).

B. Holzapfel, D. T. Verebelyi, C. Cantoni, M. Paranthaman, B. Sales, R. Feenstra, D. K. Christen, D. P. Norton, "Low Angle Grain Boundary Transport Properties of Undoped and Doped Y123 Thin Film Bicrystals," *Physica C* **341-348**, 1431–34 (2000).

W. N. Kang, B. W. Kang, Q. Y. Chen, J. Z. Wu, Y. Bai, W. K. Chu, D. K. Christen, R. Kerchner, and Sung-Ik Lee, "Triple Sign Reversal of the Hall Effect in $HgBa_2CaCu_2O_6$ Thin Films After Heavy-Ion Irradiation," *Phys. Rev. B* **61**, 722 (2000).

Kerchner, H. R. and D. K. Christen, "Ac Loss in Superconductive Cable: Comparison of YBCO Thin Films and Composite BSCCO/Ag Tapes," abstract submitted to Fall 2000 Materials Research Society, Boston, Massachusetts, November 27, 2000–December 1, 2000.

J. Y. Lao, J. H. Wang, D. Z. Wang, Y. Tu, S. X. Yang, H. L. Wu, Z. F. Ren, D. T. Verebelyi, M. Paranthaman, T. Aytug, D. K. Christen, R. N. Bhattacharya, and R. D. Blaugher, "Synthesis and Characterization of Chromium-Containing, Thallium-Based 1212 Films," *Physica C* **333**, 221–28 (May 2000).

J. Y. Lao, J. H. Wang, D. Z. Wang, S. X. Yang, J. G. Wen, H. L. Wu, Z. F. Ren, D. T. Verebelyi, M. Paranthaman, T. Adage, D. K. Christen, R. N. Bhattacharya, and R. D. Blaugher, "Synthesis and Characterization of Thallium-Based 1212 Films with High Critical Current Density on $LaAlO_3$ Substrates," *Supercon. Sci. Technol.* **13**, 173–77 (2000).

S. W. Lu, F. A. List, D. F. Lee, X. Cui, M. Paranthaman, B. W. Kang, D. M. Kroeger, A. Goyal, P. M. Martin, and R. E. Ericson, "Electron Beam Co-Evaporation of $YBaF_2$-Cu Precursor Films for $YBa_2Cu_3O_7$ Coated Conductors," submitted to *Superconductor Science and Technology*.

A. P. Malozemoff, S. Annavarapu, L. Fritzemeier, Q. Li, V. Prunier, M. Rupich, C. Thieme, and W. Zhang (American Superconductor), A. Goyal, M. Paranthaman, and D. F. Lee (ORNL), "Low-Cost YBCO Coated Conductor Technology," *Supercond. Sci. Technol.* **13**, 473–76 (2000).

I. Matsubara, M. Paranthaman, T. G. Chirayil, E. Y. Sun, P. M. Martin, D. M. Kroeger, D. T. Verebelyi, and D. K. Christen, "Preparation of Epitaxial $YbBa_2Cu_3O_{7-}$ on $SrTiO_3$ Single Crystal Substrates using a Solution Process," *Jpn. J. Appl. Phys.* **38**, L727–30 (1999).

B. W. McConnell, "Transformers—A Successful Application of High Temperature Superconductors," *IEEE Transactions on Applied Superconductivity* **10**(1), (2000).

B. W. McConnell (ORNL), S. P. Mehta (Waukesha Electric Systems), and M. S. Walker (Intermagnetics General), "HTS Transformers," *IEEE Power Engineering Review*, June 2000.

J. S. Morrell, Z. B. Xue, E. D. Specht, A. Goyal, P. M. Martin, D. F. Lee, R. Feenstra, D. T. Verebelyi, D. K. Christen, T. G. Chirayil, M. Paranthaman, C. E. Vallet, and D. B. Beach, "Epitaxial Growth of Gadolinium Oxide on Roll-Textured Nickel using a Solution Growth Technique," *J. Mater. Res.*, **15**(3) (2000).

M. Paranthaman, T. G. Chirayil, F. A. List, X. Cui, A. Goyal, D. F. Lee, E. D. Specht, P. M. Martin, R. K. Williams, D. M. Kroeger, J. S. Sorrell, D. B. Beach, R. Feenstra, and D. K. Christen, "Fabrication of Long Lengths of Epitaxial Buffer Layers on Biaxially Textured-Ni Substrates Using a Continuous Reel-to-Reel Dip-Coating Unit,"submitted to *J. Amer. Ceram. Soc*.

M. Paranthaman, R. Feenstra, D. F. Lee, D. B. Beach, J. S. Morrell, T. G. Chirayil, A. Goyal, X. Cui, D. T. Verebelyi, J. E. Mathis, P. M. Martin, D. P. Norton, E. D. Specht, D. K. Christen, and D. M. Kroeger, "Demonstration of High Current Density YBCO Coated Conductors on RE_2O_3-Buffered Ni Substrates with Two New Alternative Architectures," *Advances in Cryogenic Engineering*, **46**, Part B, 879–86 (2000).

M. Paranthaman, C. Park, X. Cui, A. Goyal, D. F. Lee, P. M. Martin, T. G. Chirayil, D. T. Verebelyi, D. P. Norton, D. K. Christen, and D. M. Kroeger, "YBCO Coated Conductors with High Engineering Current Density," *J. Mater. Res*. **15**, 2647–52 (2000).

C. Park, D. P. Norton, D. T. Verebelyi, D. K. Christen, J. D. Budai, D. F. Lee, and A. Goyal (ORNL), "Nucleation of Epitaxial Yttria-Stabilized Zirconia on Biaxially Textured (001) Ni for Deposited Conductors," *Appl. Phys. Lett.* **76**(17), 24 (April 2000).

C. Park, D. P. Norton, D. F. Lee, D. T. Verebelyi, A. Goyal, D. K. Christen, and J. D. Budai, "Epitaxial Yttria-Stabilized Zirconia on Biaxially Textured (001) Ni for YBCO Coated Conductor," submitted to *Physica C*.

I. Sauers, D. R. James, H. Rodrigo, M. O. Pace, B. W. McConnell, V. P. Patania, and A. R. Ellis, "Surface Flashover of Fiberlgass Reinforced Epoxy Composite Insulation in Vacuum at Liquid Nitrogen and Room Temperatures using Power Frequency AC and Lighting Impulse Waveforms," *Advances in Cryogenic Engineering*, **46**, Part B, 297–304 (2000).

U. K. Sinha, D. T. Lindsay, R. L. Hughey, J. P. Stovall, M. J. Gouge, J. W. Lue, P. Haldar, V. Selvamanickam, and N. Vo, "Development and Test of World's First Industrial High Temperature Superconducting (HTS) Power Cable," paper submitted to Proceedings of IEEE Power Engineering Society Winter Meeting 2001, Columbus, Ohio, January 28–February 1, 2001.

E. D. Specht, A. Goyal, and D. M. Kroeger, "Scaling of Percolative Current Flow to Long Lengths in Biaxially Textured Conductors," *Supercond. Sci. Technol.* **13**, 592–97 (2000).

C. E. Vallet, C. S. Prouteau, R. Feenstra, J. F. Hamet, D. T. Verebelyi, and D. K. Christen, "Atomic Force Microscopy Study of Bicrystal $SrTiO_3$ Substrates and YBCO Thin Films," *Surf. Interface Anal.* **29**, 221 (2000).

D. T. Verebelyi, D. K. Christen, R. Feenstra, C. Cantoni, A. Goyal, D. F. Lee, M. Paranthaman, P. N. Arendt, R. F. DePaula, J. R. Groves, and C. Prouteau, "Low Angle Grain Boundary Transport in $YBa_2Cu_3O_{7-}$ Coated Conductors," *Appl. Phys. Lett*. **76**, 1755–57 (March 2000).

D. T. Verebelyi, D. K. Christen, R. Feenstra, C. Cantoni, and J. R. Thompson, "YBCO Coated Conductors: Few Degree Grain Boundary Transport," abstract submitted to American Physical Society March 2000 Meeting, Minneapolis, Minnesota.

Y. Y. Xie, T. Aytug, J. Z. Wu, D. T. Verebelyi, and D. K. Christen, "Growth and Physical Properties of Hg-1212 HTSC Tapes on Buffered Metal Substrates," *Physica C* **341-348**, 2505-2506 (2000) .

Y. Y. Xie, T. Aytug, J. Z. Wu, D. T. Verebelyi, M. Paranthaman, A. Goyal, and D. K. Christen, "Epitaxy of $HgBa_2CaCu_2O_6$ Superconducting Films on Biaxially Textured Ni Substrates," *Appl. Phys. Lett.* **77**, 4193–95 (2000).

C.-Y. Yang, A. Ichinose, S. E. Babcock, J. S. Morrell, J. E. Mathis, D. T. Verebelyi, M. Paranthaman, D. B. Beach, and D. K. Christen, "Microstructure of a High J_c Laser-Ablated $YBa_2Cu_3O_{7-}$ Sol-Gel Deposited $NdGaO_3$ Buffer Layer/(001) $SrTiO_3$ Multi-Layer Structure," *Physica C* **331**(1), 73–78 (2000).

C.-Y. Yang, A. Pashitski, A. Polyanski, D. C. Larbalestier, S. E. Babcock, A. Goyal, F. A. List, C. Park, M. Paranthaman, D. P. Norton, D. F. Lee, and D. M. Kroeger, "Microstructural Homogeneity and Electromagnetic Connectivity of $YBa_2Cu_3O_{7-a}$ Grown on Rolling-Assisted Biaxially Textured Coated Conductor Substrates," *Physica C* **329**(2), 114–20 (2000).

The following papers have been submitted to the Proceedings of the Applied Superconductivity Conference 2000, September 17–22, Virginia Beach, Virginia, and are to be published in IEEE Transactions on Applied Superconductivity.

C. Cantoni, T. Aytug D. T. Verebelyi, M. Paranthaman, E. D. Specht, D. P. Norton, and D. K. Christen, "Conductive Buffer Layers and Overlayers for the Electrical Stability of Coated Conductors."

J. A. Demko, J. W. Lue, M. J. Gouge, U. Sinha, R. L. Hughey, and Z. Butterworth, "Practical AC Loss and Thermal Considerations for HTS Power Transmission Cable Systems."

R. C. Duckworth, J. M. Pfotenhauer, M. J. Gouge, and J. W. Lue, "Stability and Normal Zone Propagation in YBCO Coated Conductors."

D. M. Feldmann, J. L. Reeves, A. A. Polyanski, A. Goyal, R. Feenstra, D. F. Lee, M. Paranthaman, D. M. Kroeger, D. K. Christen, S. E. Babcock, and D. C. Larbalestier, "Magneto-Optical Imaging of Transport Currents in $YBa_2Cu_3O_{7-x}$ on RABiTS™."

M. J. Gouge, J. A. Demko, P. W. Fisher, C. A. Foster, J. W. Lue, J. P. Stovall, U. Sinha, J. Armstrong, R. L. Hughey, D. T. Lindsay, and J. Tolbert, "Development and Testing of HTS Cables and Terminations at ORNL."

A. Goyal, F. A. List, D. F. Lee, E. D. Specht, R. Feenstra, M. Paranthaman, X. Cui, S. W. Lu, P. M. Martin, D. M. Kroeger, D. K. Christen, B. Kang, D. P. Norton, C. Park, D. T. Verebelyi, J. R. Thompson, R. K. Williams, T. Aytug, and C. Cantoni, "Fabrication of High-J_c Tapes by Epitaxial Deposition of YBCO on RABiTS™."

H. R. Kerchner and D. K. Christen, "AC Magnetic Field Scanner of High-T_c Superconductors."

J. W. Lue, G. C. Barber, J. A. Demko, M. J. Gouge, J. P. Stovall, R. L. Hughey, and U. Sinha, "Fault Current Tests of a 5-m HTS Cable."

M. Paranthaman, T. G. Chirayil, S. Sathyamurthy, D. B. Beach, A. Goyal, F. A. List, D. F. Lee, X. Cui, S. W. Lu, B. Kang, E. D. Specht, P. M. Martin, D. M. Kroeger, R. Feenstra, C. Cantoni, and D. K. Christen, "Fabrication of Long Lengths of YBCO Coated Conductors using a Continuous Reel-to-Reel Dip-Coating Unit."

M. O. Rikel, R. K. Williams, X. Y. Cai, A. A. Polyanski, J. Jiang, D. Wesolowski, E. E. Hellstrom, D. C. Larbalestier, K. DeMoranville, and G. N. Riley, "Overpressure Processing Bi2223/Ag Tapes."

M. W. Rupich, Q. Li, S. Annavarapu, C. Thieme, W. Zhang, V. Prunier, M. Paranthaman, A. Goyal, D. F. Lee, E. D. Specht, and F. A. List, "Low Cost Y-Ba-Cu-O Coated Conductors."

S. W. Schwenterly, J. A. Demko, J. W. Lue, M. S. Walker, C. T. Reis, D. W. Hazelton, X. Shi, and M. T. Gardner, "AC Loss Measurements with a Cryocooled Sample."

T. P. Sheahen, B. W. McConnell, J. W. Mulholland, "Method for Estimating Future Markets for High Temperature Superconducting Power Devices."

J. P. Stovall, J. A. Demko, P. W. Fisher, M. J. Gouge, J. W. Lue, U. K. Sinha, J. W. Armstrong, R. L. Hughey, D. Lindsay, and J. C. Tolbert, "Installation and Operation of the Southwire 30-m High-Temperature Superconducting Power Cable."